Ubiquitous Earthquake Dynamic Triggering in Southern California

Nicolas D DeSalvio[1] and Wenyuan Fan[1]

[1]Scripps Institution of Oceanography, UCSD

February 9, 2023

Abstract

Earthquakes can be dynamically triggered by the passing waves of events from disconnected faults. The frequent occurrence of dynamic triggering offers tangible hope in revealing earthquake nucleation processes. However, the physical mechanisms behind earthquake dynamic triggering have remained unclear, and contributions of competing hypotheses are challenging to isolate with individual case studies. Therefore, developing a systematic understanding of the spatiotemporal patterns of dynamic triggering can provide insights into the physical mechanisms, which may aid mitigation of earthquake hazards. Here we investigate earthquake dynamic triggering in Southern California from 2008 to 2017 using the Quake Template Matching catalog and an approach free from assuming an earthquake occurrence distribution. We develop a new set of statistics to examine the significance of seismicity-rate changes as well as moment-release changes. We show that up to 70% of global M[?]6 events may have triggered earthquakes in southern California and that the triggered seismicity often occurred several hours after the passing seismic waves. On average, earthquakes are triggered about every 4 days in the region, albeit at different locations. Although adjacent fault segments can be triggered by the same earthquakes, the majority of triggered earthquakes seem to be uncorrelated, suggesting that the process is primarily governed by local conditions. Further, the occurrence of dynamic triggering does not seem to correlate with ground motion (e.g., peak ground velocity) at the triggered sites. These observations indicate that nonlinear processes may have primarily regulated the dynamic triggering cases.

Ubiquitous Earthquake Dynamic Triggering in Southern California

Nicolas D. DeSalvio[1], **Wenyuan Fan**[1]

[1]Scripps Institution of Oceanography, U.C. San Diego, La Jolla, CA, USA

Key Points:

- Earthquake dynamic triggering is ubiquitous in southern California.
- Triggered earthquakes are frequently associated with significant moment-release anomalies and are likely controlled by local processes.
- The choice of statistical test is less impactful for identifying earthquake dynamic triggering using the method developed here.

Corresponding author: Nicolas D. DeSalvio, `ndesalvio@ucsd.edu`

Abstract

Earthquakes can be dynamically triggered by the passing waves of events from disconnected faults. The frequent occurrence of dynamic triggering offers tangible hope in revealing earthquake nucleation processes. However, the physical mechanisms behind earthquake dynamic triggering have remained unclear, and contributions of competing hypotheses are challenging to isolate with individual case studies. Therefore, developing a systematic understanding of the spatiotemporal patterns of dynamic triggering can provide insights into the physical mechanisms, which may aid mitigation of earthquake hazards. Here we investigate earthquake dynamic triggering in Southern California from 2008 to 2017 using the Quake Template Matching catalog and an approach free from assuming an earthquake occurrence distribution. We develop a new set of statistics to examine the significance of seismicity-rate changes as well as moment-release changes. We show that up to 70% of global M≥6 events may have triggered earthquakes in southern California and that the triggered seismicity often occurred several hours after the passing seismic waves. On average, earthquakes are triggered about every 4 days in the region, albeit at different locations. Although adjacent fault segments can be triggered by the same earthquakes, the majority of triggered earthquakes seem to be uncorrelated, suggesting that the process is primarily governed by local conditions. Further, the occurrence of dynamic triggering does not seem to correlate with ground motion (e.g., peak ground velocity) at the triggered sites. These observations indicate that nonlinear processes may have primarily regulated the dynamic triggering cases.

Plain Language Summary

Earthquakes interact with each other, such as mainshocks triggering nearby aftershocks. Earthquake dynamic triggering is a type of interaction where seismic waves from an earthquake trigger other earthquakes beyond several fault lengths, and sometimes, up to thousands of kilometers away. Triggered earthquakes may occur upon the arrival of the seismic waves but may also be delayed hours after the wave passage, suggesting the involvement of time-dependent processes. Identifying delayed cases relies on robust measures of seismicity-rate changes. Here we present a new method that can identify triggering cases without many assumptions. We find that earthquakes in southern California are frequently triggered by distant earthquakes around the globe, and the triggered earthquakes tend to cluster in space and time. Some of the triggered earthquakes are larger in magnitude than the background seismicity. We also find that the triggering incidences do not seem to correlate with the seismic wave characteristics of the distant earthquakes. Our findings suggest that dynamically triggered earthquakes in southern California are likely caused by time-dependent, complex processes.

1 Introduction

While large earthquakes are difficult to predict on a given fault, earthquake occurrence is not completely random (e.g., Abercrombie & Mori, 1996; Ross, Idini, et al., 2019; Trugman & Ross, 2019; Utsu, 1961). Earthquakes interact with each other and often cluster in space and time, such as commonly observed mainshock-aftershock sequences. For example, the 1992 Landers earthquake caused widespread aftershocks that occurred in the near-field (Bosl & Nur, 2002; Harris & Simpson, 1992; Parsons & Dreger, 2000) and the far-field (Gomberg, 1996; Gomberg et al., 2001). The far-field aftershocks were likely triggered by the passing seismic waves, termed earthquake dynamic triggering (Aiken & Peng, 2014; Gomberg & Johnson, 2005; Gonzalez-Huizar & Velasco, 2011). As seismic waves pass through a region, transient dynamic stresses perturb local fault systems that ultimately trigger earthquakes (Hill & Prejean, 2015). This direct correlation between the triggered seismicity and passing waves reflects an observable process that promises tangible hope of deciphering earthquake nucleation mechanisms (Brodsky & van der Elst, 2014). Despite numerous observations of dynamic triggering around the globe, its occurrence conditions and associated precise physical mechanisms remain unclear (e.g., Fan et al., 2021; Meng & Peng, 2014; Velasco et al., 2008). Understanding the physical processes is crucial, as damaging earthquakes can be dynamically triggered (e.g., Pollitz et al., 2012; Uchide et al., 2016; Yoshida, 2016) but are not considered in most seismic hazard models (e.g., Field et al., 2014).

California is an ideal natural laboratory to study earthquake dynamic triggering because of its rich geophysical datasets including high quality catalogs, seismic records, and geodetic observations. The long-term continuous records provide an opportunity to examine the phenomenon by comparing statistical observations to a variety of geophysical observables (e.g., Fan et al., 2021; Miyazawa et al., 2021). Dynamic triggering has been frequently observed in California following M7 earthquakes from different regions (e.g., Aiken & Peng, 2014; Fan et al., 2022; Meng & Peng, 2014; Prejean et al., 2004). Further, geothermal and volcanic areas in the region, such as the Salton Sea Geothermal Field (e.g., Fan et al., 2021), Coso Geothermal Field (e.g., Aiken & Peng, 2014), Geysers Geothermal Field (e.g., Stark & Davis, 1996), and Long Valley Caldera (e.g., Brodsky & Prejean, 2005) seem to be particularly susceptible to dynamic triggering.

In practice, earthquake dynamic triggering is often identified using statistical methods that examine the significance of seismicity-rate changes following candidate trigger earthquakes (e.g., Marsan & Nalbant, 2005; Pankow & Kilb, 2020; Wyss & Marsan, 2011). If the changes are statistically significant, the local earthquakes are inferred to be triggered seismicity (e.g., Marsan & Nalbant, 2005; Pankow & Kilb, 2020; Wyss & Marsan, 2011). Such statistical exercises often assume that local earthquake occurrence is a random and independent process, following a Poissonian distribution (Marsan & Nalbant, 2005; Pankow & Kilb, 2020). However, this assumption is inaccurate for transient, triggered seismicity due to its correlated activity, small sample size, and short duration (e.g., Fan et al., 2021). Fan et al. (2021) experimented using a sampling method to identify statistically significant changes in seismicity-rate. Here we critically reevaluate the approach and construct new statistics that are free from the Poissonian assumption.

There are several families of statistics that have been used to evaluate seismicity-rate changes, and we focus on the two most commonly used statistics for comparison, the β-statistic (Matthews & Reasenberg, 1988) and the Z-statistic (Habermann, 1983). We further develop two additional statistics to investigate earthquake moment-release changes, the β_m-statistic and the Z_m-statistic, which can help identify anomalous occurrence of earthquakes with large magnitudes. The four test statistics were applied to southern California earthquakes to identify cases of dynamic triggering from 2008 to 2017. The statistical results are then compared with seismic waveform characteristics, including peak ground velocity (PGV), peak frequency, kinetic energy, and relative frequency content. Our approach provides a systematic way to investigate the physical mechanisms of earthquake dynamic triggering.

We find that dynamic triggering is common throughout southern California, and about 70% of global M$\geq$6 earthquakes may have triggered seismicity in the region. Significant seismic moment-release is triggered less often, but 52% of the global earthquakes may have triggered anomalies. Triggering of both types, seismicity and moment-release, is widespread in southern California, albeit with strong spatial heterogeneities in their triggering frequency. For example, earthquakes at geothermal fields and the San Jacinto Fault are frequently triggered, but triggering is rarely observed in the Los Angeles Basin. The general triggering patterns are consistent regardless of the test statistic that is used to evaluate the cases. We observe no obvious correlations between the triggering pattern and the instantaneous waveform metrics (e.g., PGV), suggesting that the transient dynamic stress is unlikely the primarily control for the observed cases. Our findings suggest that dynamic triggering in southern California likely involves nonlinear, time-dependent processes that may occur over hours to a day. Triggered seismicity clusters in space and time, indicating that the regulating physical processes likely operate on local length scales on the order of tens of kilometers.

2 Data and Methods

2.1 Catalog and Waveform Data

To study dynamic triggering in southern California, we use the Quake Template Matching catalog (QTM) with a detection threshold of 12 times the median average deviation (MAD) for local seismicity (Ross, Trugman, et al., 2019). This catalog has nearly 900 thousand earthquakes across southern California. We opt to use the 12 times MAD catalog over the 9.5 times MAD QTM version because it is more robust and is free from occasional day-long seismicity bursts that could be misinterpreted as triggering by our algorithm (e.g., Moutote et al., 2021).

We consider global M≥6 earthquakes as possible candidate trigger earthquakes, which are obtained from the International Seismological Centre (ISC) catalog (International Seismological Centre, 2022). The catalog is downloaded from the Incorporated Research Institutions for Seismology Data Management Center. We consider 1,580 M≥6 candidate trigger earthquakes between 2008 and 2017. To achieve a uniform sampling procedure, we do not examine earthquakes from January to June 2008 and July to December 2017; the details are described in Section 2.3. We also do not consider global earthquakes that occurred in the two months after the 2010 El Mayor Cucapah Earthquake due to its extended triggering behavior in southern California (e.g., Inbal et al., 2017; Meng & Peng, 2014). In total, 1,388 candidate earthquakes are investigated in this study.

To investigate local ground motions caused by the candidate trigger earthquakes, we examine the three-component, broadband, velocity seismograms recorded by stations in the region of interest, which roughly brackets southern California from 31° to 38° in latitude and from -123° to -113° in longitude. For each candidate event, we downloaded data from 10 minutes before the candidate earthquake origin time to two hours after. Thus, the data contains a 10-minute pre-event noise window and a two-hour signal window, which include body wave phases and minor arc surface wave phases. Waveform data is downloaded using the Obspy Mass Downloader tool (Beyreuther et al., 2010).

2.2 Study Area

We focus on identifying dynamic triggering in southern California where the QTM catalog continuously reported local earthquakes (Figure 1). Ideally, the region would be gridded to have uniform coverage of southern California. Such a gridding scheme would lead to about 1,750 grids using a 0.2° separation distance. In practice, we take advantage of the well-documented surface fault traces from the Southern California Earthquake Center Community Fault Model (CFM) (Marshall et al., 2022) to identify sites of interest. We first discretize the study area into 429 circular sites centering on the CFM surface traces (Figure 1a). Each site has a radius of 20 km and we space them ∼20 km apart such that each grid overlaps by ∼50% in area (inset, Figure 1a). Overlapping the grids avoids a cluster of triggered seismicity being split by a region border, leading to possible misidentification of dynamic triggering. Despite centering the grids on the CFM fault traces, our gridding strategy ensures the entire study area is nearly contained within the boundaries of the grid points. In each grid, we associate the QTM earthquakes contained within its footprint to the grid and estimate the magnitude of completeness (M_c) for the earthquakes using both the maximum-curvature and goodness-of-fit methods (Wiemer, 2000). The estimate with the greater value is taken as the M_c for the grid (Figure 1c). When evaluating dynamic triggering for the grids, we only consider earthquakes with magnitudes greater than the M_c for the individual sites. Grid points containing less than 500 earthquakes above M_c during the study period are not evaluated to ensure reliable results, leaving 222 grid points (Figure 1b-c). Our gridding approach leads to almost eight times less grid points than using an equal-separation uniform gridding scheme, which greatly improves the computational efficiency.

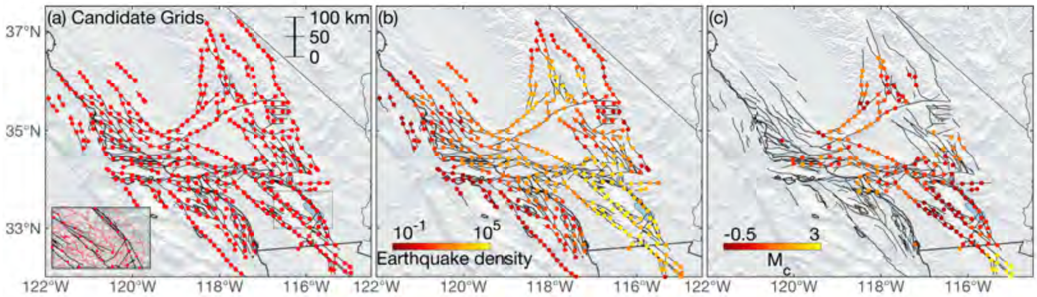

Figure 1: Study area in southern California. (a) Map of locations (grid points) where earthquake dynamic triggering is evaluated. Gray lines show surface fault traces from the Southern California Earthquake Center Community Fault Model (CFM). Each red dot represents a site of interest covering a region within a 20 km radius. Gray box shows the region highlighted in the inset demonstrating the boundaries and overlapping of the grid points near the Salton Sea area. (b) Earthquake density, representing the average number of earthquakes per year that have magnitudes above the M_c within each grid point. (c) Magnitude of completeness of the grid points. Grid points that have less than 500 earthquakes during the study period are removed.

2.3 Dynamic Triggering Identification

We hypothesize that statistically significant seismicity-rate changes within the immediate 24 hours following a candidate earthquake are likely caused by earthquake dynamic triggering. The seismicity-rate changes are examined using two different statistics: the β-statistic (Matthews & Reasenberg, 1988) and the Z-statistic (Habermann, 1983). Furthermore, we modify the two statistics to evaluate significant seismic moment-release anomalies, which we term the β_m-statistic (Section 2.3.1) and the Z_m-statistic (Section 2.3.2). The statistics compare seismicity or seismic moment within two different time periods, δ_a and δ_b, where δ_a is the time period of interest and δ_b is the reference time period. For the time period of interest (δ_a), we evaluate seismicity-rate and moment-release changes within 2-, 6-, 12-, and 24-hour time windows at each grid after the candidate earthquake origin time. The time-window length can be adjusted for customized applications. We select the 2-hour window to monitor possible instantaneous triggering and use the other three windows to characterize delayed dynamic triggering. It is worth noting that the instantaneous-triggering window length can be shorter, albeit at the cost of the robustness of the statistics due to the small number of samples. The reference time period (δ_b) is set to be the immediate 30 days before and after the candidate earthquake for the β- and β_m-statistics (a total of 60 days) and the immediate 30 days before the candidate earthquake for the Z- and Z_m-statistics. Positive statistic values suggest an increase in seismicity-rate or moment-release and the negative values suggest a decrease. Our procedure aims to identify spatiotemporal dependent thresholds to quantify the significance of the changes in seismicity and moment-release after a candidate trigger earthquake.

2.3.1 β- and β_m-statistics

The β-statistic characterizes seismicity-rate changes with respect to a reference time period that is normalized by its standard deviation (a dispersion parameter), which can be given by

$$\beta = \frac{N_a - \bar{N}_a}{\sigma_a}, \tag{1}$$

where N_a is the number of earthquakes during the time period of interest (δ_a), and $\bar{N}_a$ and σ_a are its expected value and standard deviation during the reference time period (δ_b). The expected value can be obtained analytically as $\bar{N}_a = \Lambda = N_b \cdot \frac{\delta_a}{\delta_b}$. When assuming that earthquake occurrence follows a Poisson distribution, the standard deviation is the square root of the expected value, or $\sigma_a = \sqrt{\Lambda}$. Alternatively, $\bar{N}_a$ and σ_a can be estimated empirically from the statistical population of N_a. Specifically, we randomly reposition the δ_a time window within the δ_b time window 10,000 times, leading to 10,000 samples of N_a. The population expected value and standard deviation are estimated as

$$\bar{N}_a = \frac{1}{M}\sum_{i=1}^{M} N_i, \tag{2}$$

$$\sigma_a = \sqrt{\frac{1}{M-1}\sum_{i=1}^{M}(N_i - \bar{N}_a)^2}, \tag{3}$$

where M is the number of samples (10,000 in this study) and N_i is the earthquake number in the i-th reposition time window. The obtained N_a samples are converted to their corresponding β-values (Equation 1), and we term this set of values B. The β-statistic of the original time period of interest is denoted as β_0. The procedure is similar to that outlined in Fan et al. (2021), but $\bar{N}_a$ and σ_a are obtained empirically from the sampled population and our new procedure is free from earthquake occurrence assumptions. We construct the N_a samples and their associated β-values for every candidate trigger earthquake at every grid and time window.

Typically, the β-statistic is considered 95% significant when $\beta \geq 1.96$ (Wyss & Marsan, 2011). In this case, the β-statistic attends to a zero-mean, unit-variance Gaussian distribution, which is a result of the Poissonian assumption about seismicity occurrence (Wyss & Marsan, 2011). However, the assumption may be inaccurate and the $\beta \geq$ 1.96 threshold may cause erroneous identifications of significant seismicity-rate changes (e.g., Fan et al., 2021; Marsan & Nalbant, 2005; Pankow & Kilb, 2020; Prejean & Hill, 2018). Therefore, we adopt the procedure described in (Fan et al., 2021) to evaluate the statistical significance of β_0. To assess its statistical significance, we use the β-statistic values (B) to construct the B-distribution, a β-statistic probability density function (PDF, e.g., Figure 2c), by using the kernel density estimator (Bowman & Azzalini, 1997; Fan et al., 2021; Silverman, 1986). The 95^{th} percentile from the PDF accords with a 95% significance level, and the value is taken as one threshold, $\beta^a_{95\%}$, for evaluating the significance of the seismicity-rate changes. We choose the 95^{th} confidence level as suggested in Fan et al. (2021) and emphasize that the value of the parameter is chosen subjectively. One can and sometimes should use a different value, but this is dependent on the specifics of individual cases (e.g., Cattania et al., 2017; Pankow & Kilb, 2020). Additionally, we calculate β_b as the β-statistic for seismicity in a time window that has equal length of δ_a but immediately precedes the candidate event origin time. We consider the seismicity-rate change statistically significant for the given time window δ_a and grid point if $\beta_0 >$ $\beta^a_{95\%}$ and $\beta_0 > \beta_b$ (e.g., Figure 2c). For such cases, we hypothesize that the seismicity-rate change was caused by dynamic triggering.

When computing the β-statistic for seismicity-rate changes, earthquakes with different magnitudes are treated equally as only their occurrences are evaluated. However,

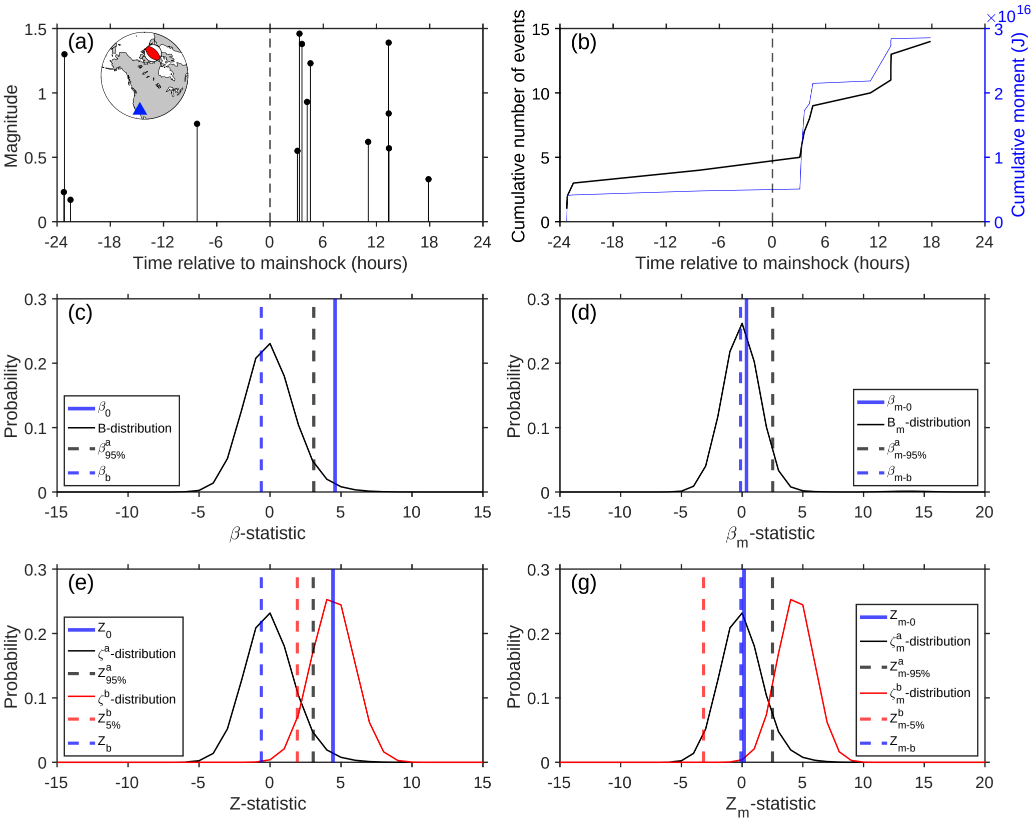

Figure 2: Example statistic distributions for δ_a as 6 hours. (a) Earthquake occurrence at a grid point footprint near the Coso Geothermal Field within 24 hours of a candidate trigger earthquake. Inset: candidate trigger earthquake (2017-01-08 23:47:13.66, M6.0, ISC ID: 611831502) and the study site. (b) Cumulative seismicity and moment-release within the grid point boundary and within 24 hours of a candidate trigger earthquake. (c) β-statistic distribution (B-distribution), β_0, and the associated thresholds β_b and $\beta^a_{95\%}$. (d) β_m-statistic distribution (B_m-distribution), β_{m-0}, and the associated thresholds β_{m-b} and $\beta^a_{m-95\%}$. (e) Z-statistic distributions (ζ^a- and ζ^b-distributions), Z_0, and the associated thresholds Z_b, $Z^a_{95\%}$, $Z^b_{5\%}$. (f) Z_m-statistic distributions (ζ^a_m- and ζ^b_m-distributions), Z_{m-0}, and the associated thresholds Z_{m-b}, $Z^a_{m-95\%}$, $Z^b_{m-5\%}$.

one magnitude difference causes about 31 times more seismic moment-release, and β-statistics based on earthquake occurrence would underestimate the impact of larger earthquakes. To detect statistically significant seismic moment-release anomalies that may have been caused by earthquake dynamic triggering, we develop a new moment-release statistic, the β_m-statistic. We sum the seismic moments of earthquakes in δ_a, denote it M_a, and compare it to the seismic moment-release in the reference time period δ_b ($\bar{M}_a$ and σ_{M_a}). For simplicity, the magnitude (m) in the QTM catalog is taken as the moment-magnitude for this calculation, and the absolute moment-release estimate is therefore likely biased (e.g., Shearer et al., 2022). However, identification of moment-release anomalies is not impacted because the statistic focuses on relative differences. The β_m-statistic is defined as:

$$\beta_m = \frac{M_a - \bar{M}_a}{\sigma_{M_a}}, \tag{4}$$

where

$$M_a = \sum_{i=1}^{N_a} 10^{1.5m_i+9.1}. \quad (5)$$

The procedure to sample the β_m-statistic population and obtain B_m is similar to that of B. We estimate the population expected value ($\bar{M}_a$) and standard deviation (σ_{M_a}) from B_m and build the B_m-distribution to identify its statistical-significance threshold, $\beta^a_{m-95\%}$ (e.g., Figure 2d). The sampling and construction procedures are similar to those outlined for the β-statistic. We then consider that the moment-release change is statistically significant for the given time window δ_a at a grid when $\beta_{m-0} > \beta^a_{m-95\%}$ and $\beta_{m-0} > \beta_{m-b}$ (e.g., Figure 2d).

2.3.2 *Z*- and Z_m-statistics

Similar to the β-statistic, the Z-statistic can also measure the degree of seismicity-rate changes in comparison to the background seismicity-rate (Habermann, 1981, 1983). In this study, we examine the Z-statistic and compare the results with the β-statistics for the same earthquakes. The Z-statistic is a symmetric measure of the seismicity-rate changes because its normalization depends on seismicity in both the time period of interest and reference period (Wyss & Marsan, 2011). Following Habermann (1983), we compute the Z-statistic as

$$Z = \frac{N_a/\delta_a - N_b/\delta_b}{\sqrt{\left(\sigma_a/\delta_a\right)^2 + \left(\sigma_b/\delta_b\right)^2}}, \quad (6)$$

where N_b is the number of earthquakes within δ_b, σ_b is the standard deviation associated with the distribution of N_b, and N_a, δ_a, δ_b, and σ_a are defined as above. The quantities N_a/δ_a and N_b/δ_b represent the mean seismicity-rates during their respective time periods. The Z-statistic is free from seismicity occurrence assumptions if σ_a and σ_b are estimated empirically. Similar to the β-statistic sampling procedure, we sample the N_b population by randomly repositioning the δ_b window 10,000 times within one year of the candidate trigger earthquake, ranging from 6 months before to 6 months after the event origin time. We estimate the population statistics for the N_b population, particularly the expected value and standard deviation (σ_b), which are then used to compute a Z-statistic for the candidate trigger earthquake at a given grid point. We note that the sampling procedure implicitly assumes that σ_a and σ_b are invariant throughout their respective sampling time periods, which is 30 days for σ_a and one year for σ_b.

Similar to the β-statistic, the Z-statistic also attends to a zero-mean, unit-variance Gaussian distribution when the earthquake occurrence follows a Poisson distribution. In such a case, the seismicity-rate increase is statistically significant at the 95% confidence level when $Z \geq 1.96$ (Aiken et al., 2018; Wyss & Marsan, 2011). In our approach, we require the Z-statistic exceed $Z^a_{95\%}$, Z_b, and $Z^b_{5\%}$ (e.g., Figure 2e). The $Z^a_{95\%}$ threshold is the 95^{th} percentile of a Z-statistic distribution (ζ^a-distribution) constructed by randomly sampling N_i for a window length of δ_a within 30 days before and after the candidate trigger earthquake origin time. We hold N_b constant as the seismicity in the 30 days before the candidate trigger earthquake. The Z_b threshold is for seismicity in a time window that has equal length of δ_a but immediately precedes the candidate event origin time. The $Z^b_{5\%}$ is the 5^{th} percentile obtained from a Z-statistic distribution (ζ^b-distribution) constructed by sampling N_i for a window length of δ_b within 6 months before and after the candidate trigger earthquake origin time. We keep N_a constant as the seismicity within the δ_a window after the origin time.

Similar to the β_m-statistic, we design the Z_m-statistic to detect seismic moment-release anomalies. The Z_m-statistic is given by:

$$Z_m = \frac{M_a/\delta_a - M_b/\delta_b}{\sqrt{\left(\sigma_{Ma}/\delta_a\right)^2 + \left(\sigma_{Mb}/\delta_b\right)^2}}, \tag{7}$$

where M_b follows Equation 5 but for the δ_b time period. The sampling procedure for the Z_m-statistic is similar to that of the Z-statistic (e.g., Figure 2g), and we define a similar set of thresholds to evaluate the statistical significance of the moment-release anomalies, including, $Z_{m-0} > Z^a_{m-95\%}$, $Z_{m-0} > Z_{m-b}$, and $Z_{m-0} > Z^b_{m-5\%}$ (e.g., Figure 2g).

Taking the January 8, 2017 M6 Queen Charlotte earthquake as an example trigger earthquake (Figure 2a), we find that the earthquake may have triggered seismicity within the Coso Geothermal Field within 6 hours of its origin time (Figure 2 and Table S1), which is indicated by both the β-statistic and Z-statistic. However, neither the β_m- or Z_m-statistic suggests anomalous moment-release change at the location during the 6-hour time window.

2.4 Waveform Metrics

We inspect the velocity waveforms of the candidate trigger earthquakes in southern California and measure four instantaneous waveform metrics: peak ground velocity, peak frequency, kinetic energy, and relative frequency content. We measure the peak ground velocity (PGV) in two frequency bands, 0.01–0.1 Hz and 1–5 Hz (Figure 3a-b). After downloading the records, we first remove the instrument response and decimate the data to a 20 Hz sampling rate. Then we band-pass filter the data and compute their envelope functions. The maximum envelope amplitudes are measured in both the pre-event noise window (10 minutes) and the signal window (2 hours) independently for all three channels at each station. A signal-to-noise ratio (SNR) is computed as the ratio between the maximum amplitudes of the signal and noise windows for each channel. We only use traces that have a SNR greater than 5 for both the low- and high-frequency bands to measure the waveform metrics. If all three channels at a station have a SNR greater than the threshold, we take the geometric mean of the qualified waveform envelopes and calculate a single PGV value for the station. We use the same qualified traces for the other calculated metrics and discard the rest. Figure 3a-b demonstrates an example of measuring the PGV values of the 2017 M6 earthquake in the Queen Charlotte Islands, Canada at CI.JRC2 (near Coso) in the two frequency bands. The 0.1 to 1 Hz frequency band is not investigated here as the noise level is high due to microseisms.

We measure the peak frequency of qualified ground velocity records at each station caused by the candidate trigger earthquakes (e.g., Figure 3c). For an earthquake-station pair, we estimate the power spectrum of the waveform in the signal window for each channel using the multitaper method with 11 Slepian tapers (Thomson, 1982). Given the earthquake-station distance, we focus on the 0.01–5 Hz frequency band and compute the geometric mean of the power spectra from the three channels. The corresponding frequency of the maximum power is taken as the peak frequency.

For the kinetic energy calculation, the qualified seismic data are first band-pass filtered at 0.01 to 10 Hz (Figure 3d), and the root-mean-square (RMS) values are computed for each channel in the signal window. This leads to three measurements in total for each station. We then record the RMS-square-sum of the signal window as the kinetic energy per unit mass for the earthquake-station pair. Figure 3d shows an example of measuring the kinetic energy for the M6 Queen Charlotte earthquake at CI.JRC2.

Lastly, we examine the relative frequency content of the passing waveforms. We modify the Frequency Index (FI) metric (Buurman & West, 2010) given by:

$$\mathrm{FI} = \log_{10}\left(\frac{\bar{A}_u}{\bar{A}_l}\right), \tag{8}$$

where $\bar{A}_l$ is the mean power spectrum amplitude in a lower frequency band and $\bar{A}_u$ in an upper frequency band. We replace the mean spectral amplitudes with the integrated total power within each frequency band, which is a more stable calculation. We refer to this as the Frequency Content Ratio (FCR):

$$\mathrm{FCR} = \log_{10}\left(\frac{\int_{f_{l1}}^{f_{l2}} S(f)\, df}{\int_{f_{u1}}^{f_{u2}} S(f)\, df}\right) = \log_{10}\left(\frac{P_l}{P_u}\right) \tag{9}$$

where $S(f)$ is the geometric mean of the power spectra of the three channels and f_{l1}, f_{l2}, f_{u1}, f_{u2} define the lower and upper frequency bands. Here the lower frequency band is taken as 0.01–1 Hz, and the upper frequency band is 1–5 Hz (Figure 3c). We place the lower band in the numerator to ensure that the FCR estimates are primarily positive for teleseismic earthquakes, due to their more prominent low frequency signals.

The waveform metrics are computed for each station independently, and the measurements for each candidate trigger earthquake are interpolated to nearby grid points. For each grid point, we obtain the median of the waveform metrics at the five nearest stations within 100 km (Figure 4). We do not make measurements at grid points when less than three stations are available.

3 Results

In this section, we detail our observations of seismicity and moment-release anomalies in southern California associated with the candidate earthquakes, focusing on their spatial (Section 3.1) and temporal (Section 3.2) patterns. Since the seismicity-rate anomalies are identified at a 95% confidence level, we omit grid points that triggered less than 5 times from our results and discussion (see Section 4.1 for details). In general, we find that up to 70% of candidate trigger earthquakes caused dynamic triggering in southern California from 2007 to 2017. We find that triggering occurrence varies from fault to fault, and triggering occurs most often at the Salton Sea and Coso geothermal fields as well as the San Jacinto Fault. Furthermore, we identify temporal patterns evolving at multiple scales, from instantaneous to delayed responses, and from intermittent occurrence at a given site to frequent triggering in southern California. Lastly, we examine the waveform metrics of candidate trigger earthquakes at sites with both normal and anomalous seismicity and moment-release rate changes.

3.1 Spatial Triggering Patterns

Dynamic triggering likely occurs frequently in southern California. About 70% of the candidate trigger earthquakes associate with seismicity anomalies that are identified using the β-statistic (Figure 5). Given the close temporal correlation, we consider that the anomalies are dynamically triggered by the earthquakes. Spatially, seismicity at 54% of the grid points (a total of 222 points) was triggered at least five times. Using the Z-statistic, we find that 60% of candidate earthquakes associate with seismicity anomalies, and seismicity at 42% of the grid points was likely dynamically triggered five or more times. Anomalous seismic moment-release is less commonly observed to associate with the candidate earthquakes, with the β_m- and Z_m-statistics identifying triggered seismicity after 52% and 32% of the candidate earthquakes, respectively. Spatially,

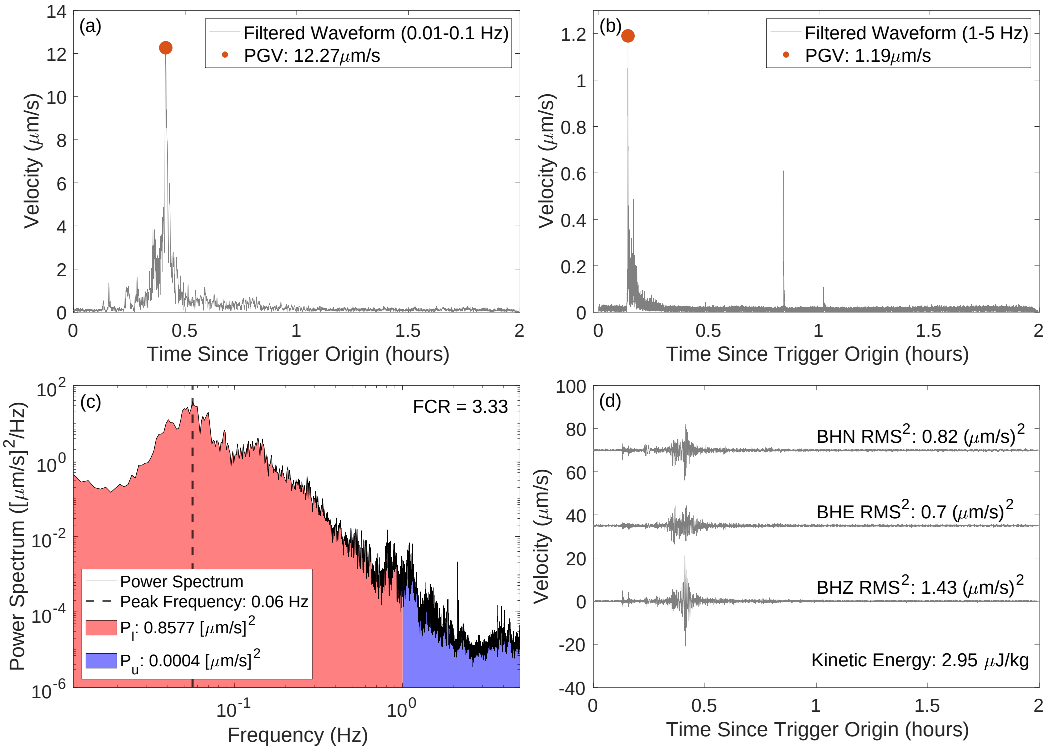

Figure 3: Waveform metric calculations of the January 8, 2017 M6 Queen Charlotte earthquake at station CI.JRC2, near the Coso Geothermal Field. (a–b) Waveform envelopes (geometric mean of the three-component envelopes) at the 0.01–0.1 Hz and 1–5 Hz frequency bands. The maximum amplitudes of the envelopes are taken as the PGV of the frequency bands, respectively. (c) Geometric mean of the three-component power spectra. Peak frequency corresponds to the frequency yielding the maximum value of the spectrum. FCR is calculated using the integral results P_l in the 0.01–1 Hz band and P_h in the 1–5 Hz band (Equation 9). (d) Band-pass filtered waveforms. Square sum of the three-component RMS values is taken as the kinetic energy per unit mass. The BHE data is shifted 35 $\mu m/s$ upwards, and BHN 70 $\mu m/s$.

moment-release anomalies are identified at 45% and 33% of grid points using the β_m- and Z_m-statistics, respectively.

Spatial patterns of triggering occurrence for the four test statistics are highly heterogeneous (Figure 5). Here triggering occurrence counts the number of candidate trigger earthquakes that caused seismicity or moment-release anomalies in any of the four time windows (δ_a as 2, 6, 12, or 24 hours) during the study period. The Salton Sea Geothermal Field (SSGF), Coso Geothermal Field (CGF), and San Jacinto Fault (SJF) most frequently experienced seismicity-rate anomalies identified by the β- and Z-statistics, which are likely caused by the passing waves (Figure 5a,c). Seismicity at the Elsinore Fault, the merging connection of the San Andreas and San Jacinto Faults, the southern San Andreas, the southern Sierra Nevada, and the Ridgecrest region is frequently triggered by remote earthquakes. In contrast, moment-release anomalies that are identified by the β_m- and Z_m-statistics have different spatial patterns than those of the seismicity-rate anomalies (Figure 5b,d). Specifically, the SSGF and CGF are less likely to have moment-

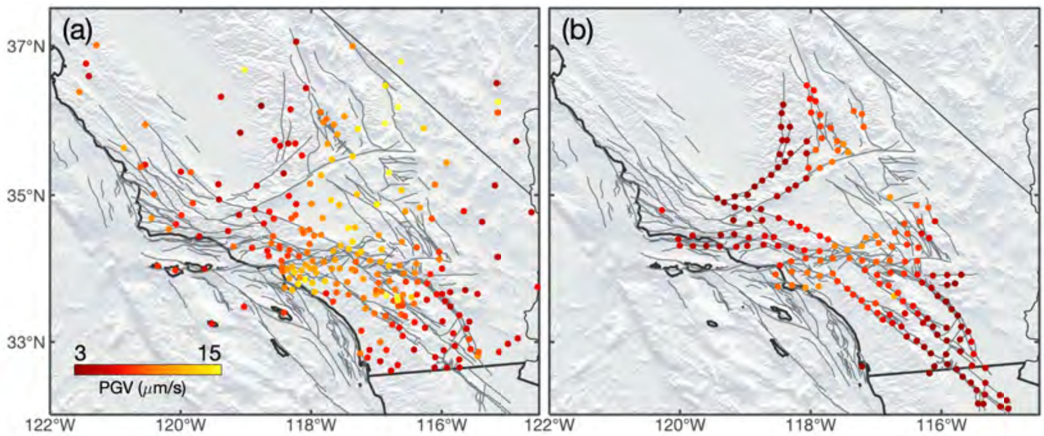

Figure 4: Example interpolation of PGV values in the 0.01-0.1 Hz band for the January 8, 2017 M6 Queen Charlotte earthquake. (a) Measured values at each station. (b) Interpolated values for qualified grid points.

release anomalies than SJF, and their triggering occurrence is comparable to that of the Elsinore Fault (Figure 5b,d). Moment-release anomalies are less frequently observed at the merging connection of the San Andreas and San Jacinto Faults, Ridgecrest area, and southern San Andreas fault (Figure 5b,d).

We observe more delayed (6 to 24 hour windows, Figures S1, S2 and 7) than instantaneous triggering cases (2 hour, Figure 6). Such triggering occurrence differences between the instantaneous and delayed cases are observed for all four statistics. While instantaneous triggering cases are often difficult to observe because the catalog completeness may suffer due to the passing wave coda, our results show that delayed dynamic triggering of both seismicity and moment-release occurs frequently in southern California at multiple sites. For example, 83% of the β-statistic seismicity-rate anomalies are delayed cases, and 79% of the Z-statistic cases are delayed, showing strong agreement. Further, 91% and 89% of moment-release anomalies are delayed cases from the β_m- and Z_m-statistics, respectively. Around half of instantaneously triggered cases of seismicity also extended into later hours. Specifically, 51% and 46% of the instantaneous cases, as identified by the β- and Z-statistics, had extended responses reaching up to and beyond the 6-hour window. Intriguingly, more than half of the instantaneously triggered moment-release extended into later hours, with 63% and 59% of cases for the β_m- and Z_m-statistics, respectively.

Our triggering occurrence patterns are similar to the triggerability pattern in Miyazawa et al. (2021) with some differences at the Beta Offshore Platform, San Andreas Fault, and the southern Sierra. Miyazawa et al. (2021) investigates dynamic triggering occurrence in southern California using the same QTM catalog. Differently, Miyazawa et al. (2021) adapts the method in van der Elst and Brodsky (2010) and inverts for triggerability based on distributions of separation times between the candidate earthquake and the local earthquakes immediately preceding and succeeding the candidate. The discrepancies at a few sites in our results are likely because we examine seismicity in the entire time window and not just the temporally closest events. Our study corroborates the findings of Velasco et al. (2008), which finds that triggering is ubiquitous around the globe and independent of tectonic environment. Velasco et al. (2008) reports a triggering rate of 80% for M≥7 candidates.

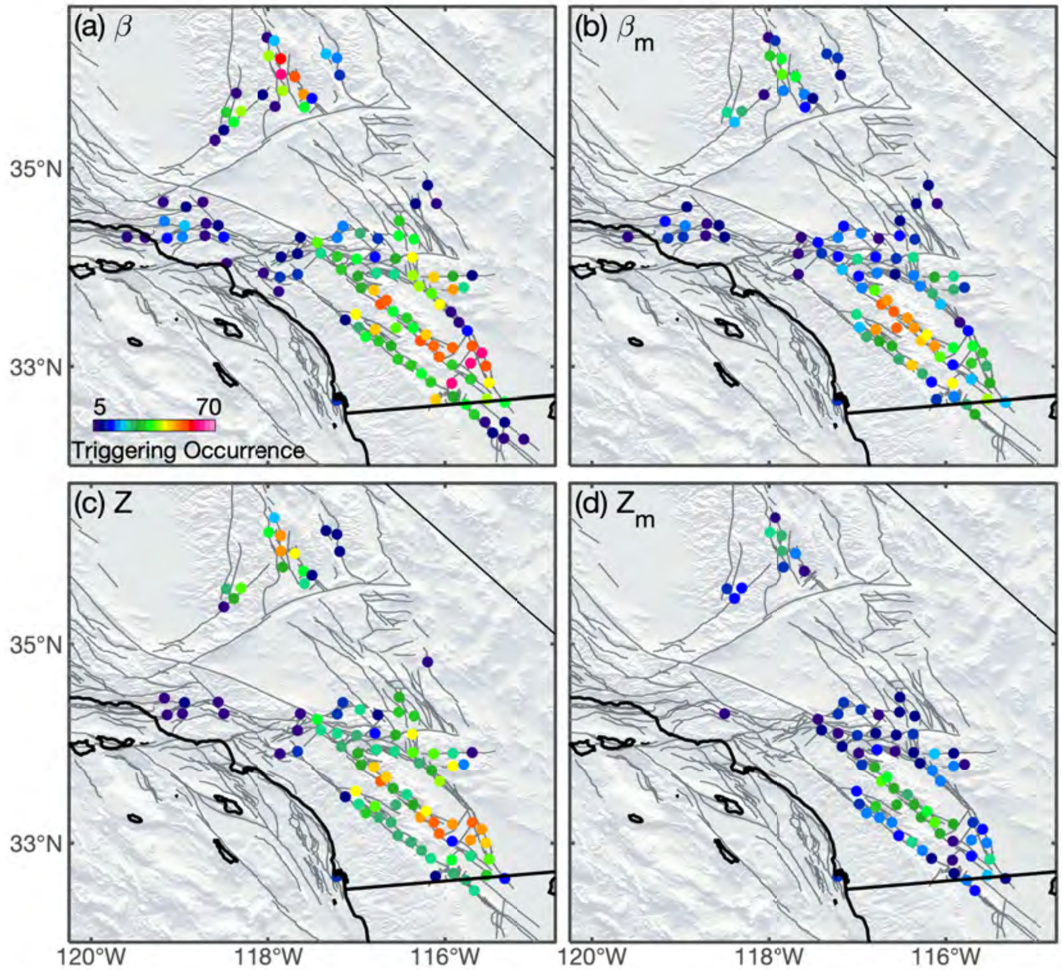

Figure 5: Spatial triggering patterns in southern California. Triggering occurrence identified using the β-statistic (a), β_m-statistic (b), Z-statistic (c), and Z_m-statistic (d) are denoted in color. Triggering occurrence is the number of candidate trigger earthquakes that caused seismicity or moment-release anomalies in any of the four time windows.

3.2 Temporal Triggering Patterns

To investigate the temporal evolution of dynamic triggering processes, we inspect time intervals between consecutive triggering incidences at every grid point, denoted as local recurrence times. We also investigate consecutive time intervals of dynamic triggering cases in southern California for any grid point, which we term interevent time.

Dynamic triggering occurs at individual grid points intermittently, often on the timescale of months to years (e.g., Figure 8). The spatial pattern of recurrence times correlates with that of triggering occurrence and there are strong heterogeneities from site to site (Figures 5 and 8). The median recurrence times range from tens of days to years for different sites, and adjacent sites tend to have similar recurrence times. For example, the Salton Sea Geothermal Field, Coso Geothermal Field, and San Jacinto Fault have frequent incidences of seismicity-rate anomalies, with average recurrence times around 2–2.5 months (Figure 8). In contrast, we rarely observe seismicity-rate anomalies in the LA Basin, showing gaps on the order of years between triggering cases (Figure 8). Similar to the spatial pattern of moment-release anomalies (Figure 5), the geothermal fields

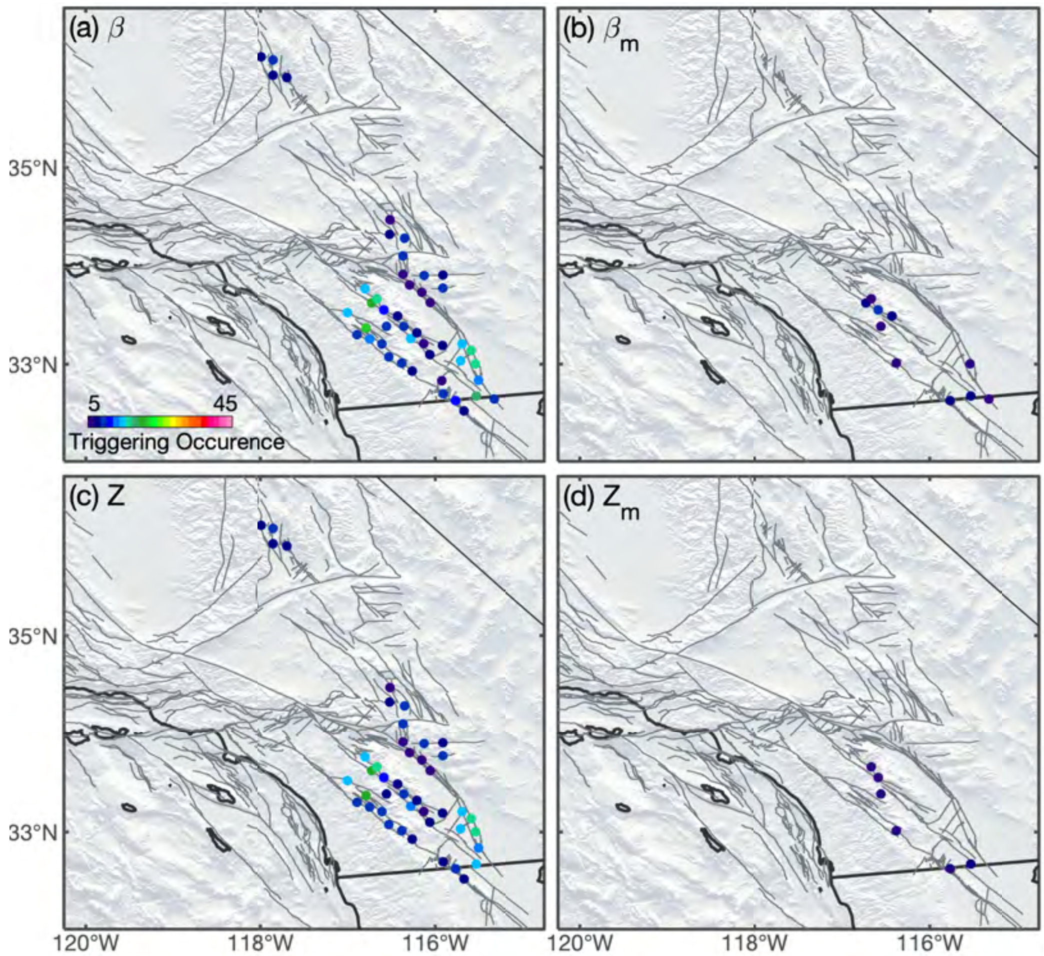

Figure 6: Triggering occurrence during the 2 hour (δ_a=2) time window using the β-statistic (a), β_m-statistic (b), Z-statistic (c), and Z_m-statistic (d).

do not have significant moment-release anomalies very often (Figure 8). For example, Figure 9a–d shows the distributions of recurrence times for a few notable locations using the β-statistic. Similar figures of other statistics are included in the Supplementary Material.

On average, dynamically triggered seismicity is identified using the β- and Z-statistics at one or more of the grids in southern California every 3.4 and 3.9 days, respectively. Similarly, moment-release anomalies from the β_m and Z_m-statistics occur every 4.5 and 7.4 days on average in the region, respectively. The distributions of interevent times in southern California are summarized in Figure 9e–h, showing that dynamic triggering occurs frequently in southern California on a scale of every few days. We also explored temporal variations of the recurrence and interevent times in the region during the study period, e.g., whether the triggering patterns evolve with the occurrence of the 2010 El Mayor Cucapah earthquake and the 2019 Ridgecrest earthquakes. We do not identify significant variations over the triggering patterns using the QTM catalog.

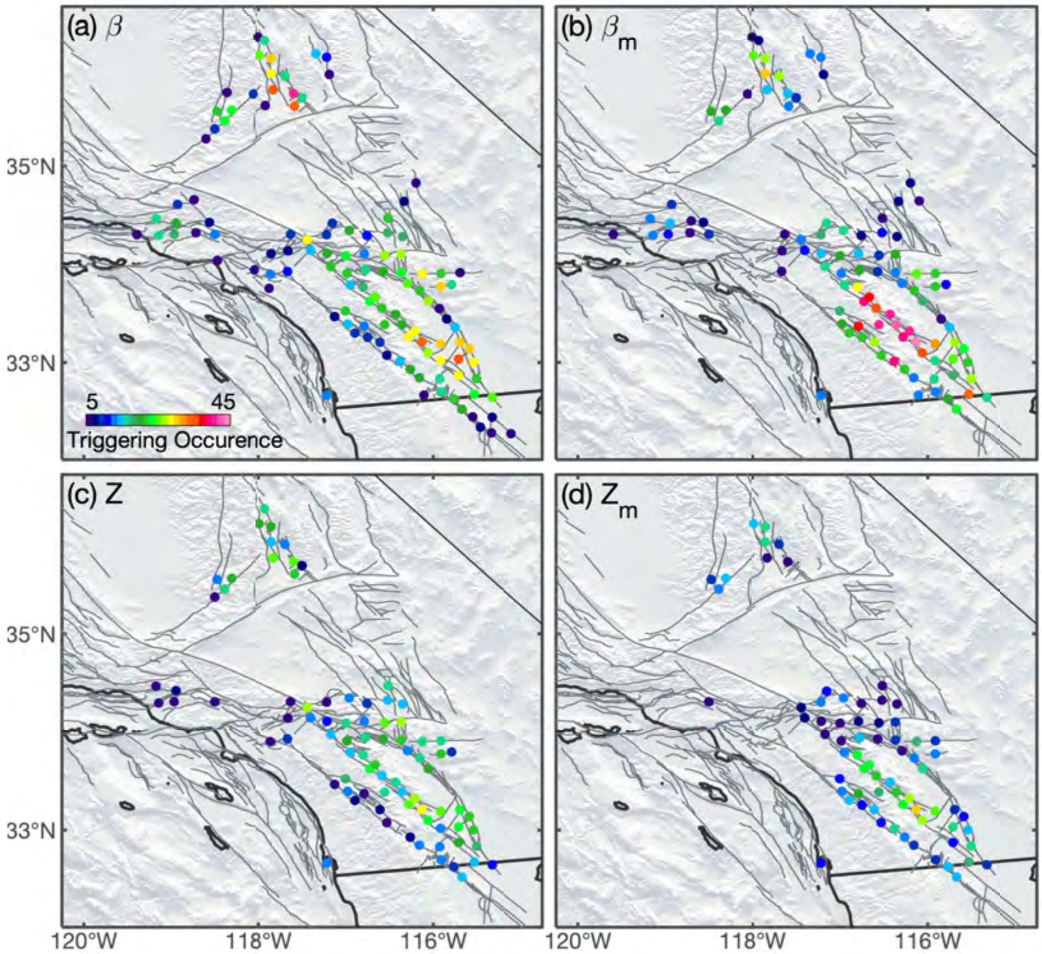

Figure 7: Triggering occurrence during the 24 hour (δ_a=24) time window using the β-statistic (a), β_m-statistic (b), Z-statistic (c), and Z_m-statistic (d).

3.3 Waveform Results

We measure waveform metrics (e.g., Figures 3-4) at all 222 grid points for the 1388 candidate trigger earthquakes, including events and grids that do not associate with seismicity-rate and moment-release anomalies (Figures 10-12). The measurements are then grouped into three categories: instantaneous (2-hour window), delayed (6- to 24-hour windows), and non-triggering. We examine distributions of waveform metrics for the three groups to evaluate their possible differences. For PGV in the 0.01–0.1 Hz band we observe no significant differences between the three distributions for the four test statistics (Figure 10a–d). Interestingly, instantaneous triggering cases seem to have a larger minimum PGV than the delayed cases in the 1–5 Hz frequency band (Figure 10e–h). The 1–5 Hz PGV distributions shift towards higher values compared to the delayed and non-triggering distributions in Figure 10e–h, most clear for the β_m- and Z_m-statistics. On average, a PGV threshold of 0.2 and 0.5 $\mu m/s$ in the 1–5 Hz band seems to be observed for the instantaneously triggered seismicity and moment-release anomalies, respectively. The threshold does not exclude occurrence of delayed and non-triggering cases as there are incidences of both groups with similar or greater PGV values. The observed high-frequency threshold is also observed in the FCR metric, manifesting as a leftward shift of the instanta-

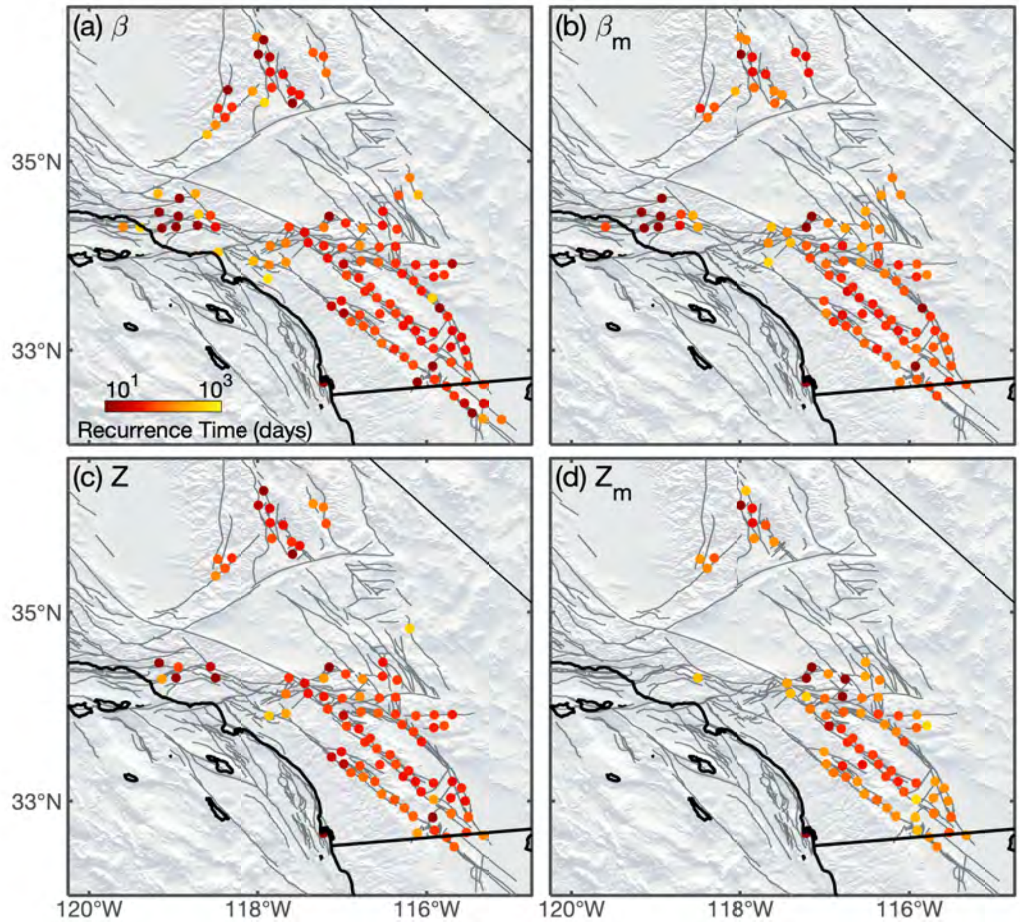

Figure 8: Median recurrence time at the qualified grid points using the β-statistic (a), β_m-statistic (b), Z-statistic (c), and Z_m-statistic (d).

neous distributions (Figure 11e–h), which suggests higher PGV values at high frequencies and therefore lower FCR values. There are no obvious differences in the distributions of the peak frequency or kinetic energy for the four test statistics (Figures 11a–d and 12). In summary, the waveform characteristics of the candidate earthquakes cannot deterministically differentiate the triggering incidence from non-triggering cases or separate instantaneous and delayed cases.

4 Discussion

Dynamically triggered seismicity occurs ubiquitously in southern California, albeit with strong occurrence heterogeneities in space and time. Moment-release anomalies share similar spatiotemporal patterns with the seismicity-rate anomalies but occur less frequently. In this section we will first evaluate the identification uncertainty and limitations (Section 4.1), and then examine possible triggering mechanisms (Section 4.5).

4.1 Uncertainty and Resolution

In this study, we identify seismicity-rate and moment-release anomalies at a 95% confidence level, and the identified anomalies are interpreted to associate with candidate

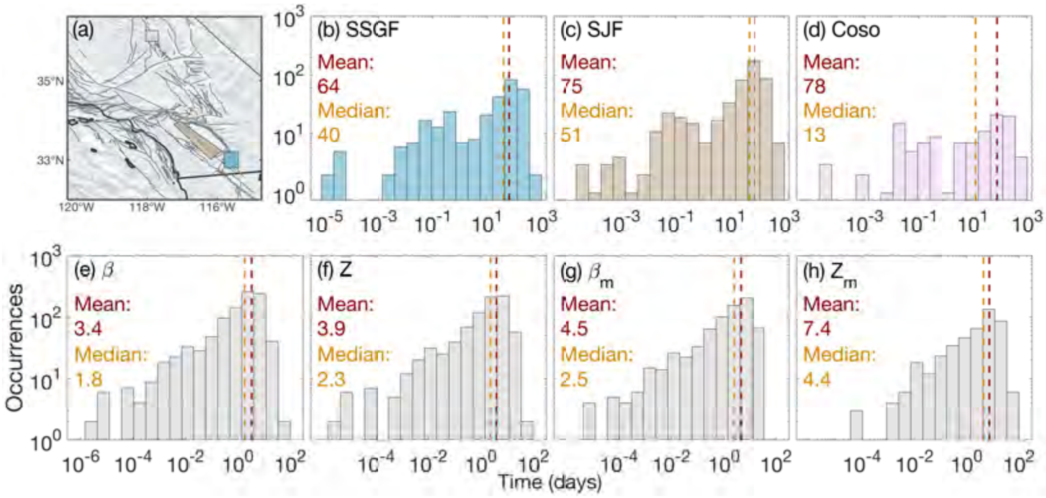

Figure 9: Distribution of triggering recurrence times at example sites and distribution of interevent times for southern California. (a) Map view of three sites. Each polygon may include more than one grid point, e.g., the San Jacinto Fault Zone. (b–d) Recurrence times at the Salton Sea Geothermal Field (b), the San Jacinto Fault Zone (c), and the Coso Geothermal Field (d). (e–f) Interevent times for southern California obtained using the the β-statistic (e), Z-statistic (f), β_m-statistic (g), and Z_m-statistic (h).

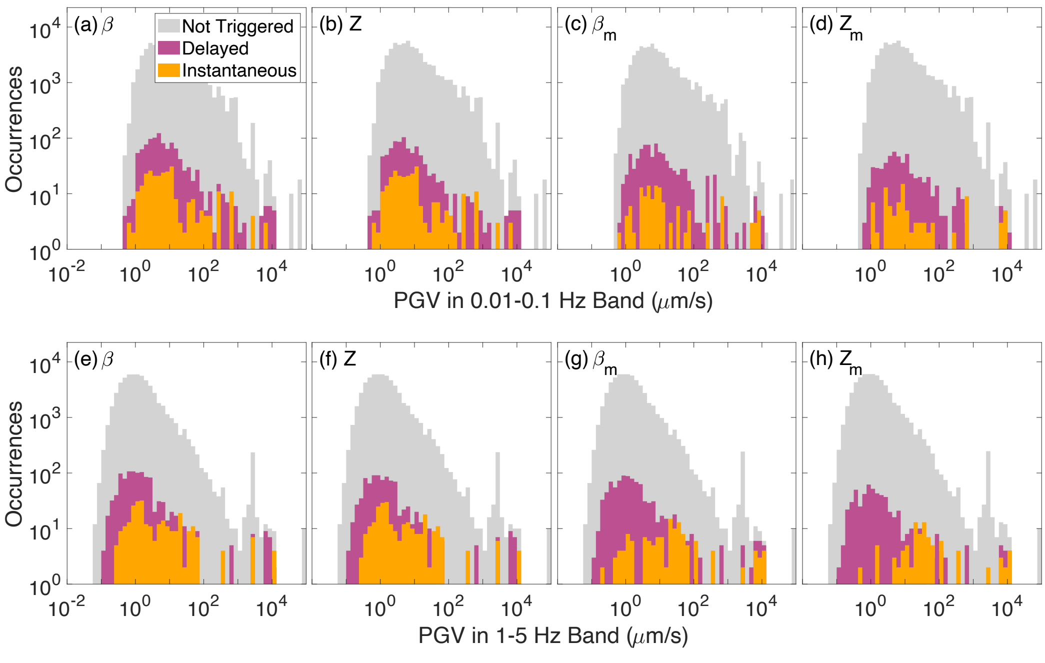

Figure 10: Distribution of PGV values in the 0.01–0.1 Hz (a–d) and 1–5 Hz (e–h) frequency bands for triggering identified by the β-statistic (a,e), Z-statistic (b,f), β_m-statistic (c,g), and Z_m-statistic (d,h). Histograms are color coded to represent the instantaneous triggering (yellow), delayed triggering (plum), and no triggering cases (gray).

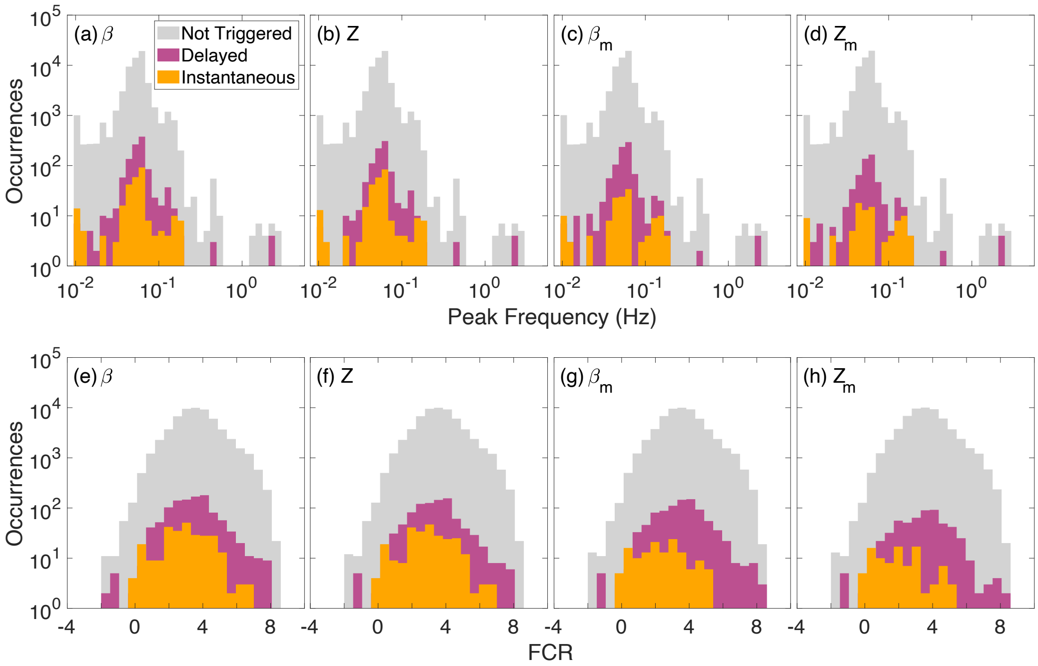

Figure 11: Distribution of peak frequency (a–d) and FCR (e–h) values for triggering identified by the β-statistic (a,e), Z-statistic (b,f), β_m-statistic (c,g), and Z_m-statistic (d,h). Histograms are color coded to represent the instantaneous triggering (yellow), delayed triggering (plum), and no triggering cases (gray).

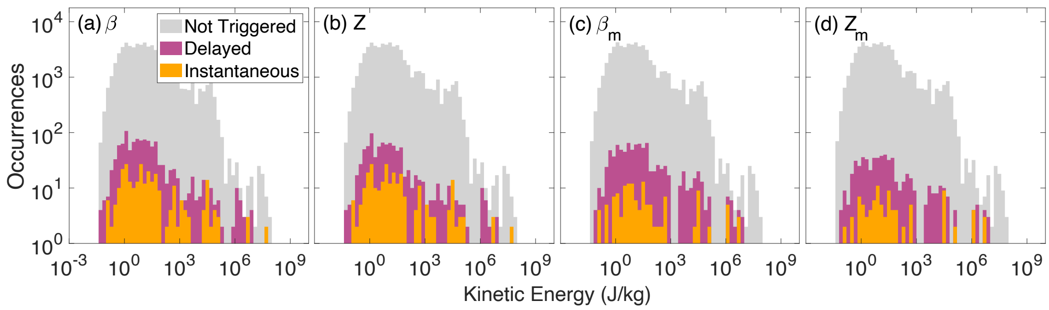

Figure 12: Distribution of kinetic energy values for triggering identified by the β-statistic (a), Z-statistic (b), β_m-statistic (c), and Z_m-statistic (d). Histograms are color coded to represent the instantaneous triggering (yellow), delayed triggering (plum), and no triggering cases (gray).

trigger earthquakes. We omitted locations that triggered less than five times from our results. Assuming each triggering case is independent and has a 5% chance of being a false positive, there is less than a 3.1×10^{-5}% probability that all triggering cases at a site are false positives if that site triggers at least five times. Our five-times selection criterion ensures that the observed spatial patterns are robust. Similarly, the temporal patterns are better resolved for sites with frequent triggering cases (Figure 9a–d), such as the San Jacinto Fault Zone, the Salton Sea Geothermal Field, and the Coso Geothermal Field. The identification of dynamic triggering could be influenced by a variety of factors, including background seismicity, magnitude of completeness, window length, af-

False Positive Rate	Poissonian Catalog	ETAS Catalog
β-statistic	0.87%	1.53%
Z-statistic	0.87%	1.46%
β_m-statistic	4.73%	2.26%
Z_m-statistic	3.35%	1.31%

Table 1: False positive rates of the statistical identification procedures when applied to a Poissonian and ETAS synthetic catalog.

tershocks of candidate events, and consecutive candidate earthquakes with short separations. To evaluate the robustness of the results, we examine the contribution of these factors item by item below. Through the suite of exercises, we confirm the robustness of our findings and outline possible biases in the results.

We generate two synthetic catalogs that do not include triggering cases to test the statistical procedures. We first generate a ten-year-long Poissonian catalog, where the occurrence of seismicity follows a Poisson distribution with magnitudes drawn from the probability distribution associated with the Gutenberg-Richter Law (Fiedler et al., 2018; Gutenberg & Richter, 1944). To construct the Poisson distribution we use an earthquake rate parameter of 0.002 earthquakes per second, equivalent to the number of earthquakes above completeness per second in the QTM catalog. We set the Gutenberg-Richter Law b-value to 0.99, an empirically obtained value for southern California (Hardebeck, 2013). Without losing generality, we assume that the seismicity occurs within the footprint of one grid point. We then randomly select 1,500 times to represent global candidate earthquakes and apply the same statistical procedures as detailed in Section 2.3 to evaluate the seismicity-rate and moment-release significance. Out of the 1,500 realizations, 0.87% of the cases are identified by both the β- and Z-statistics as anomalously high seismicity-rates, and 4.73% and 3.35% of the cases are labeled by the β_m- and Z_m-statistics as moment-release anomalies (Table 1). These cases are false positives, but the rates are less than the 5% threshold (95% confidence level) defined in our procedure.

The Poissonian catalog does not include mainshock-aftershock sequences of local earthquakes. Therefore, we design a second synthetic ten-year-long catalog following the temporal Epidemic-Type Aftershock Sequence (ETAS) model (Ogata, 1988), and the catalog is created using the procedure outlined in Shearer (2012a) and Shearer (2012b). The ETAS catalog includes both the random background seismicity and mainshock-aftershock sequences governed by the Omori-Utsu Law (Utsu, 1961). The ETAS parameters required in this formulation are aftershock productivity, b-value, and the Omori's Law time decay parameters c and p. We use an aftershock productivity of 0.003, an estimate specific to the QTM catalog from Miyazawa et al. (2021), a b-value of 0.99 (Hardebeck, 2013), a c value of 10^{-4} days, in accordance with Moutote et al. (2021) for the QTM catalog, and a p value of 1, near the global median value (Utsu et al., 1995; Zhuang et al., 2012). The earthquake magnitudes are randomly drawn from the same Gutenberg-Richter magnitude distribution used for the Poissonian catalog. Similarly, the seismicity is attributed to one grid point, and 1,500 time realizations are inspected. We find false-positive rates of 1.53% and 1.46% for the β- and Z-statistics and 2.26% and 1.31% for the β_m- and Z_m-statistics (Table 1). The false positive rates of all-four statistics are below 5% for the ETAS catalog. These tests confirm the effectiveness of the method.

We test if triggering occurrence correlates with the total number of earthquakes greater than M_c within each grid by computing the correlation coefficient (Figure 13a). The seismicity-rate anomalies identified by the β- and Z-statistics moderately correlate

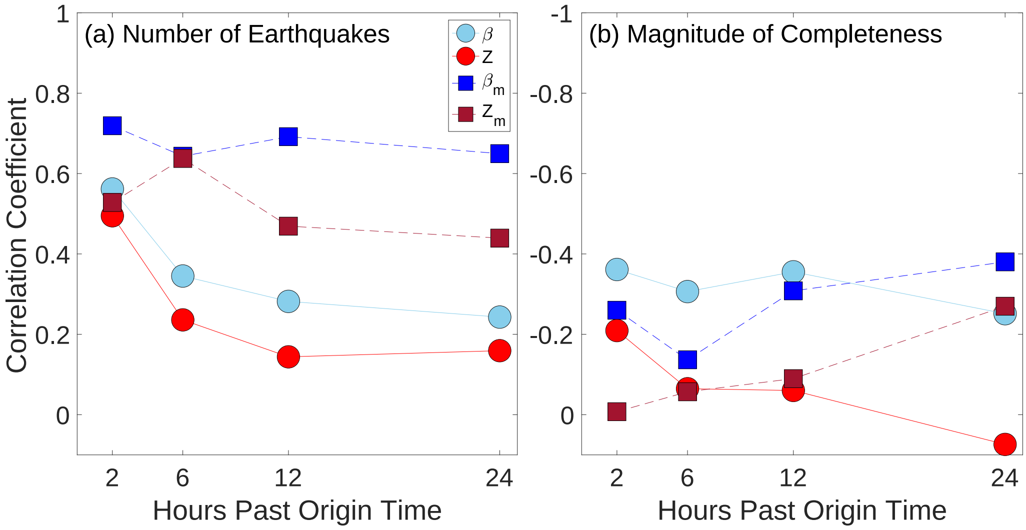

Figure 13: (a) Correlation coefficients between triggering occurrence and the number of earthquakes within the footprint of the grid points. (b) Correlation coefficients between triggering occurrence and the magnitude of completeness of earthquakes within the footprint of the grid points. Horizontal axis denotes the four time windows.

with the total earthquake number. Interestingly, the correlation coefficient is higher for instantaneous triggering than delayed cases. For example, the β-statistic has a correlation coefficient of 0.59 for the 2 hour window, but only 0.31 for the 24 hour window. A similar pattern is observed for the Z-statistic (Figure 13a). We find a strong correlation between the triggering occurrence of moment-release anomalies and the distribution of earthquake numbers. On average, the moment-release anomaly patterns identified by the β_m- and Z_m-statistics have correlation values around 0.5-0.7, differing from the seismicity-rate patterns (Figure 13a). There are some variations in the correlation values among different window lengths, i.e., correlations for the β_m-statistic vary from 0.76 at 2 hours to 0.68 at 24 hours, and correlations for Z_m-statistic oscillate in between 0.62 to 0.73 for the four window lengths. These results differ from Miyazawa et al. (2021) which found no correlation between the triggerability and seismicity-rate for a given site, but are in qualitative agreement with observations reported in van der Elst and Brodsky (2010). These correlation coefficients suggest that areas of higher background seismicity-rates are moderately more likely to experience frequent dynamic triggering.

Dynamically triggered earthquakes are generally small (Hill & Prejean, 2015), and lower magnitudes of completeness permit the identification of more triggered cases (Li et al., 2022). Therefore, the observed spatial pattern could be because the catalog has heterogeneous spatial resolutions. To determine the effect, we compute correlation coefficients between spatial patterns of the triggering occurrence and magnitude of completeness. The results are plotted in Figure 13b and show that each test statistic does not have a significant correlation with M_c since all coefficients are between -0.4 and 0.1. The seismicity anomalies identified by the β- and β_m-statistics generally have a higher negative correlation with M_c than their Z-counterparts (Figure 13b). The coefficients for the β_m- and Z_m-statistics typically decrease with time window (δ_a). For example, the coefficients range from -0.26 to -0.38 from 2 to 24 hours for the β_m-statistic, and they vary from -0.01 to -0.27 for the Z_m-statistic from 2 to 24 hours. The correlation values suggest that our identified cases are not significantly biased by the magnitude of completeness at different sites.

The overlapping δ_a windows may result in limited temporal resolutions of triggering types. For example, the 24 hour window includes seismicity from the 2 hour window, and intensely triggered seismicity in the 2 hour window could lead to an identification at a later time window, even if the triggered seismicity ceases. Such scenarios may complicate the extended cases but would not impact our identification of instantaneously triggered cases. However, identification of instantaneous cases may have been hampered by the coda of the passing seismic waves, which causes challenges in detecting and locating local microearthquakes. Furthermore, sporadic earthquakes could have been instantaneously triggered with a low seismicity-rate or low magnitudes (below M_c). These cases may have been missed by our procedure, which therefore may have underestimated the instantaneous triggering cases.

When multiple candidate earthquakes occur within 24 hours of each other and seismicity-rate and moment-release anomalies are identified at the sites of interest, it is challenging to separate the triggering contributions from the candidate earthquakes. In such cases, we consider that each of the earthquakes have contributed to cause the observed dynamic triggering, which may overestimate triggering occurrence. Specifically, M≥7 earthquakes often have M≥6 aftershocks, whose effects in dynamic triggering might be marginal. To evaluate the effect of M≥6 aftershocks in identifying dynamic triggering, we compare the results before and after removing aftershocks of the candidate trigger earthquakes. Removing potential aftershocks as candidate events may help avoid counting duplicate trigger earthquakes and underestimating the recurrence and interevent times.

For the removal procedure, we follow Knopoff et al. (1982) to define a spatial window to identify aftershocks of the candidate earthquakes. The Knopoff et al. (1982) mainshock footprint covers 100 km for an M6 event to 900 km for an M8 event. We use linear interpolation and extrapolation schemes to obtain the footprint dimension for a candidate trigger earthquake. If a smaller candidate event is within 24 hours (corresponding to the largest δ_a) of a previous event and is within its spatial area defined by Knopoff et al. (1982), the smaller earthquake is considered an aftershock of the greater candidate event, and it is excluded from the candidate trigger list. The spatial footprint from Knopoff et al. (1982) overestimates the aftershock zone and yields upper limits of the recurrence and interevent times. The percentage of candidate earthquakes that caused dynamic triggering is largely invariant to the aftershock removal procedure (Table 2). Additionally, the interevent times remain stable for the test statistics with less than one day of a difference. The aftershock removal exercise confirms the robustness of our finding and supports the conclusion that triggering is ubiquitous across southern California.

Not all large earthquakes close in time are part of the same sequence, and our procedure does not separate the triggering effects from multiple candidate earthquakes occurring within 24 hours. Multiple candidate earthquakes may increase the chances of dynamic triggering in southern California. We evaluate the hypothesis by examining the correlation between triggering occurrence and the number of candidate trigger earthquakes in the preceding 24 hours. When evaluating test statistics after each candidate earthquake, we count the number of global M≥6 earthquakes that occurred in the immediately preceding 24 hours, forming a ten-year time series. Correspondingly, we obtain a binary time series recording the triggering incidence. The correlation between the two time series has a coefficient of -0.02 for incidences identified using the β-statistic. The correlation coefficients for cases identified by other statistics (Z, β_m, and Z_m) have similar insignificant values. Therefore, we conclude that the presence of multiple candidate earthquakes within 24 hours does not impact the observed triggering patterns significantly.

4.2 Statistic Comparison

Several statistics have been introduced to measure the significance of seismicity-rate changes, e.g., the β-, Z-, and *gamma*-statistics (Habermann, 1983; Marsan & Nal-

	All candidate earthquakes	Aftershocks removed
Number of candidates	1388	1214
Percent of candidates that trigger (β)	70	68
Percent of candidates that trigger (Z)	60	60
Percent of candidates that trigger (β_m)	52	52
Percent of candidates that trigger (Z_m)	32	32
Interevent time in days (β)	3.4	4
Interevent time in days (Z)	3.9	4.5
Interevent time in days (β_m)	4.5	5.2
Interevent time in days (Z_m)	7.4	8.3

Table 2: Table of triggering results before and after removing aftershocks of candidate trigger earthquakes using the Knopoff et al. (1982) spatial footprint and a one-day temporal window.

bant, 2005; Matthews & Reasenberg, 1988). Assuming that earthquakes occur randomly, the probability distributions of the statistics can be derived analytically, and their significance threshold can be obtained through the distributions (e.g., Wyss & Marsan, 2011). The Z-statistic is often favored over the β-statistic because of its symmetric formulation (e.g., Aiken et al., 2018). However, the difference of the two statistics in identifying dynamic triggering is unclear because conventional approaches assume earthquake occurrence as a Possionian process, and a triggering threshold of 2 is widely adopted following this assumption, which is inaccurate for triggered seismicity.

To quantitatively compare the β- and Z-statistics (and the β_m- and Z_m-statistics), we compute correlation coefficients between pairs of statistics for each of the 1,388 candidate earthquakes at the sites of interest. Triggering occurrence of each statistic is recorded in a binary array, with values consisting of either a 0 (non-triggered) or 1 (triggered) for the 222 grid points. The correlation coefficient is calculated between the resulting arrays for each statistic pair. This produces one coefficient for each candidate earthquake. A higher resulting correlation coefficient shows a higher level of consistency between the two statistics while a lower coefficient shows less consistency. The correlation coefficients are computed for each time window (Figure 14). Additionally, a coefficient examining whether any triggering occurred at a grid for an earthquake is computed between statistic pairs (Figure 14). With the collection of coefficient values, we find that seismicity anomalies identified by the β- and Z-statistics are highly correlated with over half of incidences having a coefficient of 1 (Figure 14a). Similarly, moment-release anomalies identified by the β_m- and Z_m-statistics have high correlations with low variances (Figure 14d). Correlation between the seismicity-rate and moment-release anomalies are noticeably different, with smaller median coefficients and larger variances (Figure 14b,c). The results are consistent with the triggering rate results that seismicity-rate changes occur more frequently than moment-release anomalies. The results indicate that the choice of test statistic (e.g., β- or Z-statistic) is not crucial for our sampling procedure.

Although the differences in results between the β- and Z-statistics are minor, the β-statistic identifies more seismicity-rate anomalies than the Z-statistic, which is likely due to the Z-statistic being a symmetric formulation of the β-statistic (Wyss & Marsan, 2011). Both the β_m- and Z_m-statistics identify fewer moment-release anomalies than the seismicity-rate changes. However, significant moment-release anomalies are still common, with 54% and 34% triggering rates from the β_m- and Z_m-statistics. The synthetic cat-

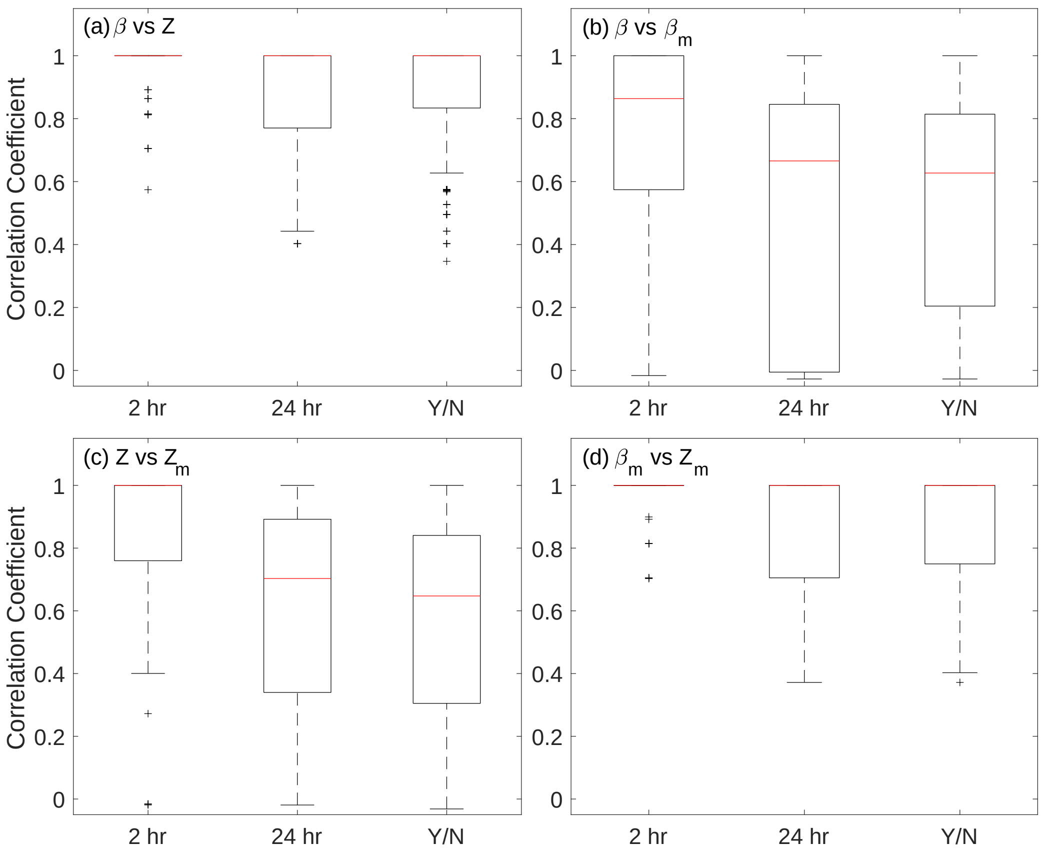

Figure 14: Boxplots of correlation coefficients between the four statistics. Here Y/N denotes if triggering was identified in any of the four time windows. Red line marks the median and the surrounding box denotes the interquartile range. Dashed lines show the range, omitting outliers. Outliers are denoted by plus-symbols, and are values greater than the third quartile plus 1.5 times the interquartile range or less than the first quartile minus 1.5 times the interquartile range.

alog tests show that the symmetric formulations, e.g., Z- and Z_m-statistics, are more accurate in comparison to their counter parts, although the differences are small.

The difference in results between the seismicity-rate and moment-release anomalies suggest that dynamically triggered seismicity in southern California is commonly observed while large earthquakes (significant moment-releases) are less frequently triggered (Figure 3.1). For example, the Salton Sea and Coso Geothermal Fields frequently experience dynamic triggering in seismicity, but do not have moment-release anomalies very often. It is likely because the thermal production areas are dominated by fragmented faults with small spatial extents (e.g., Cheng & Chen, 2018), limiting the triggered earthquake sizes. Similarly, the immature Ridgecrest fault system may contain more small fault strands (e.g., Ross, Idini, et al., 2019), which may have contributed to the triggering differences of seismicity-rate and moment-release in the region. In contrast, the San Jacinto and Elsinore faults have comparable triggering occurrence for the seismicity-rate and moment-release anomalies.

Moment-release anomalies are identified every week on average in southern California by the β_m- and Z_m-statistics. The moment-release anomalies are dominated by the largest earthquakes in the time windows. However, we note that our statistical tests cannot determine whether a specific individual earthquake was dynamically triggered. For simplicity, we convert the moment-anomalies to their equivalent moment magnitudes (Figure 15), remove duplicates from overlapping grid points and time windows, and find a nominal moment-release anomaly of M_w 3 (Figure 15). Intriguingly, the β_m- and Z_m-statistics identified 6 and 5 cases with equivalent moments above M_w 5, respectively. The cases correspond to 26% and 22% of the total M≥5 earthquakes in southern California during the study period. Except for one event likely related to the 2010 El Mayor Cucapah earthquake, each case was identified as delayed triggering with delay times beyond 6 and up to 24 hours. Close inspections of seismicity during the delay times reveal no obvious foreshock sequences for these cases. Our procedure cannot conclude whether these specific cases were dynamically triggered or not. Further, the delayed nature hinders rejecting the null hypothesis that the occurrence was random. These unusual M≥5 cases warrant detailed investigations in future follow-up studies.

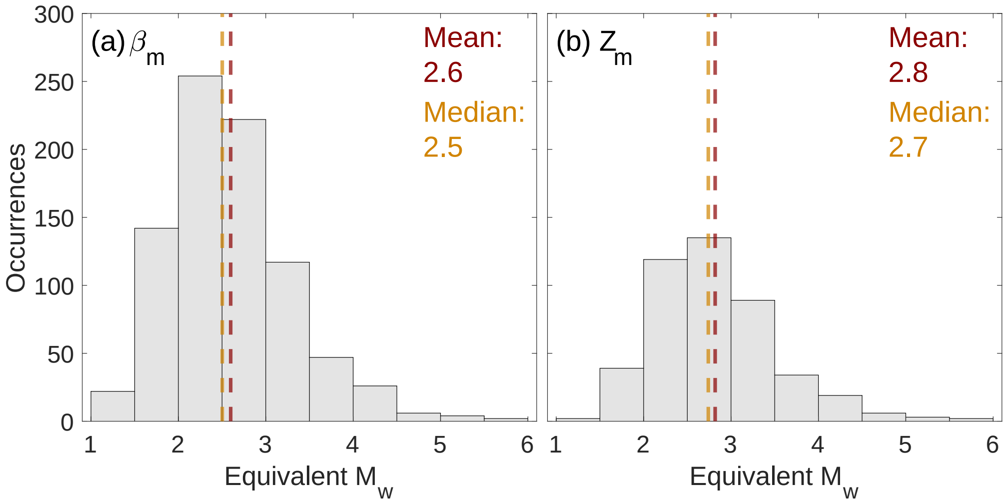

Figure 15: Distributions of equivalent moment magnitudes of the moment-release anomalies identified by the β_m- and Z_m-statistics. For extended triggering cases, the equivalent moment magnitudes are computed using the longest time window corresponding to a trigger earthquake.

4.3 Triggering Scale

To investigate the spatial footprint of the triggered seismicity and moment-release anomalies, we develop a metric of synchronization, termed the synchronization coefficient, $S_{i,j}$, between pairs of grid points:

$$S_{i,j} = \frac{N_s}{N_{tot}}, \tag{10}$$

where i and j are the indexes of two grid points, N_s is the number of shared candidate earthquakes that have caused dynamic triggering at both grids, and N_{tot} is the number of unique candidate earthquakes that have caused dynamic triggering at either or both of the grids. We define synchronization as grid points triggered by the same candidate earthquakes. $S_{i,j}$ is defined to range from 0 to 1. $S_{i,j} = 1$ denotes 100% synchronization, where dynamic triggering concurs at both grids every time the grids trigger. $S_{i,j} = 0$ indicates that dynamic triggering is not observed simultaneously at the two grids during the study period. We pairwise calculate $S_{i,j}$ for the grid points and investigate the parameter as a function of the separation distance between the ith and jth grids.

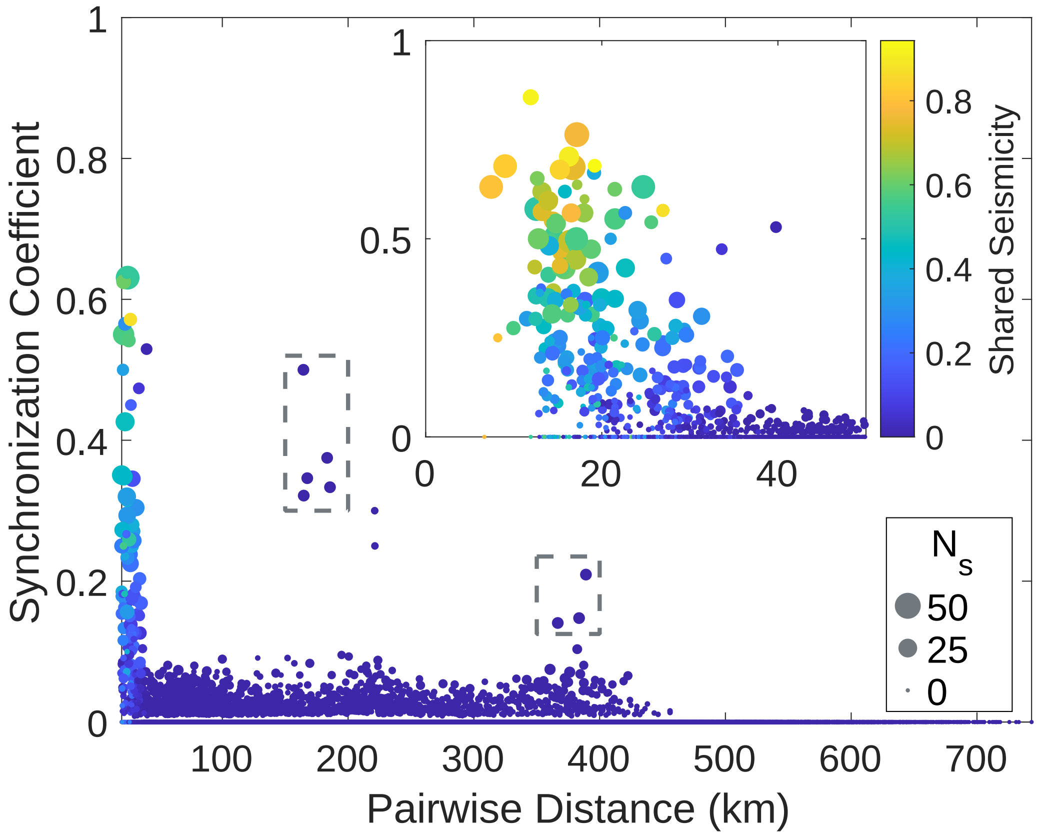

Figure 16: Synchronization coefficient versus pairwise grid distance. Inset displays a zoom-in view for grids that are less than 50 km apart. Marker color shows the proportion of local earthquakes that are shared between grid pairs during the study period. Marker size indicates the number of candidate earthquakes that cause triggering at both locations, N_s.

We hypothesize that high synchronization coefficients reflect common triggering processes occurring at the grids and the separation distance may serve as a proxy of the spatial dimension of the processes (Figure 16). For example, there is a sharp drop in $S_{i,j}$ after a distance of 40 km for seismicity-rate anomalies identified using the β-statistic. Given the gridding configuration (Section 2.2), the 40 km threshold roughly equals the distance between the centers of two grid points. Since the footprints overlap between adjacent grids, the observed high synchronization may reflect some shared seismicity. Therefore, the results suggest highly localized triggering responses of seismicity in southern California, clustering over small spatial scales, likely on the order of 40 km or smaller. We observe the same pattern for the Z-, β_m-, and Z_m-statistics.

Synchronization coefficients are generally low for grids separated beyond 40 km. However, there are two groups of outliers, denoted by the gray boxes in Figure 16, with a pairwise distance over 40 km. The first group of five pairs is around 175 km apart, and the second group is around 400 km apart. The first group associates with triggering responses from the 2015 M8.3 Illapel earthquake, Chile and its aftershocks, and the second group is due to the 2010 M8.8 Maule earthquake, Chile and its aftershocks. The two groups may suggest simultaneous triggering incidences across southern California due to the two M>8 earthquake sequences. These two groups are very rare cases as most grid pairs have low synchronization coefficients. In summary, our results suggest that triggering processes at different faults in southern California are primarily uncorrelated, and the triggering responses are highly heterogeneous. To investigate such processes, a dense network with comparable spatial scales (40 km), such as the Japanese Hi-net (Okada et al., 2004), is needed to accurately resolve the waveform characteristics within each grid.

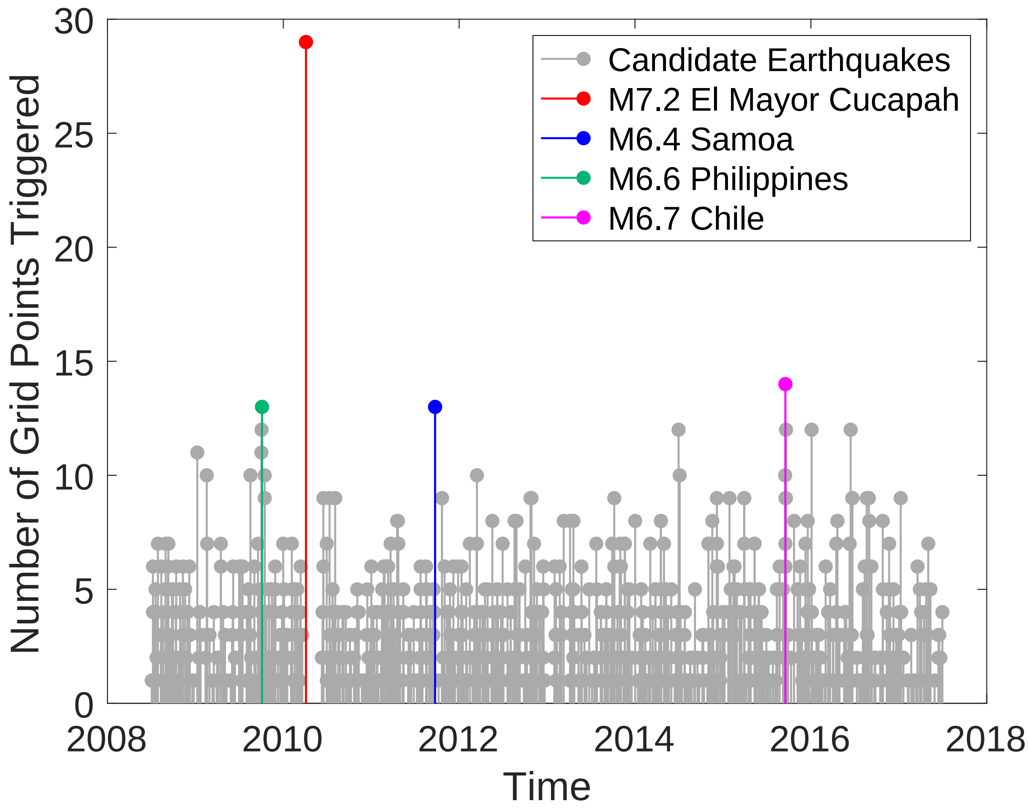

Figure 17: Time series of the number of grid points triggered after each candidate earthquake (β-statistic). Candidate earthquakes within 60 days following the 2010 El Mayor Cucapah earthquake are not analyzed (Section 2.1).

Another way to investigate the triggering scale is to count the number of triggered grids by each candidate trigger earthquake (Figure 17). We find large variability in triggering response among different candidate trigger earthquakes. For example, the 2010 El Mayor Cucapah (EMC) earthquake triggered the most seismicity-rate anomalies (β-statistic) in southern California. Seismicity was triggered at 29 grid points (Figure S6) even after excluding locations within 50 km of the epicenter. The results agree with findings in Ross, Trugman, et al. (2019) and Meng and Peng (2014). An M6.7 aftershock of the 2015 M8.3 Illapel, Chile earthquake is the second most productive trigger earthquake, causing seismicity anomalies at 14 grid points. The 2009 M6.6 Philippines earthquake and the 2011 M6.4 Samoa earthquake both correlate with seismicity-rate anomalies at 13 grid points. On average, the candidate earthquakes cause triggering at about three sites. These results further confirm that dynamic triggering occurs at local scales, and the triggering responses at different sites are usually independent. Similar plots for the other three statistics (Z, β_m, and Z_m) are included in the Supplementary Material.

4.4 Triggering Threshold

We find the triggering thresholds have large variabilities and are spatially heterogeneous (Figures 18 and 19). We examine all thresholds that are used for identifying anomalies of each statistic, and focus on discussing the the 95^{th} percentile thresholds (e.g. $\beta^a_{95\%}$) in this study as it is the most critical threshold used in our procedure. In general, the thresholds for identifying anomalies at the 95^{th} percentile are greater than 2 (e.g., $\beta^a_{95\%} \geq 2$), as reported in previous studies (Fan et al., 2021; Marsan & Nalbant, 2005). Figures 18 and 19 show that the median 95% thresholds of the four test statistics at each grid point are all above 2, suggesting that using a threshold of 2 would overestimate triggering occurrences in southern California. The San Jacinto Fault, Elsinore Fault, and Coso Geothermal Field have relatively high values of the $\beta^a_{95\%}$ and $Z^a_{95\%}$ triggering thresholds in the 2-hour window (Figure 18) while the Salton Sea Geothermal Field has a lower threshold. The spatial pattern does not seem to correlate with seismicity-rates or triggering occurrence. In contrast, the $\beta^a_{m-95\%}$ and $Z^a_{m-95\%}$ triggering thresholds in the 2-hour window have significantly less spatial variation. The thresholds for the 24-hour window have the opposite patterns, the spatial heterogeneity for $\beta^a_{95\%}$ and $Z^a_{95\%}$ is less significant in comparison to those of the 2-hour window, while there is an increase in spatial heterogeneity for the $\beta^a_{m-95\%}$ and $Z^a_{m-95\%}$ triggering thresholds. The thresholds also evolve over short time scales at each grid point. For example, Figure 20 shows the temporal evolution of the 95^{th} percentile thresholds at the Salton Sea Geothermal Field for the 2-hour window. We observe that the thresholds vary significantly with time over the nine year period, especially for the $\beta^a_{95\%}$ and $Z^a_{95\%}$ thresholds. The findings suggest that the triggering thresholds are space- and time-dependent, indicating constantly evolving faulting conditions, and our data-driven approach is effective in accounting for such variabilities and can effectively identify dynamic triggering cases.

4.5 Physical Mechanisms

A variety of physical processes may have occurred during earthquake dynamic triggering (Brodsky & Prejean, 2005; Freed, 2005; Prejean & Hill, 2018), and Coulomb failure due to the transient stress perturbation can intuitively explain the instantaneously triggered cases (Gonzalez-Huizar & Velasco, 2011; Hill, 2008; Kilb, 2003). In this case, faults are at critical states, and the dynamic stress from the seismic waves pushes the faults to slip. Assuming the faults are at a uniform critical condition, there might be a correlation between the triggering occurrence and the instantaneous waveform metrics. Our waveform analyses find no obvious correlations between triggering occurrence and the waveform metrics, including peak ground velocity and kinetic energy. The findings agree with previous searches for PGV-based triggering thresholds, where no simple thresholds have been confirmed (Freed, 2005; Hill & Prejean, 2015). Intriguingly, the instantaneously triggered seismicity and moment-release anomalies seem to require a minimum peak ground velocity above 0.2-0.5 $\mu m/s$, a unique feature compared to non-triggering and delayed triggering cases. However, such triggering cases do not always occur when the threshold is reached.

The 2010 El Mayor Cucapah earthquake has caused widespread triggering responses (Figure S6), including both static and dynamic triggering cases (Meng & Peng, 2014; Miyazawa et al., 2021; Ross, Trugman, et al., 2019). The earthquake offers an opportunity to inspect relations between the triggering occurrence and waveform metrics. We find no obvious correlations between the triggering occurrence and the PGV distribution; sites with comparably high PGV values show different triggering responses. For the El Mayor Cucapah earthquake, static triggering may have also regulated the triggering response in southern California (Meng & Peng, 2014). To further evaluate the Coulomb failure mechanism, we investigate candidate events that caused dynamic triggering at 10 or more grid points, and find no clear patterns. We also find that the earthquakes with the most widespread triggering responses have no obvious characteristic features in mag-

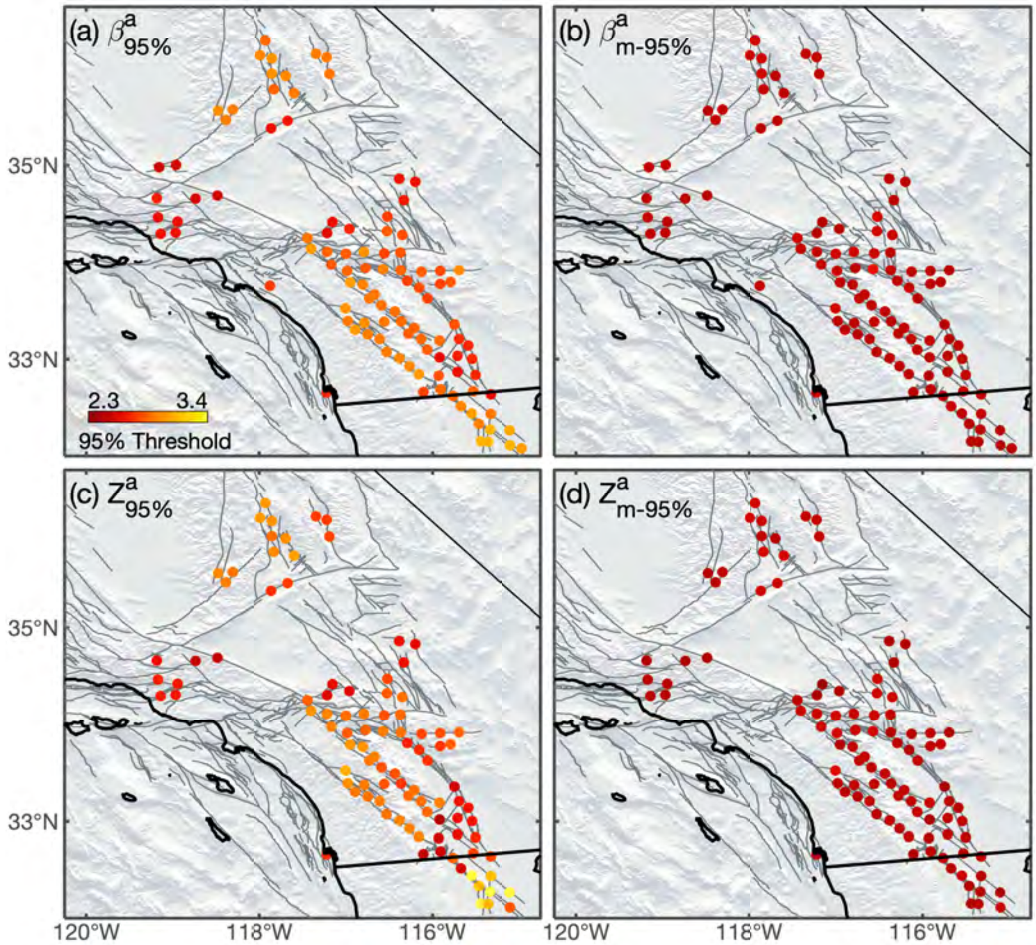

Figure 18: Spatial patterns of the median of the 95% percentile thresholds during the 2 hour time window for the β-statistic (a), β_m-statistic (b), Z-statistic (c), and Z_m-statistic (d).

nitude or location. The negative results may be due to that the faults were at different critical states, requiring different levels of stress perturbations. Additionally, the local stress field may have facilitated triggering for incoming waves from preferred azimuths (Alfaro-Diaz et al., 2020; Gonzalez-Huizar & Velasco, 2011). Alternatively, nonlinear triggering processes that were governed by rate- and state-fault properties may have regulated some of the triggering processes.

Delayed dynamic triggering requires time-dependent developments of slips and failures, which are likely controlled by non-linear mechanisms (e.g. Fan et al., 2021; Hill & Prejean, 2015; Miyazawa et al., 2021; Shelly et al., 2011). The non-linear triggering process could include a combination of mechanisms such as rate-and-state friction, material fatigue, aseismic slip, pore pressure, permeability enhancement, and granular flow among others (Brodsky & van der Elst, 2014; Hill & Prejean, 2015; Johnson & Jia, 2005; Rivera & Kanamori, 2002). Such processes may correlate better with wavefield features, including the frequency content of the passing seismic waves and the duration of intense ground motions. For example, triggering occurrence seems to relate to the PGV in low frequency bands at Long Valley (Brodsky & Prejean, 2005) and Parkfield (Guilhem et al., 2010). Our observations of delayed cases require nonlinear processes to initiate dy-

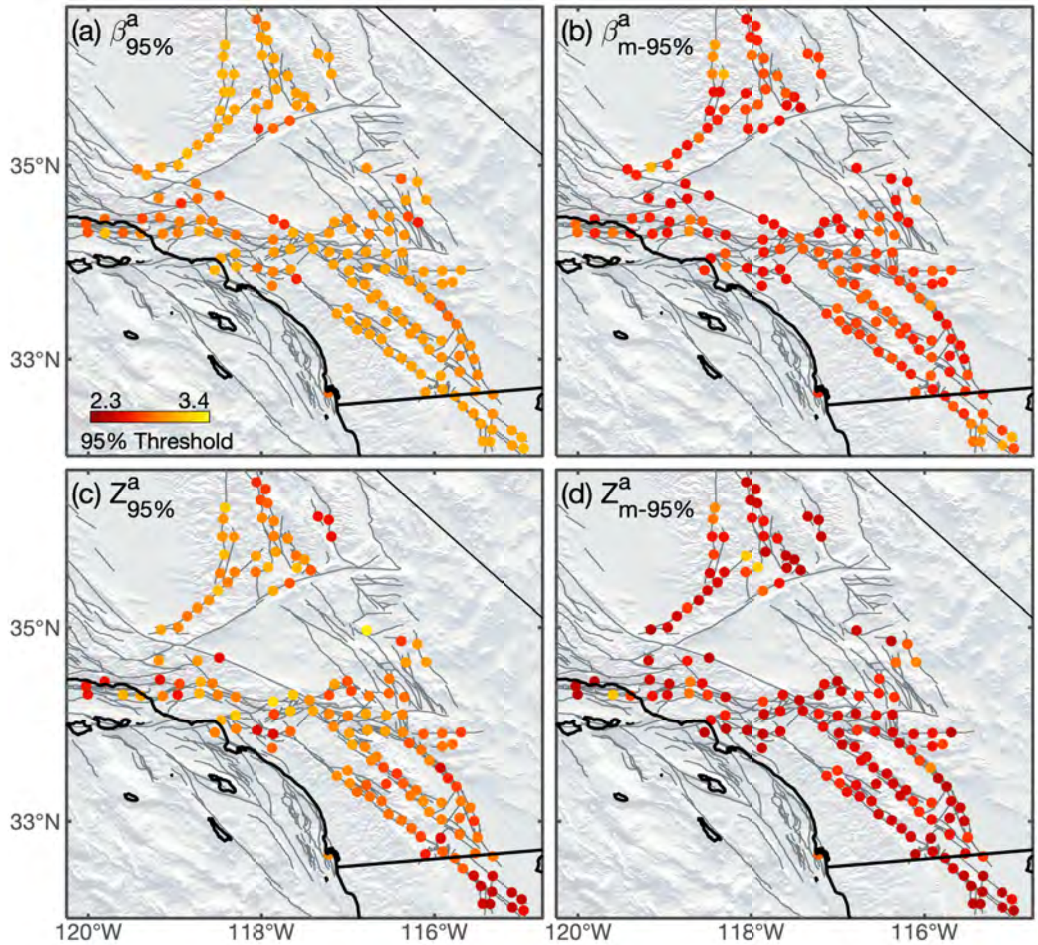

Figure 19: Spatial patterns of the median of the 95% percentile thresholds during the 24 hour time window for the β-statistic (a), β_m-statistic (b), Z-statistic (c), and Z_m-statistic (d).

namic triggering in southern California. Particularly, we find no correlation with the PGV or kinetic energy (Figures 10 and 12), nor any systematic correlations with the peak frequency or frequency content (Figure 11).

Our analyses of triggering scale show that the spatial footprint of triggering is localized and suggests that dynamic triggering is governed by conditions operating on spatial scales of tens of kilometers. Such heterogeneity may help explain the diverse triggering responses, including that Coulomb failure may be the driver for instantaneous triggering cases. Importantly, the results highlight that local conditions may play a more important role in the occurrence of triggering than features of the incoming wave, emphasizing the importance of understanding the heterogeneous stress and strength states of faults in southern California.

Models including experimentally derived rate- and state-dependent fault properties suggest that earthquake production relates to the local stress states, and the stressing episodes due to the passing seismic waves may produce clusters of earthquakes in these regions (Dieterich, 1994). We find a moderate correlation between seismicity-rate anomalies and the total number of earthquakes above completeness at each grid point (Figure 13a).

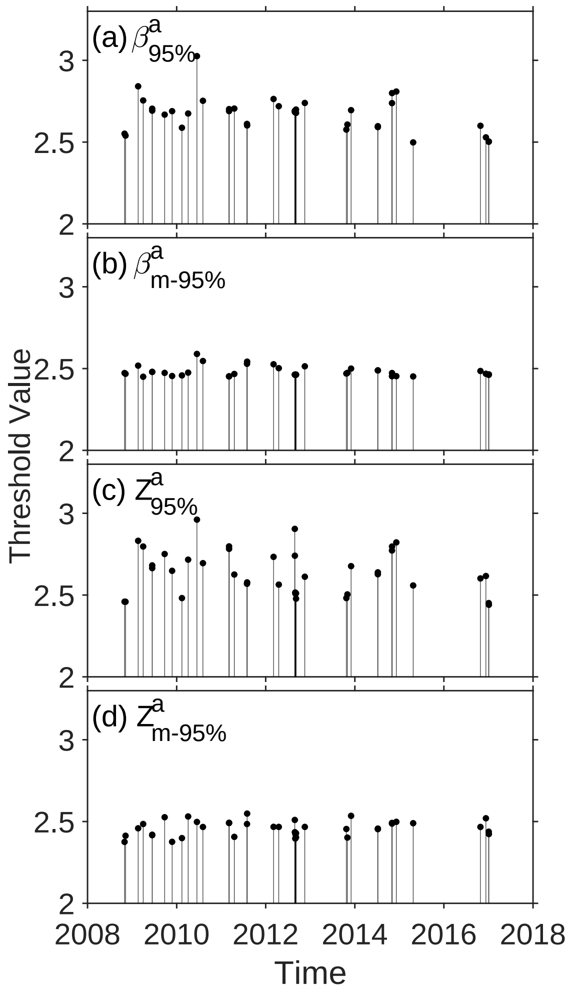

Figure 20: Temporal evolution of the 95% percentile thresholds during the 2 hour time window at a site in the Salton Sea Geothermal Field for the β-statistic (a), β_m-statistic (b), Z-statistic (c), and Z_m-statistic (d).

The correlation coefficients decrease with δ_a, which suggests that the instantaneous triggering cases are likely dominated by linear processes acting upon the heterogeneous stress field, while the delayed cases are likely caused by complex nonlinear processes. The strong correlation values observed for the moment-anomalies may have been due to the observation that more seismically active regions can generate larger earthquakes.

The clear evidence of dynamic triggering operating on local spatial scales ($\sim$40 km) suggests that the process is irrelevant to the macro-scale tectonic regimes, such as reported in Velasco et al. (2008). However, there is conflicting evidence showing that larger-scale tectonic processes can inhibit dynamic triggering (Harrington & Brodsky, 2006), suggesting directions for future comparative investigations. Qualitatively, we notice that frequent triggering occurs at the San Jacinto Fault, Salton Sea Geothermal Field, Coso Geothermal field, and the merging connection of the San Andreas and San Jacinto faults, where the fault geometries are complex (Chu et al., 2021; Marshall et al., 2022). The geometric complexities may further indicate complex stress fields at those sites (Yang & Hauksson, 2013). We experimented computing correlations between the triggering occurrence and the surface trace complexity metrics from Chu et al. (2021) but found no obvious correlation. It is possible that the surface traces do not fully reflect the 3D fault geometry and stress field complexities, and future investigations on the relations between earthquake focal mechanisms and triggering occurrence may offer new insights into the physical mechanisms of dynamic triggering processes.

5 Conclusions

We have developed an assumption-free approach to statistically identify seismicity-rate and moment-release anomalies caused by earthquake dynamic triggering. We apply the method to southern California seismicity from 2008 to 2017 and find

1. Earthquake dynamic triggering is ubiquitous throughout southern California, and up to 70% of the global M≥6 earthquakes may have caused dynamic triggering in the region.
2. Dynamic triggering was identified at most of the major faults in the area. The Salton Sea Geothermal Field, Coso Geothermal Field, and San Jacinto Fault are the most prone regions to triggering.
3. Dynamic triggering occurs every 4 days on average in southern California.
4. Individual sites in southern California are triggered less frequently, ranging from once a month to every few years.
5. Most dynamic triggering cases are delayed.
6. Significant moment-release anomalies are common in southern California, but occur less often than significant seismicity-rate increases.
7. The β-based and Z-based test statistics identify similar sets of dynamic triggering cases.
8. There are no clear connections between triggering patterns and instantaneous waveform metrics, including the peak ground velocity, peak frequency, kinetic energy, and frequency content.
9. Local fault conditions likely govern dynamic triggering occurrence.

These observations suggest that time-dependent nonlinear mechanisms acting on local scales are likely responsible for the majority of the observed triggering cases.

6 Open Research

Data Availability Statement

The earthquake catalogs used in this study are from the International Seismological Centre (ISC) catalog (International Seismological Centre, 2022) and the Southern California Earthquake Data Center (Quake Template Matching catalog; Ross, Trugman, et al., 2019). The facilities of IRIS Data Services, and specifically the IRIS Data Management Center, were used for access to the seismic waveforms and the ISC catalog, related metadata, and/or derived products used in this study. IRIS Data Services are funded through the Seismological Facilities for the Advancement of Geoscience and EarthScope (SAGE) Proposal of the National Science Foundation (NSF) under Cooperative Agreement EAR-1261681. The seismic data were downloaded using ObsPy (Beyreuther et al., 2010) and the International Federation of Digital Seismograph Networks (FDSN) web services.

Acknowledgments

We thank Peter Shearer for sharing codes to generate the ETAS synthetic catalog and useful discussion. We acknowledge support from NSF grant EAR-2022441.

References

Abercrombie, R. E., & Mori, J. (1996). Occurrence patterns of foreshocks to large earthquakes in the western united states. *Nature*, *381*(6580), 303–307. doi: 10.1038/381303a0

Aiken, C., Meng, X., & Hardebeck, J. (2018). Testing for the 'predictability'of dynamically triggered earthquakes in the geysers geothermal field. *Earth and Planetary Science Letters*, *486*, 129–140. doi: 10.1016/j.epsl.2018.01.015

Aiken, C., & Peng, Z. (2014). Dynamic triggering of microearthquakes in three geothermal/volcanic regions of California. *Journal of Geophysical Research: Solid Earth*, *119*(9), 6992–7009. doi: 10.1002/2014JB011218

Alfaro-Diaz, R., Velasco, A. A., Pankow, K. L., & Kilb, D. (2020). Optimally oriented remote triggering in the coso geothermal region. *Journal of Geophysical Research: Solid Earth*, *125*(8), e2019JB019131.

Beyreuther, M., Barsch, R., Krischer, L., Megies, T., Behr, Y., & Wassermann, J. (2010). Obspy: A python toolbox for seismology. *Seismological Research Letters*, *81*(3), 530–533. doi: 10.1785/gssrl.81.3.530

Bosl, W., & Nur, A. (2002). Aftershocks and pore fluid diffusion following the 1992 landers earthquake. *Journal of Geophysical Research: Solid Earth*, *107*(B12), ESE–17. doi: 10.1029/2001JB000155

Bowman, A. W., & Azzalini, A. (1997). *Applied Smoothing Techniques for Data Analysis: The Kernel Approach with S-Plus Illustrations* (1st edition ed.). Oxford : New York: Oxford University Press.

Brodsky, E. E., & Prejean, S. G. (2005). New constraints on mechanisms of remotely triggered seismicity at Long Valley Caldera. *Journal of Geophysical Research: Solid Earth*, *110*(B4). doi: 10.1029/2004JB003211

Brodsky, E. E., & van der Elst, N. J. (2014). The Uses of Dynamic Earthquake Triggering. *Annual Review of Earth and Planetary Sciences*, *42*(1), 317–339. doi: 10.1146/annurev-earth-060313-054648

Buurman, H., & West, M. E. (2010). *Seismic precursors to volcanic explosions during the 2006 eruption of Augustine Volcano: Chapter 2 in The 2006 eruption of Augustine Volcano, Alaska* (Tech. Rep. No. 1769-2). U.S. Geological Survey. (ISSN: 2330-7102 Publication Title: Professional Paper) doi: 10.3133/pp17692

Cattania, C., McGuire, J. J., & Collins, J. A. (2017). Dynamic triggering and earthquake swarms on east pacific rise transform faults. *Geophysical Research Letters*, *44*(2), 702–710. doi: 10.1002/2016GL070857

Cheng, Y., & Chen, X. (2018). Characteristics of seismicity inside and outside the salton sea geothermal field. *Bulletin of the Seismological Society of America*, *108*(4), 1877–1888.

Chu, S. X., Tsai, V. C., Trugman, D. T., & Hirth, G. (2021). Fault Interactions Enhance High-Frequency Earthquake Radiation. *Geophysical Research Letters*, *48*(20), e2021GL095271. doi: 10.1029/2021GL095271

Dieterich, J. (1994). A constitutive law for rate of earthquake production and its application to earthquake clustering. *Journal of Geophysical Research: Solid Earth*, *99*(B2), 2601–2618. doi: 10.1029/93JB02581

Fan, W., Barbour, A. J., Cochran, E. S., & Lin, G. (2021). Characteristics of Frequent Dynamic Triggering of Microearthquakes in Southern California. *Journal of Geophysical Research: Solid Earth*, *126*(1). doi: 10.1029/2020JB020820

Fan, W., Okuwaki, R., Barbour, A. J., Huang, Y., Lin, G., & Cochran, E. S. (2022). Fast rupture of the 2009 Mw 6.9 Canal de Ballenas earthquake in the Gulf of California dynamically triggers seismicity in California. *Geophysical Journal International*, *230*(1), 528–541. doi: 10.1093/gji/ggac059

Fiedler, B., Hainzl, S., Gert Zöller, & Holschneider, M. (2018). Detection of Gutenberg–Richter b-Value Changes in Earthquake Time Series. *Bulletin of the Seismological Society of America*, *108*(5A), 2778–2787. doi: 10.1785/0120180091

Field, E. H., Arrowsmith, R. J., Biasi, G. P., Bird, P., Dawson, T. E., Felzer, K. R., . . . Zeng, Y. (2014). Uniform California Earthquake Rupture Forecast, Version 3 (UCERF3)—The Time-Independent Model. *Bulletin of the Seismological Society of America*, *104*(3), 1122–1180. doi: 10.1785/0120130164

Freed, A. M. (2005). Earthquake Triggering by Static, Dynamic, and Postseismic Stress Transfer. *Annual Review of Earth and Planetary Sciences*, *33*(1), 335–367. doi: 10.1146/annurev.earth.33.092203.122505

Gomberg, J. (1996). Stress/strain changes and triggered seismicity following the Mw 7.3 Landers, California earthquake. *Journal of Geophysical Research: Solid Earth*, *101*(B1), 751–764. doi: 10.1029/95JB03251

Gomberg, J., & Johnson, P. (2005). Dynamic triggering of earthquakes. *Nature*, *437*(7060), 830–830. doi: 10.1038/437830a

Gomberg, J., Reasenberg, P., Bodin, P. l., & Harris, R. (2001). Earthquake triggering by seismic waves following the landers and hector mine earthquakes. *Nature*, *411*(6836), 462–466. doi: 10.1038/35078053

Gonzalez-Huizar, H., & Velasco, A. A. (2011). Dynamic triggering: Stress modeling and a case study. *Journal of Geophysical Research: Solid Earth*, *116*(B2). doi: 10.1029/2009JB007000

Guilhem, A., Peng, Z., & Nadeau, R. M. (2010). High-frequency identification of non-volcanic tremor triggered by regional earthquakes. *Geophysical Research Letters*, *37*(16). doi: 10.1029/2010GL044660

Gutenberg, B., & Richter, C. (1944). Frequency of Earthquakes in California. *Bulletin of the Seismological Society of America*, *34*, 185–188.

Habermann, R. E. (1981). Precursory seismicity patterns: stalking the mature seismic gap. *Earthquake prediction: An international review*, *4*, 29–42. doi: 10.1029/ME004p0029

Habermann, R. E. (1983). Teleseismic detection in the Aleutian Island Arc. *Journal of Geophysical Research: Solid Earth*, *88*(B6), 5056–5064. doi: 10.1029/JB088iB06p05056

Hardebeck, J. L. (2013). Appendix S—Constraining Epidemic Type Aftershock Sequence (ETAS) Parameters from the Uniform California Earthquake Rupture Forecast, Version 3 Catalog and Validating the ETAS Model for Magnitude 6.5 or Greater Earthquakes. *USGS Open File Report*.

Harrington, R. M., & Brodsky, E. E. (2006). The Absence of Remotely Triggered Seismicity in Japan. *Bulletin of the Seismological Society of America*, *96*(3), 871–878. doi: 10.1785/0120050076

Harris, R. A., & Simpson, R. W. (1992). Changes in static stress on southern california faults after the 1992 landers earthquake. *Nature*, *360*(6401), 251–254. doi: 10.1038/360251a0

Hill, D. P. (2008). Dynamic Stresses, Coulomb Failure, and Remote Triggering. *Bulletin of the Seismological Society of America*, *98*(1), 66–92. doi: 10.1785/0120070049

Hill, D. P., & Prejean, S. G. (2015). 4.11 - dynamic triggering. In G. Schubert (Ed.), *Treatise on geophysics (second edition)* (Second Edition ed., p. 273-304). Oxford: Elsevier. doi: 10.1016/B978-0-444-53802-4.00078-6

Inbal, A., Ampuero, J.-P., & Avouac, J.-P. (2017). Locally and remotely triggered aseismic slip on the central San Jacinto Fault near Anza, CA, from joint inversion of seismicity and strainmeter data. *Journal of Geophysical Research: Solid Earth*, *122*(4), 3033–3061. doi: 10.1002/2016JB013499

International Seismological Centre. (2022). On-line bulletin [Computer software manual]. Thatcham, United Kingdom. (http://www.isc.ac.uk)

Johnson, P. A., & Jia, X. (2005). Nonlinear dynamics, granular media and dynamic earthquake triggering. *Nature*, *437*(7060), 871–874.

Kilb, D. (2003). A strong correlation between induced peak dynamic Coulomb stress change from the 1992 M7.3 Landers, California, earthquake and the hypocenter of the 1999 M7.1 Hector Mine, California, earthquake. *Journal of Geophysical Research: Solid Earth*, *108*(B1), ESE 3–1–ESE 3–7. doi: 10.1029/2001JB000678

Knopoff, L., Kagan, Y. Y., & Knopoff, R. (1982). b Values for foreshocks and aftershocks in real and simulated earthquake sequences. *Bulletin of the Seismological Society of America*, *72*(5), 1663–1676. doi: 10.1785/BSSA0720051663

Li, C., Peng, Z., Yao, D., Meng, X., & Zhai, Q. (2022). Temporal changes of seismicity in salton sea geothermal field due to distant earthquakes and geothermal productions. *Geophysical Journal International*, *232*(1), 287–299. doi: 10.1093/gji/ggac324

Marsan, D., & Nalbant, S. S. (2005). Methods for Measuring Seismicity Rate Changes: A Review and a Study of How the Mw7.3 Landers Earthquake Affected the Aftershock Sequence of the Mw6.1 Joshua Tree Earthquake. *Pure and Applied Geophysics*, *162*(6), 1151–1185. doi: 10.1007/s00024-004-2665-4

Marshall, S., Plesch, A., Shaw, J., & Nicholson, C. (2022). *SCEC Community Fault Model (CFM).* Zenodo. (Type: dataset) doi: 10.5281/zenodo.5899364

Matthews, M. V., & Reasenberg, P. A. (1988). Statistical methods for investigating quiescence and other temporal seismicity patterns. *Pure and Applied Geophysics*, *126*(2), 357–372. doi: 10.1007/BF00879003

Meng, X., & Peng, Z. (2014). Seismicity rate changes in the Salton Sea Geothermal Field and the San Jacinto Fault Zone after the 2010 Mw 7.2 El Mayor-Cucapah earthquake. *Geophysical Journal International*, *197*(3), 1750–1762. doi: 10.1093/gji/ggu085

Miyazawa, M., Brodsky, E. E., & Guo, H. (2021). Dynamic Earthquake Triggering in Southern California in High Resolution: Intensity, Time Decay, and Regional Variability. *AGU Advances*, *2*(2), e2020AV000309. doi: 10.1029/2020AV000309

Moutote, L., Marsan, D., Lengliné, O., & Duputel, Z. (2021). Rare Occurrences of Non-cascading Foreshock Activity in Southern California. *Geophysical Research Letters*, *48*(7), e2020GL091757. doi: 10.1029/2020GL091757

Ogata, Y. (1988). Statistical Models for Earthquake Occurrences and Residual Analysis for Point Processes. *Journal of the American Statistical Association*, *83*(401), 9–27. doi: 10.1080/01621459.1988.10478560

Okada, Y., Kasahara, K., Hori, S., Obara, K., Sekiguchi, S., Fujiwara, H., & Yamamoto, A. (2004). Recent progress of seismic observation networks in japan—hi-net, f-net, k-net and kik-net. *Earth, Planets and Space*, *56*(8), xv–xxviii. doi: 10.1186/BF03353076

Pankow, K. L., & Kilb, D. (2020). Going Beyond Rate Changes as the Sole Indicator for Dynamic Triggering of Earthquakes. *Scientific Reports*, *10*(1), 4120. doi: 10.1038/s41598-020-60988-2

Parsons, T., & Dreger, D. S. (2000). Static-stress impact of the 1992 landers earthquake sequence on nucleation and slip at the site of the 1999 m= 7.1 hector mine earthquake, southern california. *Geophysical research letters*, *27*(13), 1949–1952. doi: 10.1029/1999GL011272

Pollitz, F. F., Stein, R. S., Sevilgen, V., & Bürgmann, R. (2012). The 11 april 2012 east indian ocean earthquake triggered large aftershocks worldwide. *Nature*, *490*(7419), 250–253. doi: 10.1038/nature11504

Prejean, S. G., & Hill, D. P. (2018). The influence of tectonic environment on dynamic earthquake triggering: A review and case study on Alaskan volcanoes. *Tectonophysics*, *745*, 293–304. doi: 10.1016/j.tecto.2018.08.007

Prejean, S. G., Hill, D. P., Brodsky, E. E., Hough, S. E., Johnston, M. J. S., Malone, S. D., … Richards-Dinger, K. B. (2004). Remotely Triggered Seismicity on the United States West Coast following the Mw 7.9 Denali Fault Earthquake. *Bulletin of the Seismological Society of America*, *94*(6B), S348–S359. doi: 10.1785/0120040610

Rivera, L., & Kanamori, H. (2002). Spatial heterogeneity of tectonic stress and friction in the crust. *Geophysical Research Letters*, *29*(6), 12–1–12–4. doi: 10.1029/2001GL013803

Ross, Z. E., Idini, B., Jia, Z., Stephenson, O. L., Zhong, M., Wang, X., ... Jung, J. (2019). Hierarchical interlocked orthogonal faulting in the 2019 Ridgecrest earthquake sequence. *Science*, *366*(6463), 346–351. (Publisher: American Association for the Advancement of Science) doi: 10.1126/science.aaz0109

Ross, Z. E., Trugman, D. T., Hauksson, E., & Shearer, P. M. (2019). Searching for hidden earthquakes in Southern California. *Science*, *364*(6442), 767–771. (Publisher: American Association for the Advancement of Science Section: Report) doi: 10.1126/science.aaw6888

Shearer, P. M. (2012a). Self-similar earthquake triggering, Båth's law, and foreshock/aftershock magnitudes: Simulations, theory, and results for southern California. *Journal of Geophysical Research: Solid Earth*, *117*(B6). doi: 10.1029/2011JB008957

Shearer, P. M. (2012b). Space-time clustering of seismicity in california and the distance dependence of earthquake triggering. *Journal of Geophysical Research: Solid Earth*, *117*(B10). doi: 10.1029/2012JB009471

Shearer, P. M., Abercrombie, R. E., & Trugman, D. T. (2022). Improved stress drop estimates for m 1.5 to 4 earthquakes in southern california from 1996 to 2019. *Journal of Geophysical Research: Solid Earth*, *127*(7), e2022JB024243. doi: 10.1029/2022JB024243

Shelly, D. R., Peng, Z., Hill, D. P., & Aiken, C. (2011). Triggered creep as a possible mechanism for delayed dynamic triggering of tremor and earthquakes. *Nature Geoscience*, *4*(6), 384–388. doi: 10.1038/ngeo1141

Silverman, B. (1986). *Density estimation for statistics and data analysis* (Vol. 26). CRC Press.

Stark, M. A., & Davis, S. D. (1996). Remotely triggered microearthquakes at the Geysers Geothermal Field, California. *Geophysical Research Letters*, *23*(9), 945–948. doi: 10.1029/96GL00011

Thomson, D. (1982). Spectrum estimation and harmonic analysis. *Proceedings of the IEEE*, *70*(9), 1055–1096. doi: 10.1109/PROC.1982.12433

Trugman, D. T., & Ross, Z. E. (2019). Pervasive foreshock activity across southern california. *Geophysical Research Letters*, *46*(15), 8772–8781. doi: 10.1029/2019GL083725

Uchide, T., Horikawa, H., Nakai, M., Matsushita, R., Shigematsu, N., Ando, R., & Imanishi, K. (2016). The 2016 kumamoto–oita earthquake sequence: aftershock seismicity gap and dynamic triggering in volcanic areas. *Earth, Planets and Space*, *68*(1), 1–10. doi: 10.1186/s40623-016-0556-4

Utsu, T. (1961). A statistical study on the occurrence of aftershocks. *Geophys.Mag.*, *30*, 521–605.

Utsu, T., Ogata, Y., S, R., & Matsu'ura. (1995). The Centenary of the Omori Formula for a Decay Law of Aftershock Activity. *Journal of Physics of the Earth*, *43*(1), 1–33. doi: 10.4294/jpe1952.43.1

van der Elst, N. J., & Brodsky, E. E. (2010). Connecting near-field and far-field earthquake triggering to dynamic strain. *Journal of Geophysical Research: Solid Earth*, *115*(B7). doi: 10.1029/2009JB006681

Velasco, A. A., Hernandez, S., Parsons, T., & Pankow, K. (2008). Global ubiquity of dynamic earthquake triggering. *Nature Geoscience*, *1*(6). doi: 10.1038/ngeo204

Wiemer, S. (2000). Minimum Magnitude of Completeness in Earthquake Catalogs: Examples from Alaska, the Western United States, and Japan. *Bulletin of the Seismological Society of America*, *90*(4), 859–869. doi: 10.1785/0119990114

Wyss, M., & Marsan, D. (2011). Seismicity rate changes. *Community Online Resource for Statistical Seismicity Analysis*. doi: 10.5078/CORSSA-25837590

Yang, W., & Hauksson, E. (2013). The tectonic crustal stress field and style of faulting along the pacific north america plate boundary in southern california. *Geophysical Journal International*, *194*(1), 100–117.

Yoshida, S. (2016). Earthquakes in Oita triggered by the 2016 M7.3 Kumamoto earthquake. *Earth, Planets and Space*, *68*(1), 176. doi: 10.1186/s40623-016-0552-8

Zhuang, J., Werner, M. J., Zhou, S., Hainzl, S., & Harte, D. (2012). Basic models of seismicity: temporal models. *Community Online Resource for Statistical Seismicity Analysis*. doi: 10.5078/CORSSA-79905851

Ubiquitous Earthquake Dynamic Triggering in Southern California

Nicolas D. DeSalvio[1], Wenyuan Fan[1]

[1]Scripps Institution of Oceanography, U.C. San Diego, La Jolla, CA, USA

Key Points:

- Earthquake dynamic triggering is ubiquitous in southern California.
- Triggered earthquakes are frequently associated with significant moment-release anomalies and are likely controlled by local processes.
- The choice of statistical test is less impactful for identifying earthquake dynamic triggering using the method developed here.

Corresponding author: Nicolas D. DeSalvio, `ndesalvio@ucsd.edu`

Abstract

Earthquakes can be dynamically triggered by the passing waves of events from disconnected faults. The frequent occurrence of dynamic triggering offers tangible hope in revealing earthquake nucleation processes. However, the physical mechanisms behind earthquake dynamic triggering have remained unclear, and contributions of competing hypotheses are challenging to isolate with individual case studies. Therefore, developing a systematic understanding of the spatiotemporal patterns of dynamic triggering can provide insights into the physical mechanisms, which may aid mitigation of earthquake hazards. Here we investigate earthquake dynamic triggering in Southern California from 2008 to 2017 using the Quake Template Matching catalog and an approach free from assuming an earthquake occurrence distribution. We develop a new set of statistics to examine the significance of seismicity-rate changes as well as moment-release changes. We show that up to 70% of global M≥6 events may have triggered earthquakes in southern California and that the triggered seismicity often occurred several hours after the passing seismic waves. On average, earthquakes are triggered about every 4 days in the region, albeit at different locations. Although adjacent fault segments can be triggered by the same earthquakes, the majority of triggered earthquakes seem to be uncorrelated, suggesting that the process is primarily governed by local conditions. Further, the occurrence of dynamic triggering does not seem to correlate with ground motion (e.g., peak ground velocity) at the triggered sites. These observations indicate that nonlinear processes may have primarily regulated the dynamic triggering cases.

Plain Language Summary

Earthquakes interact with each other, such as mainshocks triggering nearby aftershocks. Earthquake dynamic triggering is a type of interaction where seismic waves from an earthquake trigger other earthquakes beyond several fault lengths, and sometimes, up to thousands of kilometers away. Triggered earthquakes may occur upon the arrival of the seismic waves but may also be delayed hours after the wave passage, suggesting the involvement of time-dependent processes. Identifying delayed cases relies on robust measures of seismicity-rate changes. Here we present a new method that can identify triggering cases without many assumptions. We find that earthquakes in southern California are frequently triggered by distant earthquakes around the globe, and the triggered earthquakes tend to cluster in space and time. Some of the triggered earthquakes are larger in magnitude than the background seismicity. We also find that the triggering incidences do not seem to correlate with the seismic wave characteristics of the distant earthquakes. Our findings suggest that dynamically triggered earthquakes in southern California are likely caused by time-dependent, complex processes.

1 Introduction

While large earthquakes are difficult to predict on a given fault, earthquake occurrence is not completely random (e.g., Abercrombie & Mori, 1996; Ross, Idini, et al., 2019; Trugman & Ross, 2019; Utsu, 1961). Earthquakes interact with each other and often cluster in space and time, such as commonly observed mainshock-aftershock sequences. For example, the 1992 Landers earthquake caused widespread aftershocks that occurred in the near-field (Bosl & Nur, 2002; Harris & Simpson, 1992; Parsons & Dreger, 2000) and the far-field (Gomberg, 1996; Gomberg et al., 2001). The far-field aftershocks were likely triggered by the passing seismic waves, termed earthquake dynamic triggering (Aiken & Peng, 2014; Gomberg & Johnson, 2005; Gonzalez-Huizar & Velasco, 2011). As seismic waves pass through a region, transient dynamic stresses perturb local fault systems that ultimately trigger earthquakes (Hill & Prejean, 2015). This direct correlation between the triggered seismicity and passing waves reflects an observable process that promises tangible hope of deciphering earthquake nucleation mechanisms (Brodsky & van der Elst, 2014). Despite numerous observations of dynamic triggering around the globe, its occurrence conditions and associated precise physical mechanisms remain unclear (e.g., Fan et al., 2021; Meng & Peng, 2014; Velasco et al., 2008). Understanding the physical processes is crucial, as damaging earthquakes can be dynamically triggered (e.g., Pollitz et al., 2012; Uchide et al., 2016; Yoshida, 2016) but are not considered in most seismic hazard models (e.g., Field et al., 2014).

California is an ideal natural laboratory to study earthquake dynamic triggering because of its rich geophysical datasets including high quality catalogs, seismic records, and geodetic observations. The long-term continuous records provide an opportunity to examine the phenomenon by comparing statistical observations to a variety of geophysical observables (e.g., Fan et al., 2021; Miyazawa et al., 2021). Dynamic triggering has been frequently observed in California following M7 earthquakes from different regions (e.g., Aiken & Peng, 2014; Fan et al., 2022; Meng & Peng, 2014; Prejean et al., 2004). Further, geothermal and volcanic areas in the region, such as the Salton Sea Geothermal Field (e.g., Fan et al., 2021), Coso Geothermal Field (e.g., Aiken & Peng, 2014), Geysers Geothermal Field (e.g., Stark & Davis, 1996), and Long Valley Caldera (e.g., Brodsky & Prejean, 2005) seem to be particularly susceptible to dynamic triggering.

In practice, earthquake dynamic triggering is often identified using statistical methods that examine the significance of seismicity-rate changes following candidate trigger earthquakes (e.g., Marsan & Nalbant, 2005; Pankow & Kilb, 2020; Wyss & Marsan, 2011). If the changes are statistically significant, the local earthquakes are inferred to be triggered seismicity (e.g., Marsan & Nalbant, 2005; Pankow & Kilb, 2020; Wyss & Marsan, 2011). Such statistical exercises often assume that local earthquake occurrence is a random and independent process, following a Poissonian distribution (Marsan & Nalbant, 2005; Pankow & Kilb, 2020). However, this assumption is inaccurate for transient, triggered seismicity due to its correlated activity, small sample size, and short duration (e.g., Fan et al., 2021). Fan et al. (2021) experimented using a sampling method to identify statistically significant changes in seismicity-rate. Here we critically reevaluate the approach and construct new statistics that are free from the Poissonian assumption.

There are several families of statistics that have been used to evaluate seismicity-rate changes, and we focus on the two most commonly used statistics for comparison, the β-statistic (Matthews & Reasenberg, 1988) and the Z-statistic (Habermann, 1983). We further develop two additional statistics to investigate earthquake moment-release changes, the β_m-statistic and the Z_m-statistic, which can help identify anomalous occurrence of earthquakes with large magnitudes. The four test statistics were applied to southern California earthquakes to identify cases of dynamic triggering from 2008 to 2017. The statistical results are then compared with seismic waveform characteristics, including peak ground velocity (PGV), peak frequency, kinetic energy, and relative frequency content. Our approach provides a systematic way to investigate the physical mechanisms of earthquake dynamic triggering.

We find that dynamic triggering is common throughout southern California, and about 70% of global M$\geq$6 earthquakes may have triggered seismicity in the region. Significant seismic moment-release is triggered less often, but 52% of the global earthquakes may have triggered anomalies. Triggering of both types, seismicity and moment-release, is widespread in southern California, albeit with strong spatial heterogeneities in their triggering frequency. For example, earthquakes at geothermal fields and the San Jacinto Fault are frequently triggered, but triggering is rarely observed in the Los Angeles Basin. The general triggering patterns are consistent regardless of the test statistic that is used to evaluate the cases. We observe no obvious correlations between the triggering pattern and the instantaneous waveform metrics (e.g., PGV), suggesting that the transient dynamic stress is unlikely the primarily control for the observed cases. Our findings suggest that dynamic triggering in southern California likely involves nonlinear, time-dependent processes that may occur over hours to a day. Triggered seismicity clusters in space and time, indicating that the regulating physical processes likely operate on local length scales on the order of tens of kilometers.

2 Data and Methods

2.1 Catalog and Waveform Data

To study dynamic triggering in southern California, we use the Quake Template Matching catalog (QTM) with a detection threshold of 12 times the median average deviation (MAD) for local seismicity (Ross, Trugman, et al., 2019). This catalog has nearly 900 thousand earthquakes across southern California. We opt to use the 12 times MAD catalog over the 9.5 times MAD QTM version because it is more robust and is free from occasional day-long seismicity bursts that could be misinterpreted as triggering by our algorithm (e.g., Moutote et al., 2021).

We consider global M≥6 earthquakes as possible candidate trigger earthquakes, which are obtained from the International Seismological Centre (ISC) catalog (International Seismological Centre, 2022). The catalog is downloaded from the Incorporated Research Institutions for Seismology Data Management Center. We consider 1,580 M≥6 candidate trigger earthquakes between 2008 and 2017. To achieve a uniform sampling procedure, we do not examine earthquakes from January to June 2008 and July to December 2017; the details are described in Section 2.3. We also do not consider global earthquakes that occurred in the two months after the 2010 El Mayor Cucapah Earthquake due to its extended triggering behavior in southern California (e.g., Inbal et al., 2017; Meng & Peng, 2014). In total, 1,388 candidate earthquakes are investigated in this study.

To investigate local ground motions caused by the candidate trigger earthquakes, we examine the three-component, broadband, velocity seismograms recorded by stations in the region of interest, which roughly brackets southern California from 31° to 38° in latitude and from -123° to -113° in longitude. For each candidate event, we downloaded data from 10 minutes before the candidate earthquake origin time to two hours after. Thus, the data contains a 10-minute pre-event noise window and a two-hour signal window, which include body wave phases and minor arc surface wave phases. Waveform data is downloaded using the Obspy Mass Downloader tool (Beyreuther et al., 2010).

2.2 Study Area

We focus on identifying dynamic triggering in southern California where the QTM catalog continuously reported local earthquakes (Figure 1). Ideally, the region would be gridded to have uniform coverage of southern California. Such a gridding scheme would lead to about 1,750 grids using a 0.2° separation distance. In practice, we take advantage of the well-documented surface fault traces from the Southern California Earthquake Center Community Fault Model (CFM) (Marshall et al., 2022) to identify sites of interest. We first discretize the study area into 429 circular sites centering on the CFM surface traces (Figure 1a). Each site has a radius of 20 km and we space them ∼20 km apart such that each grid overlaps by ∼50% in area (inset, Figure 1a). Overlapping the grids avoids a cluster of triggered seismicity being split by a region border, leading to possible misidentification of dynamic triggering. Despite centering the grids on the CFM fault traces, our gridding strategy ensures the entire study area is nearly contained within the boundaries of the grid points. In each grid, we associate the QTM earthquakes contained within its footprint to the grid and estimate the magnitude of completeness (M_c) for the earthquakes using both the maximum-curvature and goodness-of-fit methods (Wiemer, 2000). The estimate with the greater value is taken as the M_c for the grid (Figure 1c). When evaluating dynamic triggering for the grids, we only consider earthquakes with magnitudes greater than the M_c for the individual sites. Grid points containing less than 500 earthquakes above M_c during the study period are not evaluated to ensure reliable results, leaving 222 grid points (Figure 1b-c). Our gridding approach leads to almost eight times less grid points than using an equal-separation uniform gridding scheme, which greatly improves the computational efficiency.

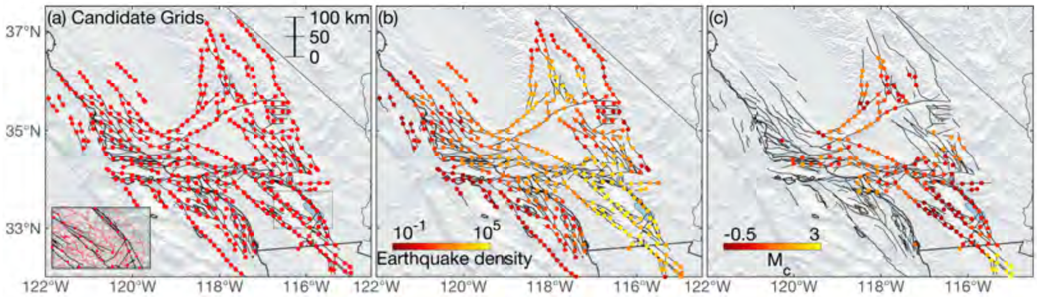

Figure 1: Study area in southern California. (a) Map of locations (grid points) where earthquake dynamic triggering is evaluated. Gray lines show surface fault traces from the Southern California Earthquake Center Community Fault Model (CFM). Each red dot represents a site of interest covering a region within a 20 km radius. Gray box shows the region highlighted in the inset demonstrating the boundaries and overlapping of the grid points near the Salton Sea area. (b) Earthquake density, representing the average number of earthquakes per year that have magnitudes above the M_c within each grid point. (c) Magnitude of completeness of the grid points. Grid points that have less than 500 earthquakes during the study period are removed.

2.3 Dynamic Triggering Identification

We hypothesize that statistically significant seismicity-rate changes within the immediate 24 hours following a candidate earthquake are likely caused by earthquake dynamic triggering. The seismicity-rate changes are examined using two different statistics: the β-statistic (Matthews & Reasenberg, 1988) and the Z-statistic (Habermann, 1983). Furthermore, we modify the two statistics to evaluate significant seismic moment-release anomalies, which we term the β_m-statistic (Section 2.3.1) and the Z_m-statistic (Section 2.3.2). The statistics compare seismicity or seismic moment within two different time periods, δ_a and δ_b, where δ_a is the time period of interest and δ_b is the reference time period. For the time period of interest (δ_a), we evaluate seismicity-rate and moment-release changes within 2-, 6-, 12-, and 24-hour time windows at each grid after the candidate earthquake origin time. The time-window length can be adjusted for customized applications. We select the 2-hour window to monitor possible instantaneous triggering and use the other three windows to characterize delayed dynamic triggering. It is worth noting that the instantaneous-triggering window length can be shorter, albeit at the cost of the robustness of the statistics due to the small number of samples. The reference time period (δ_b) is set to be the immediate 30 days before and after the candidate earthquake for the β- and β_m-statistics (a total of 60 days) and the immediate 30 days before the candidate earthquake for the Z- and Z_m-statistics. Positive statistic values suggest an increase in seismicity-rate or moment-release and the negative values suggest a decrease. Our procedure aims to identify spatiotemporal dependent thresholds to quantify the significance of the changes in seismicity and moment-release after a candidate trigger earthquake.

2.3.1 β- and β_m-statistics

The β-statistic characterizes seismicity-rate changes with respect to a reference time period that is normalized by its standard deviation (a dispersion parameter), which can be given by

$$\beta = \frac{N_a - \bar{N}_a}{\sigma_a}, \tag{1}$$

where N_a is the number of earthquakes during the time period of interest (δ_a), and $\bar{N}_a$ and σ_a are its expected value and standard deviation during the reference time period (δ_b). The expected value can be obtained analytically as $\bar{N}_a = \Lambda = N_b \cdot \frac{\delta_a}{\delta_b}$. When assuming that earthquake occurrence follows a Poisson distribution, the standard deviation is the square root of the expected value, or $\sigma_a = \sqrt{\Lambda}$. Alternatively, $\bar{N}_a$ and σ_a can be estimated empirically from the statistical population of N_a. Specifically, we randomly reposition the δ_a time window within the δ_b time window 10,000 times, leading to 10,000 samples of N_a. The population expected value and standard deviation are estimated as

$$\bar{N}_a = \frac{1}{M}\sum_{i=1}^{M} N_i, \tag{2}$$

$$\sigma_a = \sqrt{\frac{1}{M-1}\sum_{i=1}^{M}(N_i - \bar{N}_a)^2}, \tag{3}$$

where M is the number of samples (10,000 in this study) and N_i is the earthquake number in the i-th reposition time window. The obtained N_a samples are converted to their corresponding β-values (Equation 1), and we term this set of values B. The β-statistic of the original time period of interest is denoted as β_0. The procedure is similar to that outlined in Fan et al. (2021), but $\bar{N}_a$ and σ_a are obtained empirically from the sampled population and our new procedure is free from earthquake occurrence assumptions. We construct the N_a samples and their associated β-values for every candidate trigger earthquake at every grid and time window.

Typically, the β-statistic is considered 95% significant when $\beta \geq 1.96$ (Wyss & Marsan, 2011). In this case, the β-statistic attends to a zero-mean, unit-variance Gaussian distribution, which is a result of the Poissonian assumption about seismicity occurrence (Wyss & Marsan, 2011). However, the assumption may be inaccurate and the $\beta \geq 1.96$ threshold may cause erroneous identifications of significant seismicity-rate changes (e.g., Fan et al., 2021; Marsan & Nalbant, 2005; Pankow & Kilb, 2020; Prejean & Hill, 2018). Therefore, we adopt the procedure described in (Fan et al., 2021) to evaluate the statistical significance of β_0. To assess its statistical significance, we use the β-statistic values (B) to construct the B-distribution, a β-statistic probability density function (PDF, e.g., Figure 2c), by using the kernel density estimator (Bowman & Azzalini, 1997; Fan et al., 2021; Silverman, 1986). The 95^{th} percentile from the PDF accords with a 95% significance level, and the value is taken as one threshold, $\beta^a_{95\%}$, for evaluating the significance of the seismicity-rate changes. We choose the 95^{th} confidence level as suggested in Fan et al. (2021) and emphasize that the value of the parameter is chosen subjectively. One can and sometimes should use a different value, but this is dependent on the specifics of individual cases (e.g., Cattania et al., 2017; Pankow & Kilb, 2020). Additionally, we calculate β_b as the β-statistic for seismicity in a time window that has equal length of δ_a but immediately precedes the candidate event origin time. We consider the seismicity-rate change statistically significant for the given time window δ_a and grid point if $\beta_0 > \beta^a_{95\%}$ and $\beta_0 > \beta_b$ (e.g., Figure 2c). For such cases, we hypothesize that the seismicity-rate change was caused by dynamic triggering.

When computing the β-statistic for seismicity-rate changes, earthquakes with different magnitudes are treated equally as only their occurrences are evaluated. However,

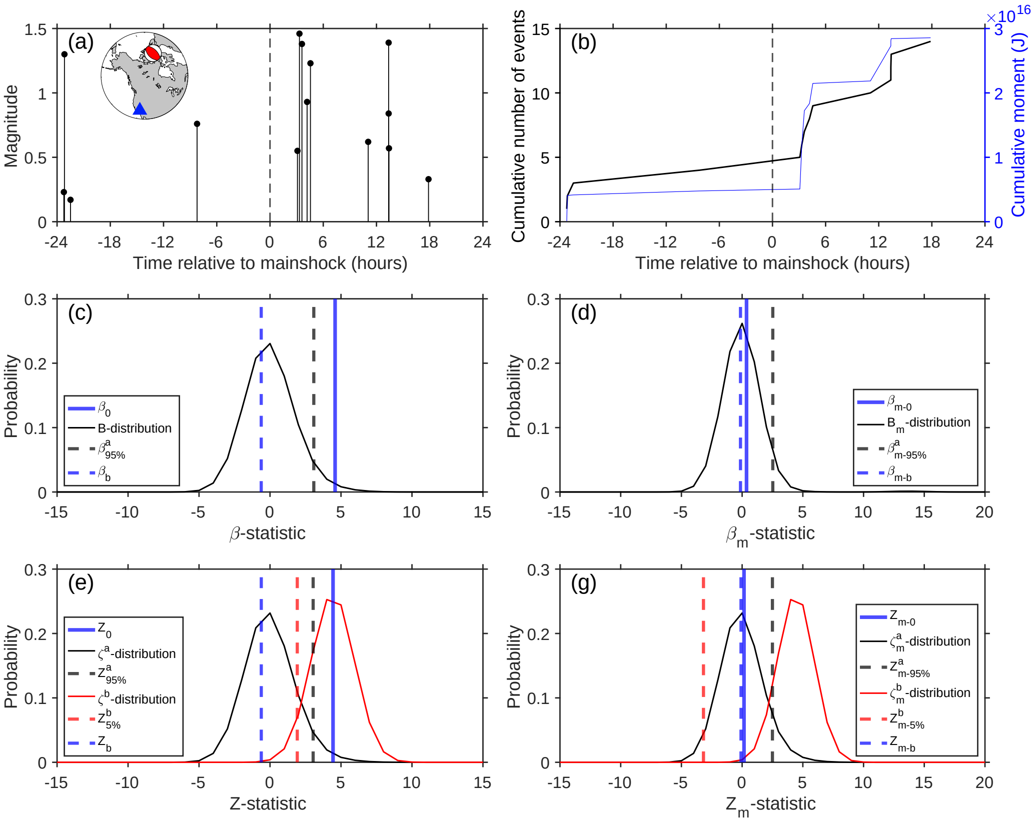

Figure 2: Example statistic distributions for δ_a as 6 hours. (a) Earthquake occurrence at a grid point footprint near the Coso Geothermal Field within 24 hours of a candidate trigger earthquake. Inset: candidate trigger earthquake (2017-01-08 23:47:13.66, M6.0, ISC ID: 611831502) and the study site. (b) Cumulative seismicity and moment-release within the grid point boundary and within 24 hours of a candidate trigger earthquake. (c) β-statistic distribution (B-distribution), β_0, and the associated thresholds β_b and $\beta^a_{95\%}$. (d) β_m-statistic distribution (B_m-distribution), β_{m-0}, and the associated thresholds β_{m-b} and $\beta^a_{m-95\%}$. (e) Z-statistic distributions (ζ^a- and ζ^b-distributions), Z_0, and the associated thresholds Z_b, $Z^a_{95\%}$, $Z^b_{5\%}$. (f) Z_m-statistic distributions (ζ^a_m- and ζ^b_m-distributions), Z_{m-0}, and the associated thresholds Z_{m-b}, $Z^a_{m-95\%}$, $Z^b_{m-5\%}$.

one magnitude difference causes about 31 times more seismic moment-release, and β-statistics based on earthquake occurrence would underestimate the impact of larger earthquakes. To detect statistically significant seismic moment-release anomalies that may have been caused by earthquake dynamic triggering, we develop a new moment-release statistic, the β_m-statistic. We sum the seismic moments of earthquakes in δ_a, denote it M_a, and compare it to the seismic moment-release in the reference time period δ_b ($\bar{M}_a$ and σ_{M_a}). For simplicity, the magnitude (m) in the QTM catalog is taken as the moment-magnitude for this calculation, and the absolute moment-release estimate is therefore likely biased (e.g., Shearer et al., 2022). However, identification of moment-release anomalies is not impacted because the statistic focuses on relative differences. The β_m-statistic is defined as:

$$\beta_m = \frac{M_a - \bar{M}_a}{\sigma_{M_a}}, \tag{4}$$

where

$$M_a = \sum_{i=1}^{N_a} 10^{1.5m_i+9.1}. \tag{5}$$

The procedure to sample the β_m-statistic population and obtain B_m is similar to that of B. We estimate the population expected value ($\bar{M_a}$) and standard deviation (σ_{M_a}) from B_m and build the B_m-distribution to identify its statistical-significance threshold, $\beta^a_{m-95\%}$ (e.g., Figure 2d). The sampling and construction procedures are similar to those outlined for the β-statistic. We then consider that the moment-release change is statistically significant for the given time window δ_a at a grid when $\beta_{m-0} > \beta^a_{m-95\%}$ and $\beta_{m-0} > \beta_{m-b}$ (e.g., Figure 2d).

2.3.2 Z- and Z_m-statistics

Similar to the β-statistic, the Z-statistic can also measure the degree of seismicity-rate changes in comparison to the background seismicity-rate (Habermann, 1981, 1983). In this study, we examine the Z-statistic and compare the results with the β-statistics for the same earthquakes. The Z-statistic is a symmetric measure of the seismicity-rate changes because its normalization depends on seismicity in both the time period of interest and reference period (Wyss & Marsan, 2011). Following Habermann (1983), we compute the Z-statistic as

$$Z = \frac{{}^{N_a}\!/\!_{\delta_a} - {}^{N_b}\!/\!_{\delta_b}}{\sqrt{\left({}^{\sigma_a}\!/\!_{\delta_a}\right)^2 + \left({}^{\sigma_b}\!/\!_{\delta_b}\right)^2}}, \tag{6}$$

where N_b is the number of earthquakes within δ_b, σ_b is the standard deviation associated with the distribution of N_b, and N_a, δ_a, δ_b, and σ_a are defined as above. The quantities N_a/δ_a and N_b/δ_b represent the mean seismicity-rates during their respective time periods. The Z-statistic is free from seismicity occurrence assumptions if σ_a and σ_b are estimated empirically. Similar to the β-statistic sampling procedure, we sample the N_b population by randomly repositioning the δ_b window 10,000 times within one year of the candidate trigger earthquake, ranging from 6 months before to 6 months after the event origin time. We estimate the population statistics for the N_b population, particularly the expected value and standard deviation (σ_b), which are then used to compute a Z-statistic for the candidate trigger earthquake at a given grid point. We note that the sampling procedure implicitly assumes that σ_a and σ_b are invariant throughout their respective sampling time periods, which is 30 days for σ_a and one year for σ_b.

Similar to the β-statistic, the Z-statistic also attends to a zero-mean, unit-variance Gaussian distribution when the earthquake occurrence follows a Poisson distribution. In such a case, the seismicity-rate increase is statistically significant at the 95% confidence level when $Z \geq 1.96$ (Aiken et al., 2018; Wyss & Marsan, 2011). In our approach, we require the Z-statistic exceed $Z^a_{95\%}$, Z_b, and $Z^b_{5\%}$ (e.g., Figure 2e). The $Z^a_{95\%}$ threshold is the 95^{th} percentile of a Z-statistic distribution (ζ^a-distribution) constructed by randomly sampling N_i for a window length of δ_a within 30 days before and after the candidate trigger earthquake origin time. We hold N_b constant as the seismicity in the 30 days before the candidate trigger earthquake. The Z_b threshold is for seismicity in a time window that has equal length of δ_a but immediately precedes the candidate event origin time. The $Z^b_{5\%}$ is the 5^{th} percentile obtained from a Z-statistic distribution (ζ^b-distribution) constructed by sampling N_i for a window length of δ_b within 6 months before and after the candidate trigger earthquake origin time. We keep N_a constant as the seismicity within the δ_a window after the origin time.

Similar to the β_m-statistic, we design the Z_m-statistic to detect seismic moment-release anomalies. The Z_m-statistic is given by:

$$Z_m = \frac{M_a/\delta_a - M_b/\delta_b}{\sqrt{\left(\sigma_{M_a}/\delta_a\right)^2 + \left(\sigma_{M_b}/\delta_b\right)^2}}, \tag{7}$$

where M_b follows Equation 5 but for the δ_b time period. The sampling procedure for the Z_m-statistic is similar to that of the Z-statistic (e.g., Figure 2g), and we define a similar set of thresholds to evaluate the statistical significance of the moment-release anomalies, including, $Z_{m-0} > Z^a_{m-95\%}$, $Z_{m-0} > Z_{m-b}$, and $Z_{m-0} > Z^b_{m-5\%}$ (e.g., Figure 2g).

Taking the January 8, 2017 M6 Queen Charlotte earthquake as an example trigger earthquake (Figure 2a), we find that the earthquake may have triggered seismicity within the Coso Geothermal Field within 6 hours of its origin time (Figure 2 and Table S1), which is indicated by both the β-statistic and Z-statistic. However, neither the β_m- or Z_m-statistic suggests anomalous moment-release change at the location during the 6-hour time window.

2.4 Waveform Metrics

We inspect the velocity waveforms of the candidate trigger earthquakes in southern California and measure four instantaneous waveform metrics: peak ground velocity, peak frequency, kinetic energy, and relative frequency content. We measure the peak ground velocity (PGV) in two frequency bands, 0.01–0.1 Hz and 1–5 Hz (Figure 3a-b). After downloading the records, we first remove the instrument response and decimate the data to a 20 Hz sampling rate. Then we band-pass filter the data and compute their envelope functions. The maximum envelope amplitudes are measured in both the pre-event noise window (10 minutes) and the signal window (2 hours) independently for all three channels at each station. A signal-to-noise ratio (SNR) is computed as the ratio between the maximum amplitudes of the signal and noise windows for each channel. We only use traces that have a SNR greater than 5 for both the low- and high-frequency bands to measure the waveform metrics. If all three channels at a station have a SNR greater than the threshold, we take the geometric mean of the qualified waveform envelopes and calculate a single PGV value for the station. We use the same qualified traces for the other calculated metrics and discard the rest. Figure 3a-b demonstrates an example of measuring the PGV values of the 2017 M6 earthquake in the Queen Charlotte Islands, Canada at CI.JRC2 (near Coso) in the two frequency bands. The 0.1 to 1 Hz frequency band is not investigated here as the noise level is high due to microseisms.

We measure the peak frequency of qualified ground velocity records at each station caused by the candidate trigger earthquakes (e.g., Figure 3c). For an earthquake-station pair, we estimate the power spectrum of the waveform in the signal window for each channel using the multitaper method with 11 Slepian tapers (Thomson, 1982). Given the earthquake-station distance, we focus on the 0.01–5 Hz frequency band and compute the geometric mean of the power spectra from the three channels. The corresponding frequency of the maximum power is taken as the peak frequency.

For the kinetic energy calculation, the qualified seismic data are first band-pass filtered at 0.01 to 10 Hz (Figure 3d), and the root-mean-square (RMS) values are computed for each channel in the signal window. This leads to three measurements in total for each station. We then record the RMS-square-sum of the signal window as the kinetic energy per unit mass for the earthquake-station pair. Figure 3d shows an example of measuring the kinetic energy for the M6 Queen Charlotte earthquake at CI.JRC2.

Lastly, we examine the relative frequency content of the passing waveforms. We modify the Frequency Index (FI) metric (Buurman & West, 2010) given by:

$$\mathrm{FI} = \log_{10}\left(\frac{\bar{A}_u}{\bar{A}_l}\right), \tag{8}$$

where $\bar{A}_l$ is the mean power spectrum amplitude in a lower frequency band and $\bar{A}_u$ in an upper frequency band. We replace the mean spectral amplitudes with the integrated total power within each frequency band, which is a more stable calculation. We refer to this as the Frequency Content Ratio (FCR):

$$\mathrm{FCR} = \log_{10}\left(\frac{\int_{f_{l1}}^{f_{l2}} S(f)\, df}{\int_{f_{u1}}^{f_{u2}} S(f)\, df}\right) = \log_{10}\left(\frac{P_l}{P_u}\right) \tag{9}$$

where $S(f)$ is the geometric mean of the power spectra of the three channels and f_{l1}, f_{l2}, f_{u1}, f_{u2} define the lower and upper frequency bands. Here the lower frequency band is taken as 0.01–1 Hz, and the upper frequency band is 1–5 Hz (Figure 3c). We place the lower band in the numerator to ensure that the FCR estimates are primarily positive for teleseismic earthquakes, due to their more prominent low frequency signals.

The waveform metrics are computed for each station independently, and the measurements for each candidate trigger earthquake are interpolated to nearby grid points. For each grid point, we obtain the median of the waveform metrics at the five nearest stations within 100 km (Figure 4). We do not make measurements at grid points when less than three stations are available.

3 Results

In this section, we detail our observations of seismicity and moment-release anomalies in southern California associated with the candidate earthquakes, focusing on their spatial (Section 3.1) and temporal (Section 3.2) patterns. Since the seismicity-rate anomalies are identified at a 95% confidence level, we omit grid points that triggered less than 5 times from our results and discussion (see Section 4.1 for details). In general, we find that up to 70% of candidate trigger earthquakes caused dynamic triggering in southern California from 2007 to 2017. We find that triggering occurrence varies from fault to fault, and triggering occurs most often at the Salton Sea and Coso geothermal fields as well as the San Jacinto Fault. Furthermore, we identify temporal patterns evolving at multiple scales, from instantaneous to delayed responses, and from intermittent occurrence at a given site to frequent triggering in southern California. Lastly, we examine the waveform metrics of candidate trigger earthquakes at sites with both normal and anomalous seismicity and moment-release rate changes.

3.1 Spatial Triggering Patterns

Dynamic triggering likely occurs frequently in southern California. About 70% of the candidate trigger earthquakes associate with seismicity anomalies that are identified using the β-statistic (Figure 5). Given the close temporal correlation, we consider that the anomalies are dynamically triggered by the earthquakes. Spatially, seismicity at 54% of the grid points (a total of 222 points) was triggered at least five times. Using the Z-statistic, we find that 60% of candidate earthquakes associate with seismicity anomalies, and seismicity at 42% of the grid points was likely dynamically triggered five or more times. Anomalous seismic moment-release is less commonly observed to associate with the candidate earthquakes, with the β_m- and Z_m-statistics identifying triggered seismicity after 52% and 32% of the candidate earthquakes, respectively. Spatially,

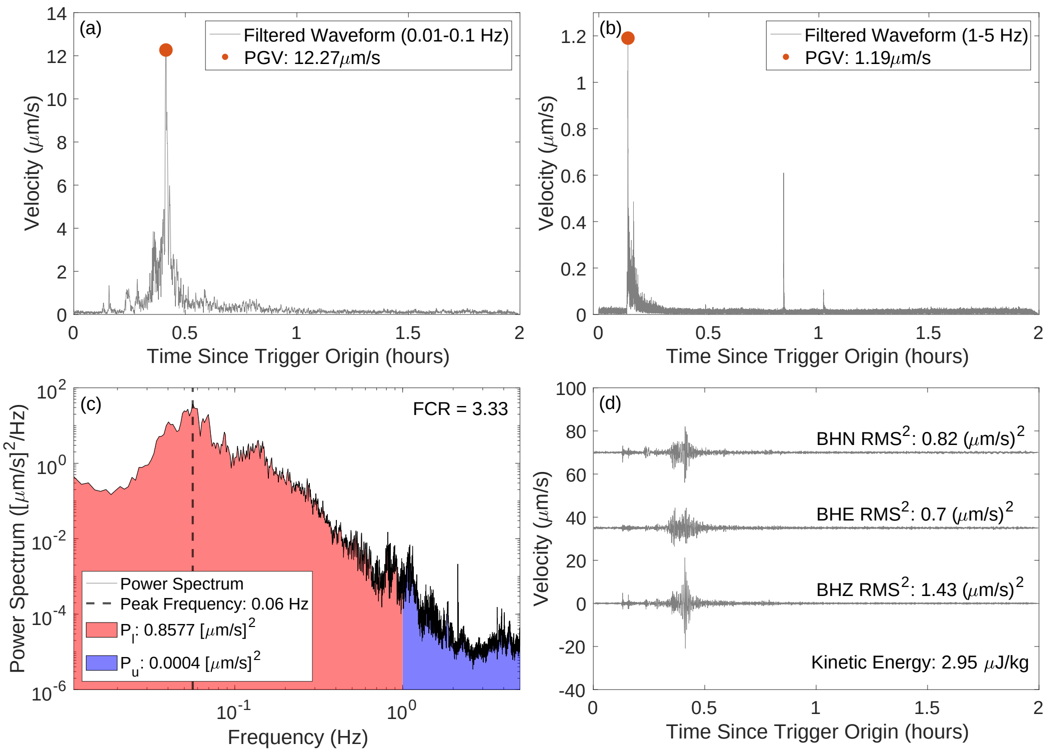

Figure 3: Waveform metric calculations of the January 8, 2017 M6 Queen Charlotte earthquake at station CI.JRC2, near the Coso Geothermal Field. (a–b) Waveform envelopes (geometric mean of the three-component envelopes) at the 0.01–0.1 Hz and 1–5 Hz frequency bands. The maximum amplitudes of the envelopes are taken as the PGV of the frequency bands, respectively. (c) Geometric mean of the three-component power spectra. Peak frequency corresponds to the frequency yielding the maximum value of the spectrum. FCR is calculated using the integral results P_l in the 0.01–1 Hz band and P_h in the 1–5 Hz band (Equation 9). (d) Band-pass filtered waveforms. Square sum of the three-component RMS values is taken as the kinetic energy per unit mass. The BHE data is shifted 35 $\mu m/s$ upwards, and BHN 70 $\mu m/s$.

moment-release anomalies are identified at 45% and 33% of grid points using the β_m- and Z_m-statistics, respectively.

Spatial patterns of triggering occurrence for the four test statistics are highly heterogeneous (Figure 5). Here triggering occurrence counts the number of candidate trigger earthquakes that caused seismicity or moment-release anomalies in any of the four time windows (δ_a as 2, 6, 12, or 24 hours) during the study period. The Salton Sea Geothermal Field (SSGF), Coso Geothermal Field (CGF), and San Jacinto Fault (SJF) most frequently experienced seismicity-rate anomalies identified by the β- and Z-statistics, which are likely caused by the passing waves (Figure 5a,c). Seismicity at the Elsinore Fault, the merging connection of the San Andreas and San Jacinto Faults, the southern San Andreas, the southern Sierra Nevada, and the Ridgecrest region is frequently triggered by remote earthquakes. In contrast, moment-release anomalies that are identified by the β_m- and Z_m-statistics have different spatial patterns than those of the seismicity-rate anomalies (Figure 5b,d). Specifically, the SSGF and CGF are less likely to have moment-

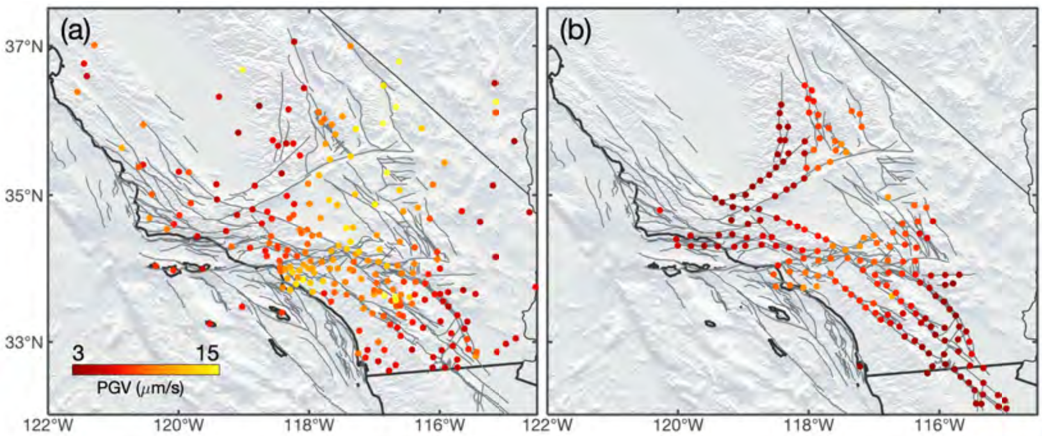

Figure 4: Example interpolation of PGV values in the 0.01-0.1 Hz band for the January 8, 2017 M6 Queen Charlotte earthquake. (a) Measured values at each station. (b) Interpolated values for qualified grid points.

release anomalies than SJF, and their triggering occurrence is comparable to that of the Elsinore Fault (Figure 5b,d). Moment-release anomalies are less frequently observed at the merging connection of the San Andreas and San Jacinto Faults, Ridgecrest area, and southern San Andreas fault (Figure 5b,d).

We observe more delayed (6 to 24 hour windows, Figures S1, S2 and 7) than instantaneous triggering cases (2 hour, Figure 6). Such triggering occurrence differences between the instantaneous and delayed cases are observed for all four statistics. While instantaneous triggering cases are often difficult to observe because the catalog completeness may suffer due to the passing wave coda, our results show that delayed dynamic triggering of both seismicity and moment-release occurs frequently in southern California at multiple sites. For example, 83% of the β-statistic seismicity-rate anomalies are delayed cases, and 79% of the Z-statistic cases are delayed, showing strong agreement. Further, 91% and 89% of moment-release anomalies are delayed cases from the β_m- and Z_m-statistics, respectively. Around half of instantaneously triggered cases of seismicity also extended into later hours. Specifically, 51% and 46% of the instantaneous cases, as identified by the β- and Z-statistics, had extended responses reaching up to and beyond the 6-hour window. Intriguingly, more than half of the instantaneously triggered moment-release extended into later hours, with 63% and 59% of cases for the β_m- and Z_m-statistics, respectively.

Our triggering occurrence patterns are similar to the triggerability pattern in Miyazawa et al. (2021) with some differences at the Beta Offshore Platform, San Andreas Fault, and the southern Sierra. Miyazawa et al. (2021) investigates dynamic triggering occurrence in southern California using the same QTM catalog. Differently, Miyazawa et al. (2021) adapts the method in van der Elst and Brodsky (2010) and inverts for triggerability based on distributions of separation times between the candidate earthquake and the local earthquakes immediately preceding and succeeding the candidate. The discrepancies at a few sites in our results are likely because we examine seismicity in the entire time window and not just the temporally closest events. Our study corroborates the findings of Velasco et al. (2008), which finds that triggering is ubiquitous around the globe and independent of tectonic environment. Velasco et al. (2008) reports a triggering rate of 80% for M≥7 candidates.

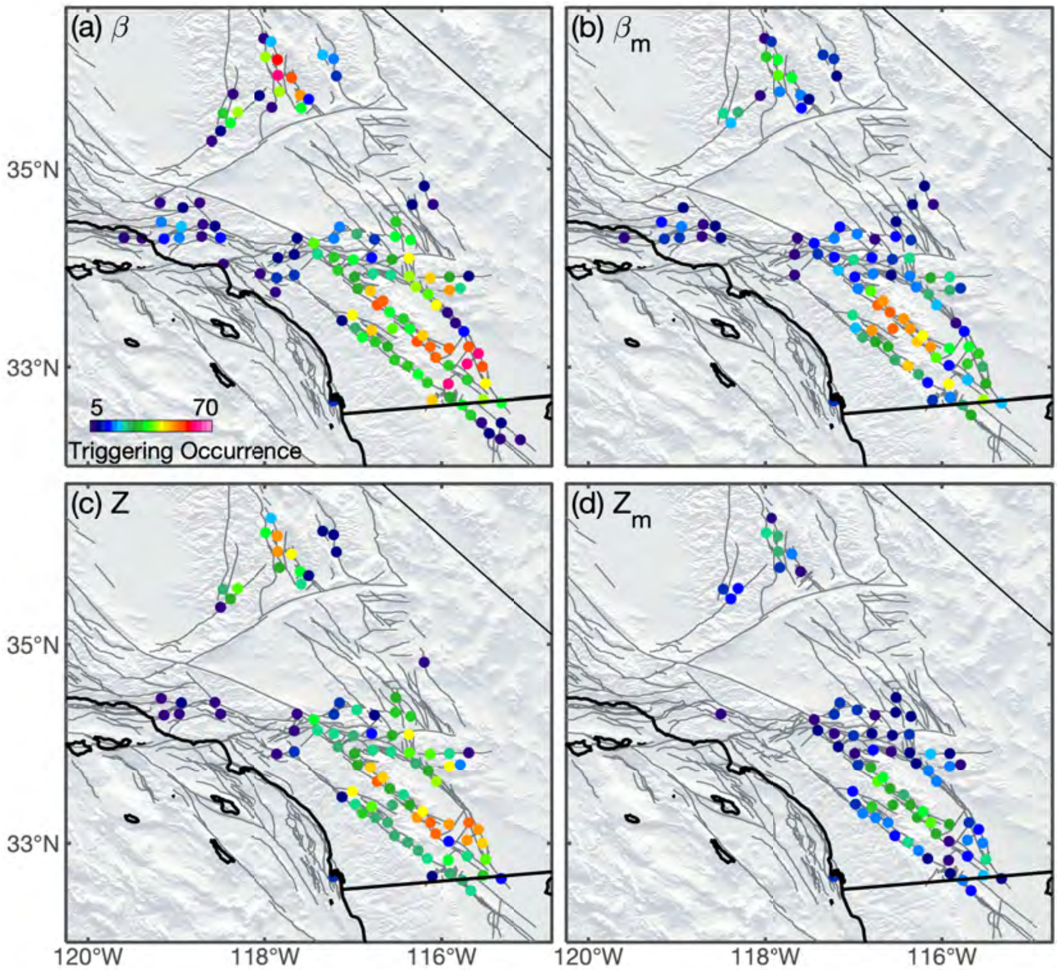

Figure 5: Spatial triggering patterns in southern California. Triggering occurrence identified using the β-statistic (a), β_m-statistic (b), Z-statistic (c), and Z_m-statistic (d) are denoted in color. Triggering occurrence is the number of candidate trigger earthquakes that caused seismicity or moment-release anomalies in any of the four time windows.

3.2 Temporal Triggering Patterns

To investigate the temporal evolution of dynamic triggering processes, we inspect time intervals between consecutive triggering incidences at every grid point, denoted as local recurrence times. We also investigate consecutive time intervals of dynamic triggering cases in southern California for any grid point, which we term interevent time.

Dynamic triggering occurs at individual grid points intermittently, often on the timescale of months to years (e.g., Figure 8). The spatial pattern of recurrence times correlates with that of triggering occurrence and there are strong heterogeneities from site to site (Figures 5 and 8). The median recurrence times range from tens of days to years for different sites, and adjacent sites tend to have similar recurrence times. For example, the Salton Sea Geothermal Field, Coso Geothermal Field, and San Jacinto Fault have frequent incidences of seismicity-rate anomalies, with average recurrence times around 2–2.5 months (Figure 8). In contrast, we rarely observe seismicity-rate anomalies in the LA Basin, showing gaps on the order of years between triggering cases (Figure 8). Similar to the spatial pattern of moment-release anomalies (Figure 5), the geothermal fields

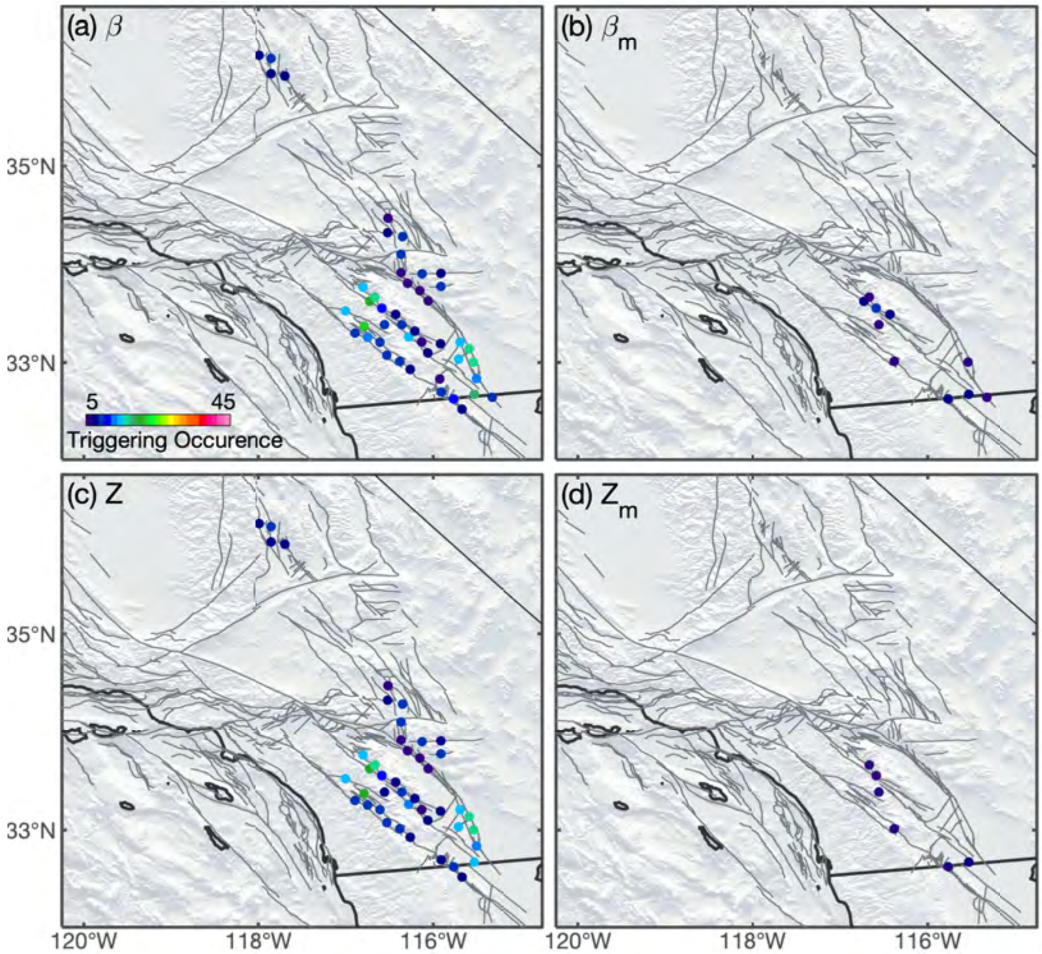

Figure 6: Triggering occurrence during the 2 hour (δ_a=2) time window using the β-statistic (a), β_m-statistic (b), Z-statistic (c), and Z_m-statistic (d).

do not have significant moment-release anomalies very often (Figure 8). For example, Figure 9a–d shows the distributions of recurrence times for a few notable locations using the β-statistic. Similar figures of other statistics are included in the Supplementary Material.

On average, dynamically triggered seismicity is identified using the β- and Z-statistics at one or more of the grids in southern California every 3.4 and 3.9 days, respectively. Similarly, moment-release anomalies from the β_m and Z_m-statistics occur every 4.5 and 7.4 days on average in the region, respectively. The distributions of interevent times in southern California are summarized in Figure 9e–h, showing that dynamic triggering occurs frequently in southern California on a scale of every few days. We also explored temporal variations of the recurrence and interevent times in the region during the study period, e.g., whether the triggering patterns evolve with the occurrence of the 2010 El Mayor Cucapah earthquake and the 2019 Ridgecrest earthquakes. We do not identify significant variations over the triggering patterns using the QTM catalog.

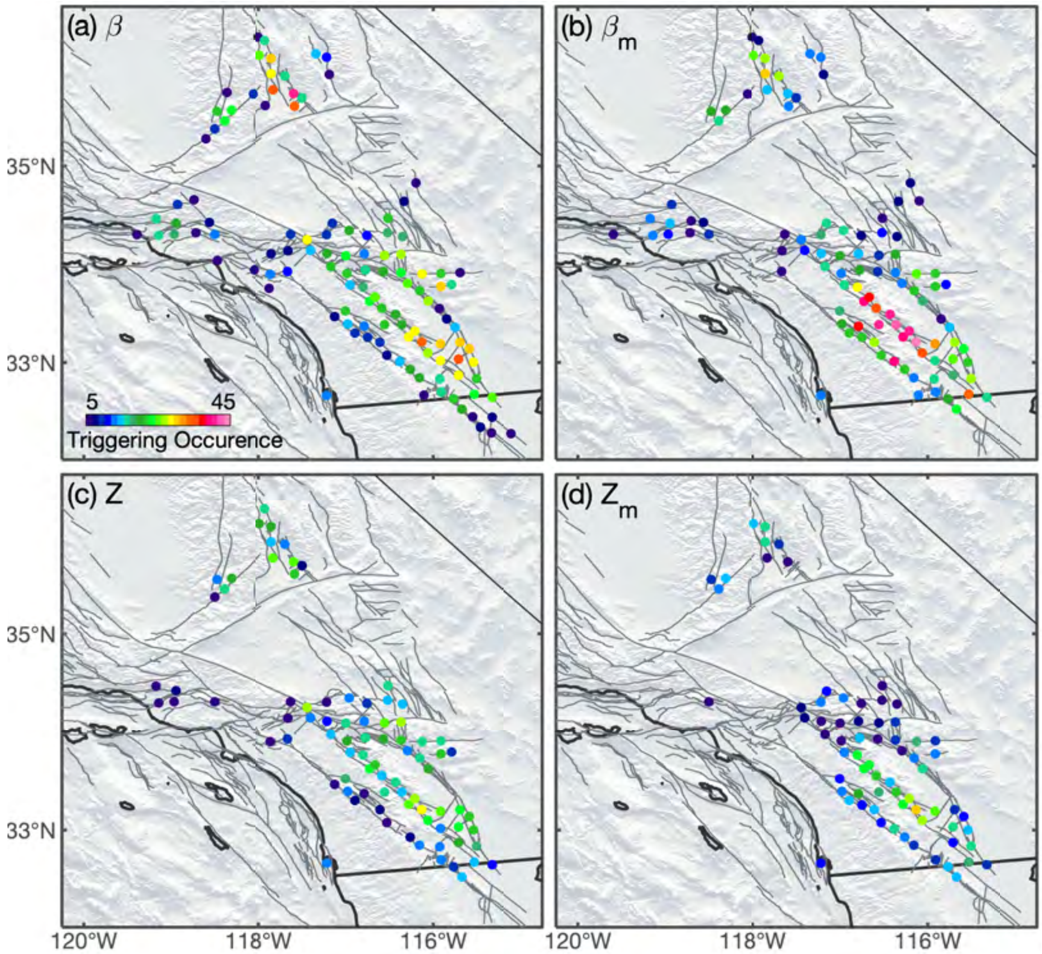

Figure 7: Triggering occurrence during the 24 hour (δ_a=24) time window using the β-statistic (a), β_m-statistic (b), Z-statistic (c), and Z_m-statistic (d).

3.3 Waveform Results

We measure waveform metrics (e.g., Figures 3-4) at all 222 grid points for the 1388 candidate trigger earthquakes, including events and grids that do not associate with seismicity-rate and moment-release anomalies (Figures 10-12). The measurements are then grouped into three categories: instantaneous (2-hour window), delayed (6- to 24-hour windows), and non-triggering. We examine distributions of waveform metrics for the three groups to evaluate their possible differences. For PGV in the 0.01–0.1 Hz band we observe no significant differences between the three distributions for the four test statistics (Figure 10a–d). Interestingly, instantaneous triggering cases seem to have a larger minimum PGV than the delayed cases in the 1–5 Hz frequency band (Figure 10e–h). The 1–5 Hz PGV distributions shift towards higher values compared to the delayed and non-triggering distributions in Figure 10e–h, most clear for the β_m- and Z_m-statistics. On average, a PGV threshold of 0.2 and 0.5 $\mu m/s$ in the 1–5 Hz band seems to be observed for the instantaneously triggered seismicity and moment-release anomalies, respectively. The threshold does not exclude occurrence of delayed and non-triggering cases as there are incidences of both groups with similar or greater PGV values. The observed high-frequency threshold is also observed in the FCR metric, manifesting as a leftward shift of the instanta-

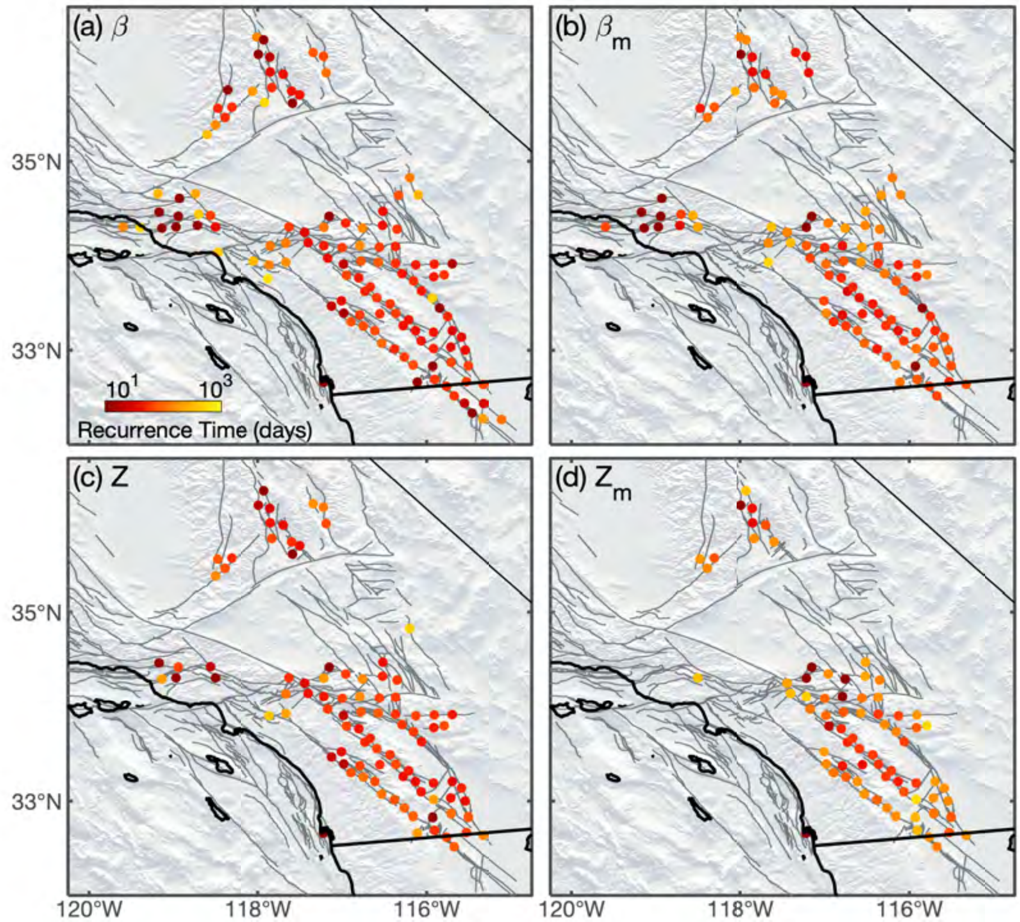

Figure 8: Median recurrence time at the qualified grid points using the β-statistic (a), β_m-statistic (b), Z-statistic (c), and Z_m-statistic (d).

neous distributions (Figure 11e–h), which suggests higher PGV values at high frequencies and therefore lower FCR values. There are no obvious differences in the distributions of the peak frequency or kinetic energy for the four test statistics (Figures 11a–d and 12). In summary, the waveform characteristics of the candidate earthquakes cannot deterministically differentiate the triggering incidence from non-triggering cases or separate instantaneous and delayed cases.

4 Discussion

Dynamically triggered seismicity occurs ubiquitously in southern California, albeit with strong occurrence heterogeneities in space and time. Moment-release anomalies share similar spatiotemporal patterns with the seismicity-rate anomalies but occur less frequently. In this section we will first evaluate the identification uncertainty and limitations (Section 4.1), and then examine possible triggering mechanisms (Section 4.5).

4.1 Uncertainty and Resolution

In this study, we identify seismicity-rate and moment-release anomalies at a 95% confidence level, and the identified anomalies are interpreted to associate with candidate

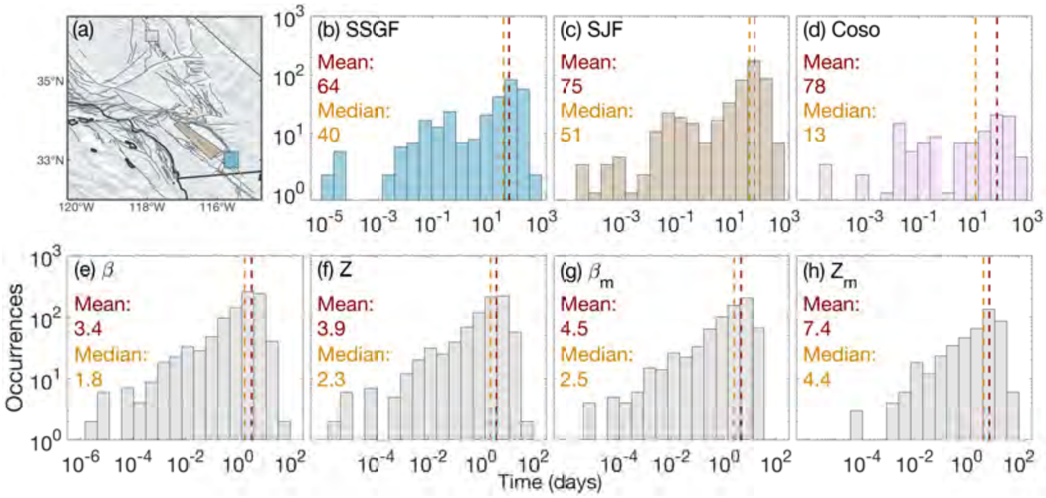

Figure 9: Distribution of triggering recurrence times at example sites and distribution of interevent times for southern California. (a) Map view of three sites. Each polygon may include more than one grid point, e.g., the San Jacinto Fault Zone. (b–d) Recurrence times at the Salton Sea Geothermal Field (b), the San Jacinto Fault Zone (c), and the Coso Geothermal Field (d). (e–f) Interevent times for southern California obtained using the the β-statistic (e), Z-statistic (f), β_m-statistic (g), and Z_m-statistic (h).

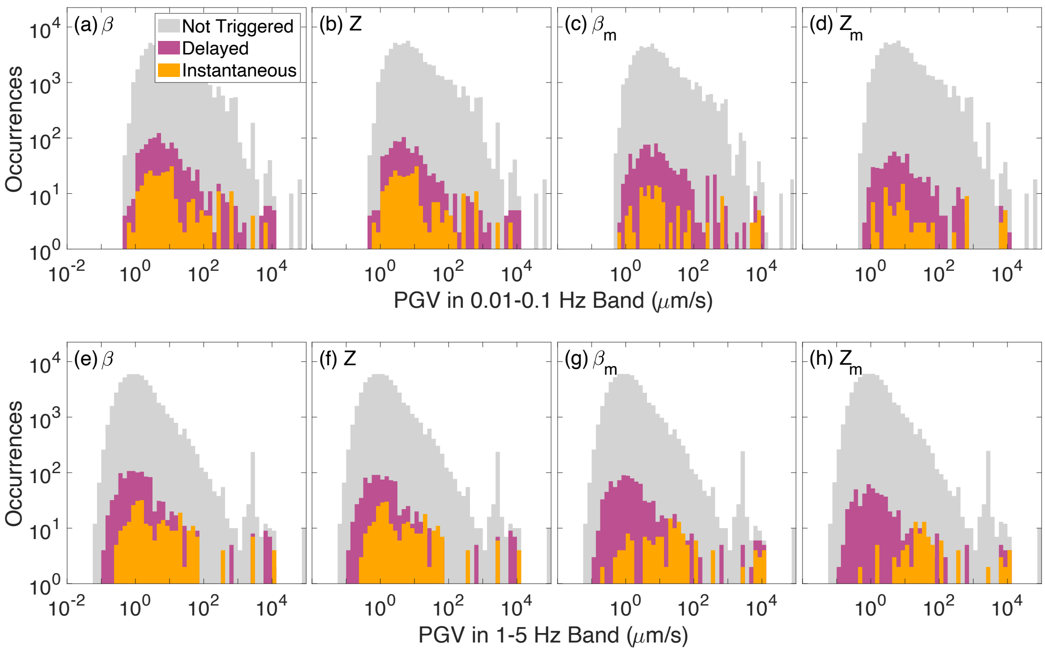

Figure 10: Distribution of PGV values in the 0.01–0.1 Hz (a–d) and 1–5 Hz (e–h) frequency bands for triggering identified by the β-statistic (a,e), Z-statistic (b,f), β_m-statistic (c,g), and Z_m-statistic (d,h). Histograms are color coded to represent the instantaneous triggering (yellow), delayed triggering (plum), and no triggering cases (gray).

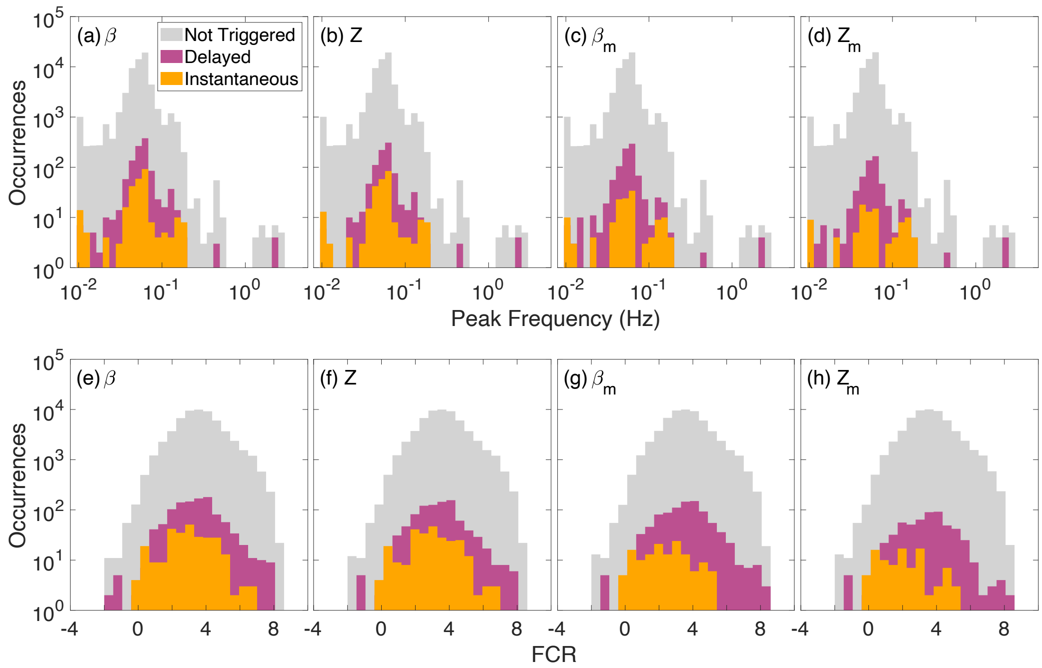

Figure 11: Distribution of peak frequency (a–d) and FCR (e–h) values for triggering identified by the β-statistic (a,e), Z-statistic (b,f), β_m-statistic (c,g), and Z_m-statistic (d,h). Histograms are color coded to represent the instantaneous triggering (yellow), delayed triggering (plum), and no triggering cases (gray).

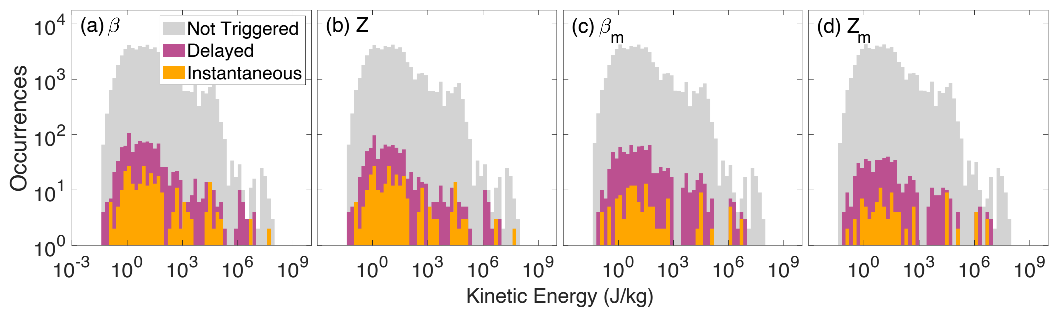

Figure 12: Distribution of kinetic energy values for triggering identified by the β-statistic (a), Z-statistic (b), β_m-statistic (c), and Z_m-statistic (d). Histograms are color coded to represent the instantaneous triggering (yellow), delayed triggering (plum), and no triggering cases (gray).

trigger earthquakes. We omitted locations that triggered less than five times from our results. Assuming each triggering case is independent and has a 5% chance of being a false positive, there is less than a 3.1×10^{-5}% probability that all triggering cases at a site are false positives if that site triggers at least five times. Our five-times selection criterion ensures that the observed spatial patterns are robust. Similarly, the temporal patterns are better resolved for sites with frequent triggering cases (Figure 9a–d), such as the San Jacinto Fault Zone, the Salton Sea Geothermal Field, and the Coso Geothermal Field. The identification of dynamic triggering could be influenced by a variety of factors, including background seismicity, magnitude of completeness, window length, af-

False Positive Rate	Poissonian Catalog	ETAS Catalog
β-statistic	0.87%	1.53%
Z-statistic	0.87%	1.46%
β_m-statistic	4.73%	2.26%
Z_m-statistic	3.35%	1.31%

Table 1: False positive rates of the statistical identification procedures when applied to a Poissonian and ETAS synthetic catalog.

tershocks of candidate events, and consecutive candidate earthquakes with short separations. To evaluate the robustness of the results, we examine the contribution of these factors item by item below. Through the suite of exercises, we confirm the robustness of our findings and outline possible biases in the results.

We generate two synthetic catalogs that do not include triggering cases to test the statistical procedures. We first generate a ten-year-long Poissonian catalog, where the occurrence of seismicity follows a Poisson distribution with magnitudes drawn from the probability distribution associated with the Gutenberg-Richter Law (Fiedler et al., 2018; Gutenberg & Richter, 1944). To construct the Poisson distribution we use an earthquake rate parameter of 0.002 earthquakes per second, equivalent to the number of earthquakes above completeness per second in the QTM catalog. We set the Gutenberg-Richter Law b-value to 0.99, an empirically obtained value for southern California (Hardebeck, 2013). Without losing generality, we assume that the seismicity occurs within the footprint of one grid point. We then randomly select 1,500 times to represent global candidate earthquakes and apply the same statistical procedures as detailed in Section 2.3 to evaluate the seismicity-rate and moment-release significance. Out of the 1,500 realizations, 0.87% of the cases are identified by both the β- and Z-statistics as anomalously high seismicity-rates, and 4.73% and 3.35% of the cases are labeled by the β_m- and Z_m-statistics as moment-release anomalies (Table 1). These cases are false positives, but the rates are less than the 5% threshold (95% confidence level) defined in our procedure.

The Poissonian catalog does not include mainshock-aftershock sequences of local earthquakes. Therefore, we design a second synthetic ten-year-long catalog following the temporal Epidemic-Type Aftershock Sequence (ETAS) model (Ogata, 1988), and the catalog is created using the procedure outlined in Shearer (2012a) and Shearer (2012b). The ETAS catalog includes both the random background seismicity and mainshock-aftershock sequences governed by the Omori-Utsu Law (Utsu, 1961). The ETAS parameters required in this formulation are aftershock productivity, b-value, and the Omori's Law time decay parameters c and p. We use an aftershock productivity of 0.003, an estimate specific to the QTM catalog from Miyazawa et al. (2021), a b-value of 0.99 (Hardebeck, 2013), a c value of 10^{-4} days, in accordance with Moutote et al. (2021) for the QTM catalog, and a p value of 1, near the global median value (Utsu et al., 1995; Zhuang et al., 2012). The earthquake magnitudes are randomly drawn from the same Gutenberg-Richter magnitude distribution used for the Poissonian catalog. Similarly, the seismicity is attributed to one grid point, and 1,500 time realizations are inspected. We find false-positive rates of 1.53% and 1.46% for the β- and Z-statistics and 2.26% and 1.31% for the β_m- and Z_m-statistics (Table 1). The false positive rates of all-four statistics are below 5% for the ETAS catalog. These tests confirm the effectiveness of the method.

We test if triggering occurrence correlates with the total number of earthquakes greater than M_c within each grid by computing the correlation coefficient (Figure 13a). The seismicity-rate anomalies identified by the β- and Z-statistics moderately correlate

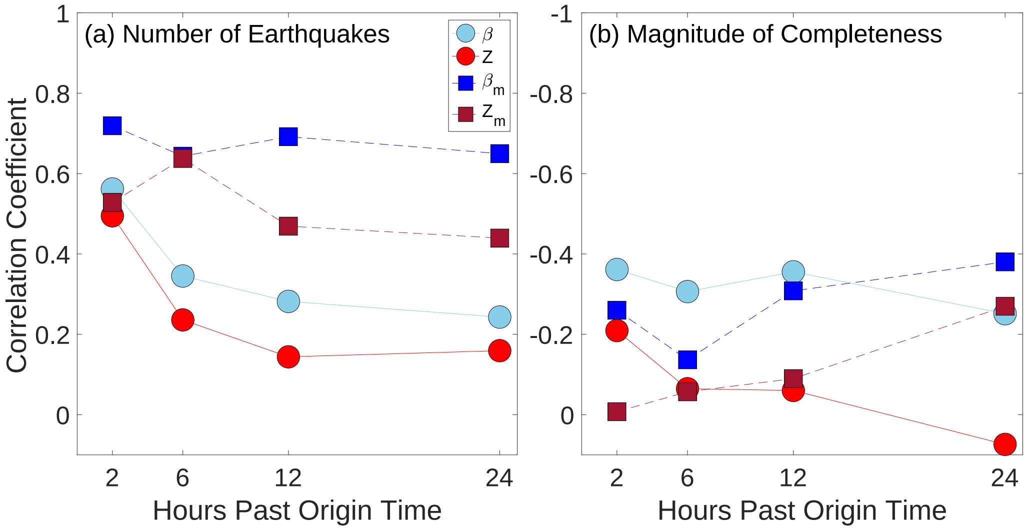

Figure 13: (a) Correlation coefficients between triggering occurrence and the number of earthquakes within the footprint of the grid points. (b) Correlation coefficients between triggering occurrence and the magnitude of completeness of earthquakes within the footprint of the grid points. Horizontal axis denotes the four time windows.

with the total earthquake number. Interestingly, the correlation coefficient is higher for instantaneous triggering than delayed cases. For example, the β-statistic has a correlation coefficient of 0.59 for the 2 hour window, but only 0.31 for the 24 hour window. A similar pattern is observed for the Z-statistic (Figure 13a). We find a strong correlation between the triggering occurrence of moment-release anomalies and the distribution of earthquake numbers. On average, the moment-release anomaly patterns identified by the β_m- and Z_m-statistics have correlation values around 0.5-0.7, differing from the seismicity-rate patterns (Figure 13a). There are some variations in the correlation values among different window lengths, i.e., correlations for the β_m-statistic vary from 0.76 at 2 hours to 0.68 at 24 hours, and correlations for Z_m-statistic oscillate in between 0.62 to 0.73 for the four window lengths. These results differ from Miyazawa et al. (2021) which found no correlation between the triggerability and seismicity-rate for a given site, but are in qualitative agreement with observations reported in van der Elst and Brodsky (2010). These correlation coefficients suggest that areas of higher background seismicity-rates are moderately more likely to experience frequent dynamic triggering.

Dynamically triggered earthquakes are generally small (Hill & Prejean, 2015), and lower magnitudes of completeness permit the identification of more triggered cases (Li et al., 2022). Therefore, the observed spatial pattern could be because the catalog has heterogeneous spatial resolutions. To determine the effect, we compute correlation coefficients between spatial patterns of the triggering occurrence and magnitude of completeness. The results are plotted in Figure 13b and show that each test statistic does not have a significant correlation with M_c since all coefficients are between -0.4 and 0.1. The seismicity anomalies identified by the β- and β_m-statistics generally have a higher negative correlation with M_c than their Z-counterparts (Figure 13b). The coefficients for the β_m- and Z_m-statistics typically decrease with time window (δ_a). For example, the coefficients range from -0.26 to -0.38 from 2 to 24 hours for the β_m-statistic, and they vary from -0.01 to -0.27 for the Z_m-statistic from 2 to 24 hours. The correlation values suggest that our identified cases are not significantly biased by the magnitude of completeness at different sites.

The overlapping δ_a windows may result in limited temporal resolutions of triggering types. For example, the 24 hour window includes seismicity from the 2 hour window, and intensely triggered seismicity in the 2 hour window could lead to an identification at a later time window, even if the triggered seismicity ceases. Such scenarios may complicate the extended cases but would not impact our identification of instantaneously triggered cases. However, identification of instantaneous cases may have been hampered by the coda of the passing seismic waves, which causes challenges in detecting and locating local microearthquakes. Furthermore, sporadic earthquakes could have been instantaneously triggered with a low seismicity-rate or low magnitudes (below M_c). These cases may have been missed by our procedure, which therefore may have underestimated the instantaneous triggering cases.

When multiple candidate earthquakes occur within 24 hours of each other and seismicity-rate and moment-release anomalies are identified at the sites of interest, it is challenging to separate the triggering contributions from the candidate earthquakes. In such cases, we consider that each of the earthquakes have contributed to cause the observed dynamic triggering, which may overestimate triggering occurrence. Specifically, M≥7 earthquakes often have M≥6 aftershocks, whose effects in dynamic triggering might be marginal. To evaluate the effect of M≥6 aftershocks in identifying dynamic triggering, we compare the results before and after removing aftershocks of the candidate trigger earthquakes. Removing potential aftershocks as candidate events may help avoid counting duplicate trigger earthquakes and underestimating the recurrence and interevent times.

For the removal procedure, we follow Knopoff et al. (1982) to define a spatial window to identify aftershocks of the candidate earthquakes. The Knopoff et al. (1982) mainshock footprint covers 100 km for an M6 event to 900 km for an M8 event. We use linear interpolation and extrapolation schemes to obtain the footprint dimension for a candidate trigger earthquake. If a smaller candidate event is within 24 hours (corresponding to the largest δ_a) of a previous event and is within its spatial area defined by Knopoff et al. (1982), the smaller earthquake is considered an aftershock of the greater candidate event, and it is excluded from the candidate trigger list. The spatial footprint from Knopoff et al. (1982) overestimates the aftershock zone and yields upper limits of the recurrence and interevent times. The percentage of candidate earthquakes that caused dynamic triggering is largely invariant to the aftershock removal procedure (Table 2). Additionally, the interevent times remain stable for the test statistics with less than one day of a difference. The aftershock removal exercise confirms the robustness of our finding and supports the conclusion that triggering is ubiquitous across southern California.

Not all large earthquakes close in time are part of the same sequence, and our procedure does not separate the triggering effects from multiple candidate earthquakes occurring within 24 hours. Multiple candidate earthquakes may increase the chances of dynamic triggering in southern California. We evaluate the hypothesis by examining the correlation between triggering occurrence and the number of candidate trigger earthquakes in the preceding 24 hours. When evaluating test statistics after each candidate earthquake, we count the number of global M≥6 earthquakes that occurred in the immediately preceding 24 hours, forming a ten-year time series. Correspondingly, we obtain a binary time series recording the triggering incidence. The correlation between the two time series has a coefficient of -0.02 for incidences identified using the β-statistic. The correlation coefficients for cases identified by other statistics (Z, β_m, and Z_m) have similar insignificant values. Therefore, we conclude that the presence of multiple candidate earthquakes within 24 hours does not impact the observed triggering patterns significantly.

4.2 Statistic Comparison

Several statistics have been introduced to measure the significance of seismicity-rate changes, e.g., the β-, Z-, and *gamma*-statistics (Habermann, 1983; Marsan & Nal-

	All candidate earthquakes	Aftershocks removed
Number of candidates	1388	1214
Percent of candidates that trigger (β)	70	68
Percent of candidates that trigger (Z)	60	60
Percent of candidates that trigger (β_m)	52	52
Percent of candidates that trigger (Z_m)	32	32
Interevent time in days (β)	3.4	4
Interevent time in days (Z)	3.9	4.5
Interevent time in days (β_m)	4.5	5.2
Interevent time in days (Z_m)	7.4	8.3

Table 2: Table of triggering results before and after removing aftershocks of candidate trigger earthquakes using the Knopoff et al. (1982) spatial footprint and a one-day temporal window.

bant, 2005; Matthews & Reasenberg, 1988). Assuming that earthquakes occur randomly, the probability distributions of the statistics can be derived analytically, and their significance threshold can be obtained through the distributions (e.g., Wyss & Marsan, 2011). The Z-statistic is often favored over the β-statistic because of its symmetric formulation (e.g., Aiken et al., 2018). However, the difference of the two statistics in identifying dynamic triggering is unclear because conventional approaches assume earthquake occurrence as a Possionian process, and a triggering threshold of 2 is widely adopted following this assumption, which is inaccurate for triggered seismicity.

To quantitatively compare the β- and Z-statistics (and the β_m- and Z_m-statistics), we compute correlation coefficients between pairs of statistics for each of the 1,388 candidate earthquakes at the sites of interest. Triggering occurrence of each statistic is recorded in a binary array, with values consisting of either a 0 (non-triggered) or 1 (triggered) for the 222 grid points. The correlation coefficient is calculated between the resulting arrays for each statistic pair. This produces one coefficient for each candidate earthquake. A higher resulting correlation coefficient shows a higher level of consistency between the two statistics while a lower coefficient shows less consistency. The correlation coefficients are computed for each time window (Figure 14). Additionally, a coefficient examining whether any triggering occurred at a grid for an earthquake is computed between statistic pairs (Figure 14). With the collection of coefficient values, we find that seismicity anomalies identified by the β- and Z-statistics are highly correlated with over half of incidences having a coefficient of 1 (Figure 14a). Similarly, moment-release anomalies identified by the β_m- and Z_m-statistics have high correlations with low variances (Figure 14d). Correlation between the seismicity-rate and moment-release anomalies are noticeably different, with smaller median coefficients and larger variances (Figure 14b,c). The results are consistent with the triggering rate results that seismicity-rate changes occur more frequently than moment-release anomalies. The results indicate that the choice of test statistic (e.g., β- or Z-statistic) is not crucial for our sampling procedure.

Although the differences in results between the β- and Z-statistics are minor, the β-statistic identifies more seismicity-rate anomalies than the Z-statistic, which is likely due to the Z-statistic being a symmetric formulation of the β-statistic (Wyss & Marsan, 2011). Both the β_m- and Z_m-statistics identify fewer moment-release anomalies than the seismicity-rate changes. However, significant moment-release anomalies are still common, with 54% and 34% triggering rates from the β_m- and Z_m-statistics. The synthetic cat-

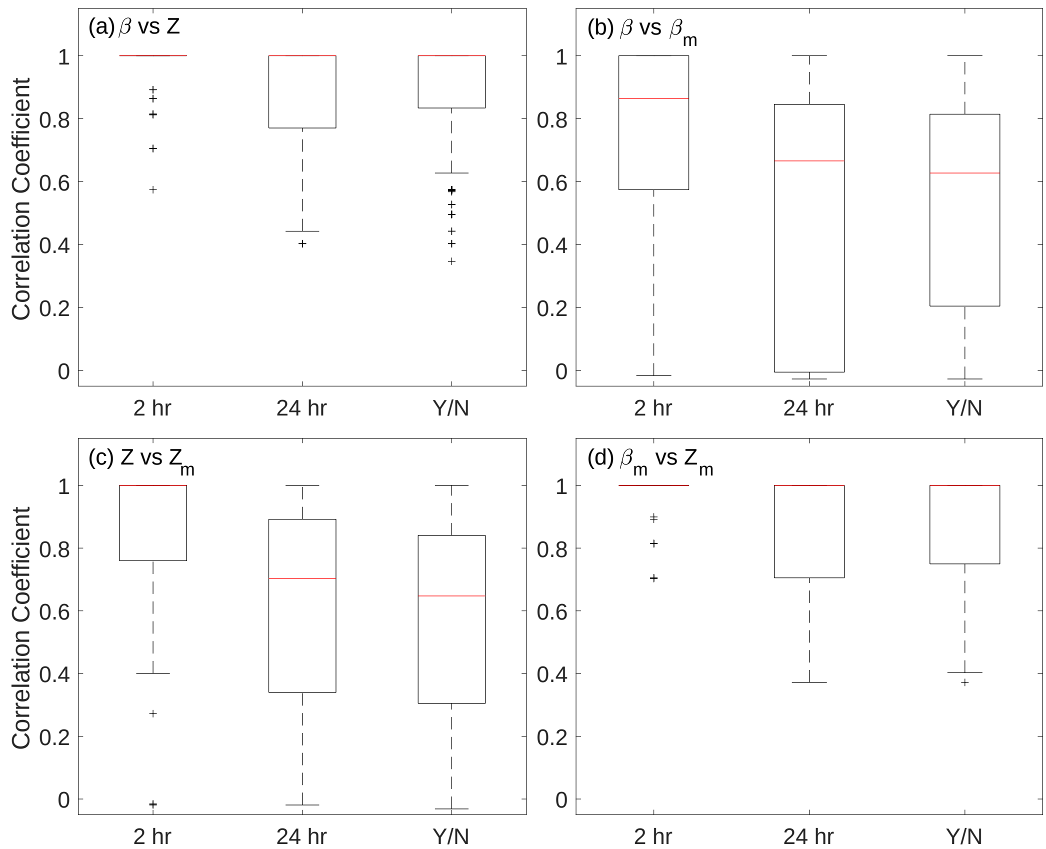

Figure 14: Boxplots of correlation coefficients between the four statistics. Here Y/N denotes if triggering was identified in any of the four time windows. Red line marks the median and the surrounding box denotes the interquartile range. Dashed lines show the range, omitting outliers. Outliers are denoted by plus-symbols, and are values greater than the third quartile plus 1.5 times the interquartile range or less than the first quartile minus 1.5 times the interquartile range.

alog tests show that the symmetric formulations, e.g., Z- and Z_m-statistics, are more accurate in comparison to their counter parts, although the differences are small.

The difference in results between the seismicity-rate and moment-release anomalies suggest that dynamically triggered seismicity in southern California is commonly observed while large earthquakes (significant moment-releases) are less frequently triggered (Figure 3.1). For example, the Salton Sea and Coso Geothermal Fields frequently experience dynamic triggering in seismicity, but do not have moment-release anomalies very often. It is likely because the thermal production areas are dominated by fragmented faults with small spatial extents (e.g., Cheng & Chen, 2018), limiting the triggered earthquake sizes. Similarly, the immature Ridgecrest fault system may contain more small fault strands (e.g., Ross, Idini, et al., 2019), which may have contributed to the triggering differences of seismicity-rate and moment-release in the region. In contrast, the San Jacinto and Elsinore faults have comparable triggering occurrence for the seismicity-rate and moment-release anomalies.

Moment-release anomalies are identified every week on average in southern California by the β_m- and Z_m-statistics. The moment-release anomalies are dominated by the largest earthquakes in the time windows. However, we note that our statistical tests cannot determine whether a specific individual earthquake was dynamically triggered. For simplicity, we convert the moment-anomalies to their equivalent moment magnitudes (Figure 15), remove duplicates from overlapping grid points and time windows, and find a nominal moment-release anomaly of M_w 3 (Figure 15). Intriguingly, the β_m- and Z_m-statistics identified 6 and 5 cases with equivalent moments above M_w 5, respectively. The cases correspond to 26% and 22% of the total M≥5 earthquakes in southern California during the study period. Except for one event likely related to the 2010 El Mayor Cucapah earthquake, each case was identified as delayed triggering with delay times beyond 6 and up to 24 hours. Close inspections of seismicity during the delay times reveal no obvious foreshock sequences for these cases. Our procedure cannot conclude whether these specific cases were dynamically triggered or not. Further, the delayed nature hinders rejecting the null hypothesis that the occurrence was random. These unusual M≥5 cases warrant detailed investigations in future follow-up studies.

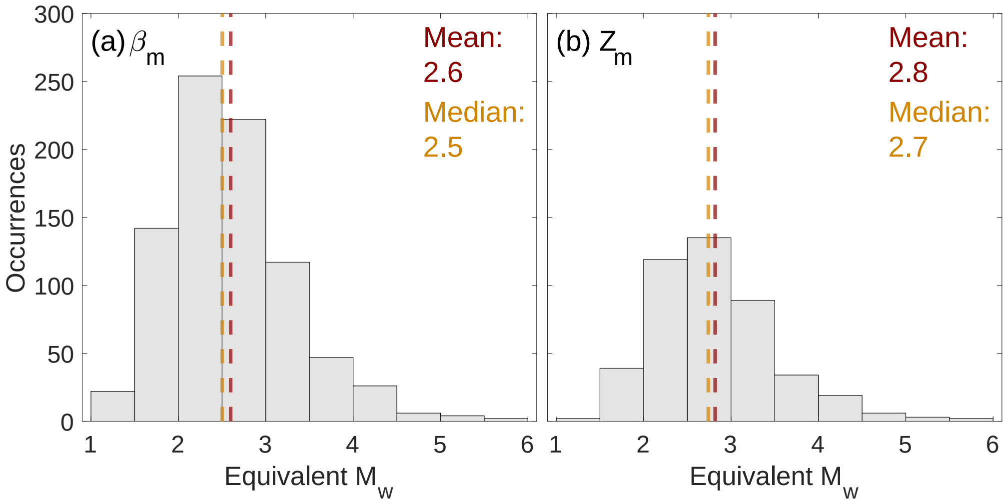

Figure 15: Distributions of equivalent moment magnitudes of the moment-release anomalies identified by the β_m- and Z_m-statistics. For extended triggering cases, the equivalent moment magnitudes are computed using the longest time window corresponding to a trigger earthquake.

4.3 Triggering Scale

To investigate the spatial footprint of the triggered seismicity and moment-release anomalies, we develop a metric of synchronization, termed the synchronization coefficient, $S_{i,j}$, between pairs of grid points:

$$S_{i,j} = \frac{N_s}{N_{tot}}, \tag{10}$$

where i and j are the indexes of two grid points, N_s is the number of shared candidate earthquakes that have caused dynamic triggering at both grids, and N_{tot} is the number of unique candidate earthquakes that have caused dynamic triggering at either or both of the grids. We define synchronization as grid points triggered by the same candidate earthquakes. $S_{i,j}$ is defined to range from 0 to 1. $S_{i,j} = 1$ denotes 100% synchronization, where dynamic triggering concurs at both grids every time the grids trigger. $S_{i,j} = 0$ indicates that dynamic triggering is not observed simultaneously at the two grids during the study period. We pairwise calculate $S_{i,j}$ for the grid points and investigate the parameter as a function of the separation distance between the ith and jth grids.

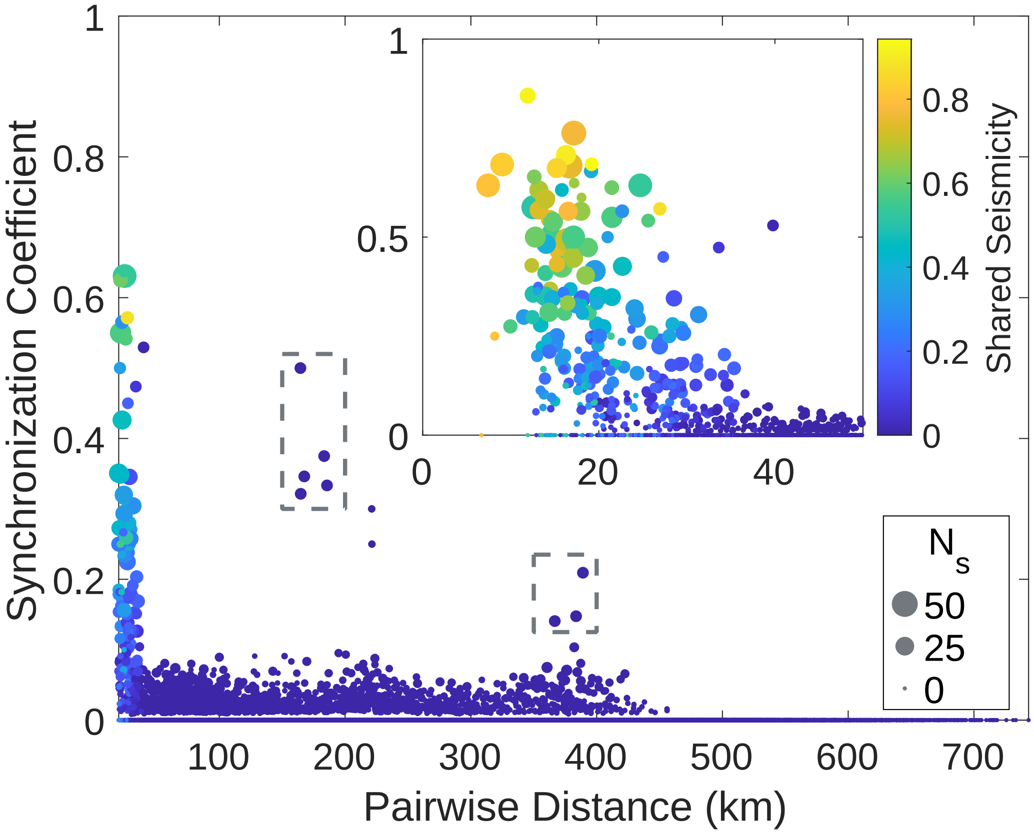

Figure 16: Synchronization coefficient versus pairwise grid distance. Inset displays a zoom-in view for grids that are less than 50 km apart. Marker color shows the proportion of local earthquakes that are shared between grid pairs during the study period. Marker size indicates the number of candidate earthquakes that cause triggering at both locations, N_s.

We hypothesize that high synchronization coefficients reflect common triggering processes occurring at the grids and the separation distance may serve as a proxy of the spatial dimension of the processes (Figure 16). For example, there is a sharp drop in $S_{i,j}$ after a distance of 40 km for seismicity-rate anomalies identified using the β-statistic. Given the gridding configuration (Section 2.2), the 40 km threshold roughly equals the distance between the centers of two grid points. Since the footprints overlap between adjacent grids, the observed high synchronization may reflect some shared seismicity. Therefore, the results suggest highly localized triggering responses of seismicity in southern California, clustering over small spatial scales, likely on the order of 40 km or smaller. We observe the same pattern for the Z-, β_m-, and Z_m-statistics.

Synchronization coefficients are generally low for grids separated beyond 40 km. However, there are two groups of outliers, denoted by the gray boxes in Figure 16, with a pairwise distance over 40 km. The first group of five pairs is around 175 km apart, and the second group is around 400 km apart. The first group associates with triggering responses from the 2015 M8.3 Illapel earthquake, Chile and its aftershocks, and the second group is due to the 2010 M8.8 Maule earthquake, Chile and its aftershocks. The two groups may suggest simultaneous triggering incidences across southern California due to the two M>8 earthquake sequences. These two groups are very rare cases as most grid pairs have low synchronization coefficients. In summary, our results suggest that triggering processes at different faults in southern California are primarily uncorrelated, and the triggering responses are highly heterogeneous. To investigate such processes, a dense network with comparable spatial scales (40 km), such as the Japanese Hi-net (Okada et al., 2004), is needed to accurately resolve the waveform characteristics within each grid.

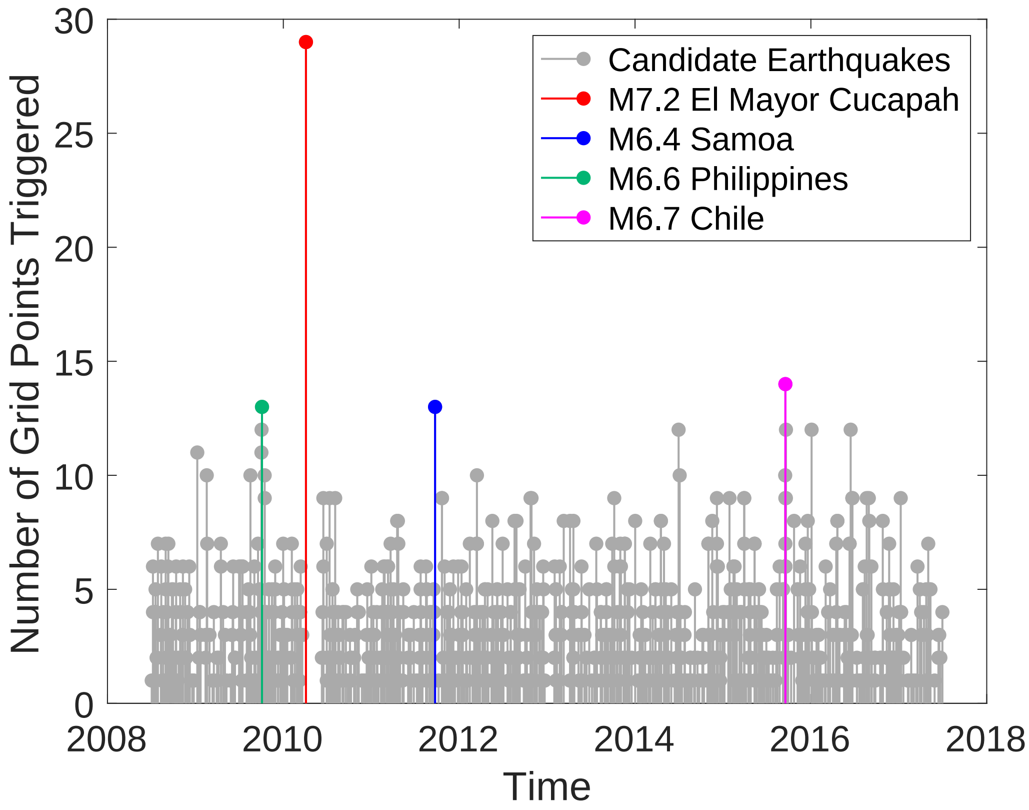

Figure 17: Time series of the number of grid points triggered after each candidate earthquake (β-statistic). Candidate earthquakes within 60 days following the 2010 El Mayor Cucapah earthquake are not analyzed (Section 2.1).

Another way to investigate the triggering scale is to count the number of triggered grids by each candidate trigger earthquake (Figure 17). We find large variability in triggering response among different candidate trigger earthquakes. For example, the 2010 El Mayor Cucapah (EMC) earthquake triggered the most seismicity-rate anomalies (β-statistic) in southern California. Seismicity was triggered at 29 grid points (Figure S6) even after excluding locations within 50 km of the epicenter. The results agree with findings in Ross, Trugman, et al. (2019) and Meng and Peng (2014). An M6.7 aftershock of the 2015 M8.3 Illapel, Chile earthquake is the second most productive trigger earthquake, causing seismicity anomalies at 14 grid points. The 2009 M6.6 Philippines earthquake and the 2011 M6.4 Samoa earthquake both correlate with seismicity-rate anomalies at 13 grid points. On average, the candidate earthquakes cause triggering at about three sites. These results further confirm that dynamic triggering occurs at local scales, and the triggering responses at different sites are usually independent. Similar plots for the other three statistics (Z, β_m, and Z_m) are included in the Supplementary Material.

4.4 Triggering Threshold

We find the triggering thresholds have large variabilities and are spatially heterogeneous (Figures 18 and 19). We examine all thresholds that are used for identifying anomalies of each statistic, and focus on discussing the the 95^{th} percentile thresholds (e.g. $\beta^a_{95\%}$) in this study as it is the most critical threshold used in our procedure. In general, the thresholds for identifying anomalies at the 95^{th} percentile are greater than 2 (e.g., $\beta^a_{95\%} \geq 2$), as reported in previous studies (Fan et al., 2021; Marsan & Nalbant, 2005). Figures 18 and 19 show that the median 95% thresholds of the four test statistics at each grid point are all above 2, suggesting that using a threshold of 2 would overestimate triggering occurrences in southern California. The San Jacinto Fault, Elsinore Fault, and Coso Geothermal Field have relatively high values of the $\beta^a_{95\%}$ and $Z^a_{95\%}$ triggering thresholds in the 2-hour window (Figure 18) while the Salton Sea Geothermal Field has a lower threshold. The spatial pattern does not seem to correlate with seismicity-rates or triggering occurrence. In contrast, the $\beta^a_{m-95\%}$ and $Z^a_{m-95\%}$ triggering thresholds in the 2-hour window have significantly less spatial variation. The thresholds for the 24-hour window have the opposite patterns, the spatial heterogeneity for $\beta^a_{95\%}$ and $Z^a_{95\%}$ is less significant in comparison to those of the 2-hour window, while there is an increase in spatial heterogeneity for the $\beta^a_{m-95\%}$ and $Z^a_{m-95\%}$ triggering thresholds. The thresholds also evolve over short time scales at each grid point. For example, Figure 20 shows the temporal evolution of the 95^{th} percentile thresholds at the Salton Sea Geothermal Field for the 2-hour window. We observe that the thresholds vary significantly with time over the nine year period, especially for the $\beta^a_{95\%}$ and $Z^a_{95\%}$ thresholds. The findings suggest that the triggering thresholds are space- and time-dependent, indicating constantly evolving faulting conditions, and our data-driven approach is effective in accounting for such variabilities and can effectively identify dynamic triggering cases.

4.5 Physical Mechanisms

A variety of physical processes may have occurred during earthquake dynamic triggering (Brodsky & Prejean, 2005; Freed, 2005; Prejean & Hill, 2018), and Coulomb failure due to the transient stress perturbation can intuitively explain the instantaneously triggered cases (Gonzalez-Huizar & Velasco, 2011; Hill, 2008; Kilb, 2003). In this case, faults are at critical states, and the dynamic stress from the seismic waves pushes the faults to slip. Assuming the faults are at a uniform critical condition, there might be a correlation between the triggering occurrence and the instantaneous waveform metrics. Our waveform analyses find no obvious correlations between triggering occurrence and the waveform metrics, including peak ground velocity and kinetic energy. The findings agree with previous searches for PGV-based triggering thresholds, where no simple thresholds have been confirmed (Freed, 2005; Hill & Prejean, 2015). Intriguingly, the instantaneously triggered seismicity and moment-release anomalies seem to require a minimum peak ground velocity above 0.2-0.5 $\mu m/s$, a unique feature compared to non-triggering and delayed triggering cases. However, such triggering cases do not always occur when the threshold is reached.

The 2010 El Mayor Cucapah earthquake has caused widespread triggering responses (Figure S6), including both static and dynamic triggering cases (Meng & Peng, 2014; Miyazawa et al., 2021; Ross, Trugman, et al., 2019). The earthquake offers an opportunity to inspect relations between the triggering occurrence and waveform metrics. We find no obvious correlations between the triggering occurrence and the PGV distribution; sites with comparably high PGV values show different triggering responses. For the El Mayor Cucapah earthquake, static triggering may have also regulated the triggering response in southern California (Meng & Peng, 2014). To further evaluate the Coulomb failure mechanism, we investigate candidate events that caused dynamic triggering at 10 or more grid points, and find no clear patterns. We also find that the earthquakes with the most widespread triggering responses have no obvious characteristic features in mag-

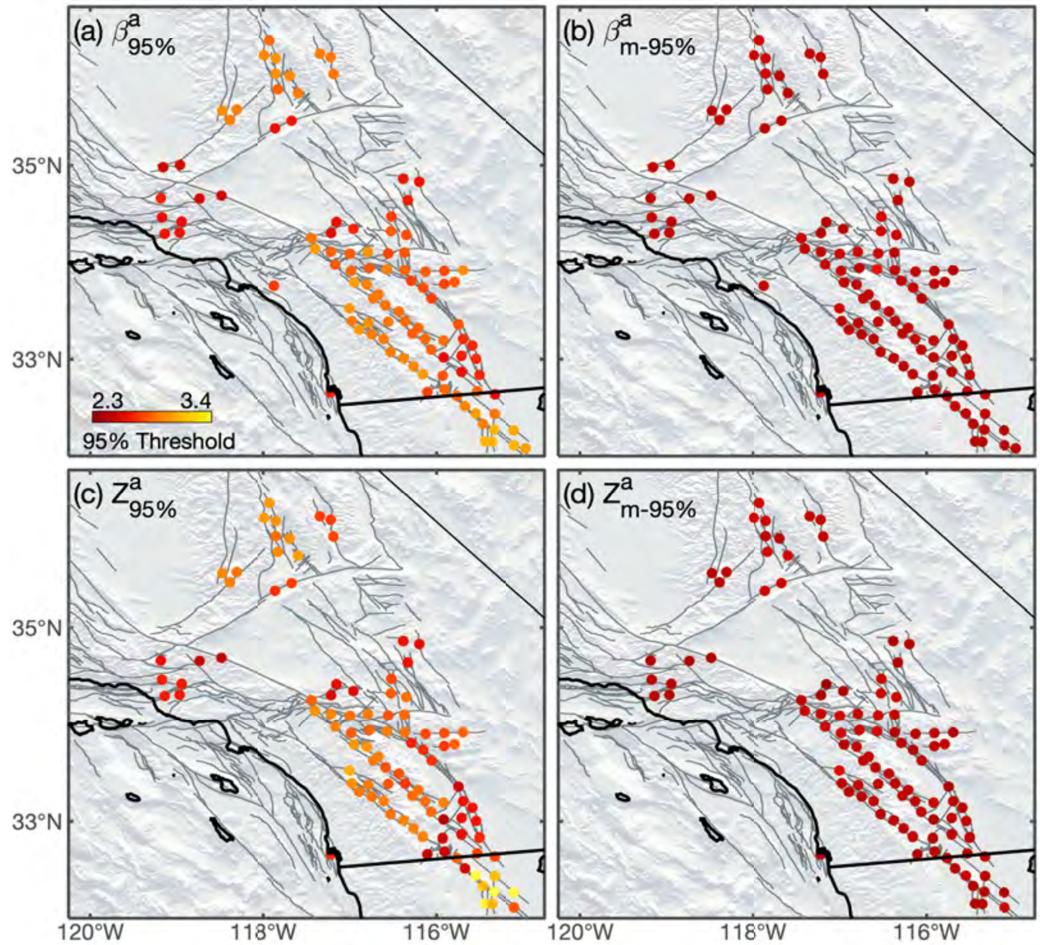

Figure 18: Spatial patterns of the median of the 95% percentile thresholds during the 2 hour time window for the β-statistic (a), β_m-statistic (b), Z-statistic (c), and Z_m-statistic (d).

nitude or location. The negative results may be due to that the faults were at different critical states, requiring different levels of stress perturbations. Additionally, the local stress field may have facilitated triggering for incoming waves from preferred azimuths (Alfaro-Diaz et al., 2020; Gonzalez-Huizar & Velasco, 2011). Alternatively, nonlinear triggering processes that were governed by rate- and state-fault properties may have regulated some of the triggering processes.

Delayed dynamic triggering requires time-dependent developments of slips and failures, which are likely controlled by non-linear mechanisms (e.g. Fan et al., 2021; Hill & Prejean, 2015; Miyazawa et al., 2021; Shelly et al., 2011). The non-linear triggering process could include a combination of mechanisms such as rate-and-state friction, material fatigue, aseismic slip, pore pressure, permeability enhancement, and granular flow among others (Brodsky & van der Elst, 2014; Hill & Prejean, 2015; Johnson & Jia, 2005; Rivera & Kanamori, 2002). Such processes may correlate better with wavefield features, including the frequency content of the passing seismic waves and the duration of intense ground motions. For example, triggering occurrence seems to relate to the PGV in low frequency bands at Long Valley (Brodsky & Prejean, 2005) and Parkfield (Guilhem et al., 2010). Our observations of delayed cases require nonlinear processes to initiate dy-

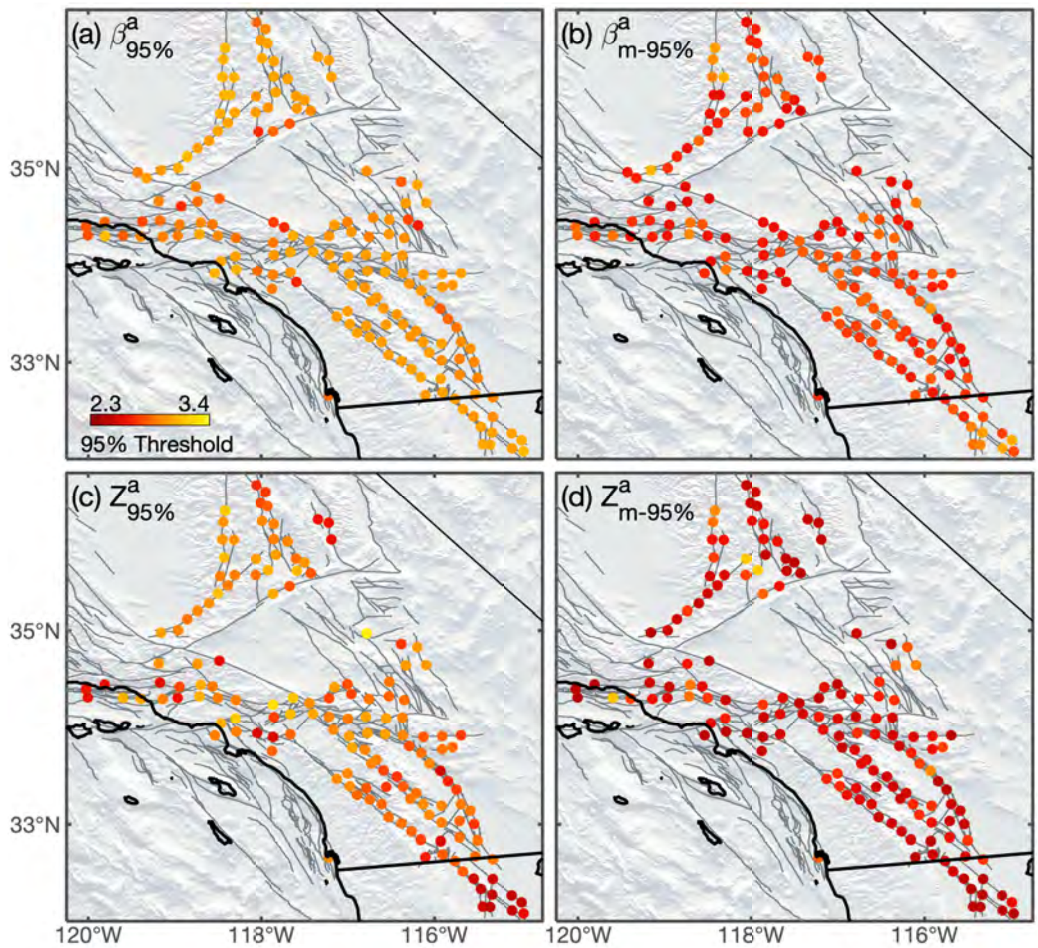

Figure 19: Spatial patterns of the median of the 95% percentile thresholds during the 24 hour time window for the β-statistic (a), β_m-statistic (b), Z-statistic (c), and Z_m-statistic (d).

namic triggering in southern California. Particularly, we find no correlation with the PGV or kinetic energy (Figures 10 and 12), nor any systematic correlations with the peak frequency or frequency content (Figure 11).

Our analyses of triggering scale show that the spatial footprint of triggering is localized and suggests that dynamic triggering is governed by conditions operating on spatial scales of tens of kilometers. Such heterogeneity may help explain the diverse triggering responses, including that Coulomb failure may be the driver for instantaneous triggering cases. Importantly, the results highlight that local conditions may play a more important role in the occurrence of triggering than features of the incoming wave, emphasizing the importance of understanding the heterogeneous stress and strength states of faults in southern California.

Models including experimentally derived rate- and state-dependent fault properties suggest that earthquake production relates to the local stress states, and the stressing episodes due to the passing seismic waves may produce clusters of earthquakes in these regions (Dieterich, 1994). We find a moderate correlation between seismicity-rate anomalies and the total number of earthquakes above completeness at each grid point (Figure 13a).

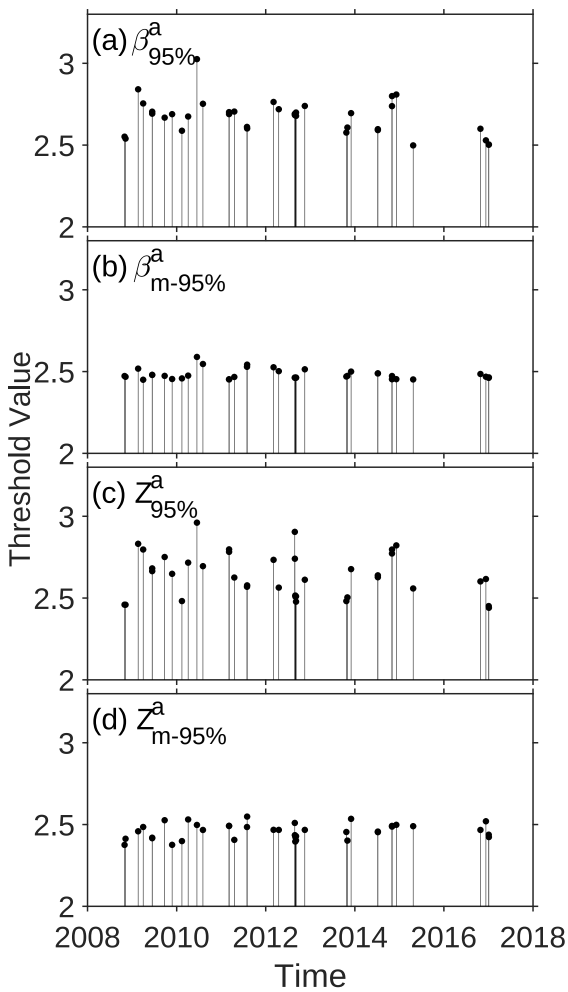

Figure 20: Temporal evolution of the 95% percentile thresholds during the 2 hour time window at a site in the Salton Sea Geothermal Field for the β-statistic (a), β_m-statistic (b), Z-statistic (c), and Z_m-statistic (d).

The correlation coefficients decrease with δ_a, which suggests that the instantaneous triggering cases are likely dominated by linear processes acting upon the heterogeneous stress field, while the delayed cases are likely caused by complex nonlinear processes. The strong correlation values observed for the moment-anomalies may have been due to the observation that more seismically active regions can generate larger earthquakes.

The clear evidence of dynamic triggering operating on local spatial scales ($\sim$40 km) suggests that the process is irrelevant to the macro-scale tectonic regimes, such as reported in Velasco et al. (2008). However, there is conflicting evidence showing that larger-scale tectonic processes can inhibit dynamic triggering (Harrington & Brodsky, 2006), suggesting directions for future comparative investigations. Qualitatively, we notice that frequent triggering occurs at the San Jacinto Fault, Salton Sea Geothermal Field, Coso Geothermal field, and the merging connection of the San Andreas and San Jacinto faults, where the fault geometries are complex (Chu et al., 2021; Marshall et al., 2022). The geometric complexities may further indicate complex stress fields at those sites (Yang & Hauksson, 2013). We experimented computing correlations between the triggering occurrence and the surface trace complexity metrics from Chu et al. (2021) but found no obvious correlation. It is possible that the surface traces do not fully reflect the 3D fault geometry and stress field complexities, and future investigations on the relations between earthquake focal mechanisms and triggering occurrence may offer new insights into the physical mechanisms of dynamic triggering processes.

5 Conclusions

We have developed an assumption-free approach to statistically identify seismicity-rate and moment-release anomalies caused by earthquake dynamic triggering. We apply the method to southern California seismicity from 2008 to 2017 and find

1. Earthquake dynamic triggering is ubiquitous throughout southern California, and up to 70% of the global M≥6 earthquakes may have caused dynamic triggering in the region.
2. Dynamic triggering was identified at most of the major faults in the area. The Salton Sea Geothermal Field, Coso Geothermal Field, and San Jacinto Fault are the most prone regions to triggering.
3. Dynamic triggering occurs every 4 days on average in southern California.
4. Individual sites in southern California are triggered less frequently, ranging from once a month to every few years.
5. Most dynamic triggering cases are delayed.
6. Significant moment-release anomalies are common in southern California, but occur less often than significant seismicity-rate increases.
7. The β-based and Z-based test statistics identify similar sets of dynamic triggering cases.
8. There are no clear connections between triggering patterns and instantaneous waveform metrics, including the peak ground velocity, peak frequency, kinetic energy, and frequency content.
9. Local fault conditions likely govern dynamic triggering occurrence.

These observations suggest that time-dependent nonlinear mechanisms acting on local scales are likely responsible for the majority of the observed triggering cases.

6 Open Research

Data Availability Statement

The earthquake catalogs used in this study are from the International Seismological Centre (ISC) catalog (International Seismological Centre, 2022) and the Southern California Earthquake Data Center (Quake Template Matching catalog; Ross, Trugman, et al., 2019). The facilities of IRIS Data Services, and specifically the IRIS Data Management Center, were used for access to the seismic waveforms and the ISC catalog, related metadata, and/or derived products used in this study. IRIS Data Services are funded through the Seismological Facilities for the Advancement of Geoscience and EarthScope (SAGE) Proposal of the National Science Foundation (NSF) under Cooperative Agreement EAR-1261681. The seismic data were downloaded using ObsPy (Beyreuther et al., 2010) and the International Federation of Digital Seismograph Networks (FDSN) web services.

Acknowledgments

We thank Peter Shearer for sharing codes to generate the ETAS synthetic catalog and useful discussion. We acknowledge support from NSF grant EAR-2022441.

References

Abercrombie, R. E., & Mori, J. (1996). Occurrence patterns of foreshocks to large earthquakes in the western united states. *Nature*, *381*(6580), 303–307. doi: 10.1038/381303a0

Aiken, C., Meng, X., & Hardebeck, J. (2018). Testing for the 'predictability'of dynamically triggered earthquakes in the geysers geothermal field. *Earth and Planetary Science Letters*, *486*, 129–140. doi: 10.1016/j.epsl.2018.01.015

Aiken, C., & Peng, Z. (2014). Dynamic triggering of microearthquakes in three geothermal/volcanic regions of California. *Journal of Geophysical Research: Solid Earth*, *119*(9), 6992–7009. doi: 10.1002/2014JB011218

Alfaro-Diaz, R., Velasco, A. A., Pankow, K. L., & Kilb, D. (2020). Optimally oriented remote triggering in the coso geothermal region. *Journal of Geophysical Research: Solid Earth*, *125*(8), e2019JB019131.

Beyreuther, M., Barsch, R., Krischer, L., Megies, T., Behr, Y., & Wassermann, J. (2010). Obspy: A python toolbox for seismology. *Seismological Research Letters*, *81*(3), 530–533. doi: 10.1785/gssrl.81.3.530

Bosl, W., & Nur, A. (2002). Aftershocks and pore fluid diffusion following the 1992 landers earthquake. *Journal of Geophysical Research: Solid Earth*, *107*(B12), ESE–17. doi: 10.1029/2001JB000155

Bowman, A. W., & Azzalini, A. (1997). *Applied Smoothing Techniques for Data Analysis: The Kernel Approach with S-Plus Illustrations* (1st edition ed.). Oxford : New York: Oxford University Press.

Brodsky, E. E., & Prejean, S. G. (2005). New constraints on mechanisms of remotely triggered seismicity at Long Valley Caldera. *Journal of Geophysical Research: Solid Earth*, *110*(B4). doi: 10.1029/2004JB003211

Brodsky, E. E., & van der Elst, N. J. (2014). The Uses of Dynamic Earthquake Triggering. *Annual Review of Earth and Planetary Sciences*, *42*(1), 317–339. doi: 10.1146/annurev-earth-060313-054648

Buurman, H., & West, M. E. (2010). *Seismic precursors to volcanic explosions during the 2006 eruption of Augustine Volcano: Chapter 2 in The 2006 eruption of Augustine Volcano, Alaska* (Tech. Rep. No. 1769-2). U.S. Geological Survey. (ISSN: 2330-7102 Publication Title: Professional Paper) doi: 10.3133/pp17692

Cattania, C., McGuire, J. J., & Collins, J. A. (2017). Dynamic triggering and earthquake swarms on east pacific rise transform faults. *Geophysical Research Letters*, *44*(2), 702–710. doi: 10.1002/2016GL070857

Cheng, Y., & Chen, X. (2018). Characteristics of seismicity inside and outside the salton sea geothermal field. *Bulletin of the Seismological Society of America*, *108*(4), 1877–1888.

Chu, S. X., Tsai, V. C., Trugman, D. T., & Hirth, G. (2021). Fault Interactions Enhance High-Frequency Earthquake Radiation. *Geophysical Research Letters*, *48*(20), e2021GL095271. doi: 10.1029/2021GL095271

Dieterich, J. (1994). A constitutive law for rate of earthquake production and its application to earthquake clustering. *Journal of Geophysical Research: Solid Earth*, *99*(B2), 2601–2618. doi: 10.1029/93JB02581

Fan, W., Barbour, A. J., Cochran, E. S., & Lin, G. (2021). Characteristics of Frequent Dynamic Triggering of Microearthquakes in Southern California. *Journal of Geophysical Research: Solid Earth*, *126*(1). doi: 10.1029/2020JB020820

Fan, W., Okuwaki, R., Barbour, A. J., Huang, Y., Lin, G., & Cochran, E. S. (2022). Fast rupture of the 2009 Mw 6.9 Canal de Ballenas earthquake in the Gulf of California dynamically triggers seismicity in California. *Geophysical Journal International*, *230*(1), 528–541. doi: 10.1093/gji/ggac059

Fiedler, B., Hainzl, S., Gert Zöller, & Holschneider, M. (2018). Detection of Gutenberg–Richter b-Value Changes in Earthquake Time Series. *Bulletin of the Seismological Society of America*, *108*(5A), 2778–2787. doi: 10.1785/0120180091

Field, E. H., Arrowsmith, R. J., Biasi, G. P., Bird, P., Dawson, T. E., Felzer, K. R., . . . Zeng, Y. (2014). Uniform California Earthquake Rupture Forecast, Version 3 (UCERF3)—The Time-Independent Model. *Bulletin of the Seismological Society of America*, *104*(3), 1122–1180. doi: 10.1785/0120130164

Freed, A. M. (2005). Earthquake Triggering by Static, Dynamic, and Postseismic Stress Transfer. *Annual Review of Earth and Planetary Sciences*, *33*(1), 335–367. doi: 10.1146/annurev.earth.33.092203.122505

Gomberg, J. (1996). Stress/strain changes and triggered seismicity following the Mw 7.3 Landers, California earthquake. *Journal of Geophysical Research: Solid Earth*, *101*(B1), 751–764. doi: 10.1029/95JB03251

Gomberg, J., & Johnson, P. (2005). Dynamic triggering of earthquakes. *Nature*, *437*(7060), 830–830. doi: 10.1038/437830a

Gomberg, J., Reasenberg, P., Bodin, P. l., & Harris, R. (2001). Earthquake triggering by seismic waves following the landers and hector mine earthquakes. *Nature*, *411*(6836), 462–466. doi: 10.1038/35078053

Gonzalez-Huizar, H., & Velasco, A. A. (2011). Dynamic triggering: Stress modeling and a case study. *Journal of Geophysical Research: Solid Earth*, *116*(B2). doi: 10.1029/2009JB007000

Guilhem, A., Peng, Z., & Nadeau, R. M. (2010). High-frequency identification of non-volcanic tremor triggered by regional earthquakes. *Geophysical Research Letters*, *37*(16). doi: 10.1029/2010GL044660

Gutenberg, B., & Richter, C. (1944). Frequency of Earthquakes in California. *Bulletin of the Seismological Society of America*, *34*, 185–188.

Habermann, R. E. (1981). Precursory seismicity patterns: stalking the mature seismic gap. *Earthquake prediction: An international review*, *4*, 29–42. doi: 10.1029/ME004p0029

Habermann, R. E. (1983). Teleseismic detection in the Aleutian Island Arc. *Journal of Geophysical Research: Solid Earth*, *88*(B6), 5056–5064. doi: 10.1029/JB088iB06p05056

Hardebeck, J. L. (2013). Appendix S—Constraining Epidemic Type Aftershock Sequence (ETAS) Parameters from the Uniform California Earthquake Rupture Forecast, Version 3 Catalog and Validating the ETAS Model for Magnitude 6.5 or Greater Earthquakes. *USGS Open File Report*.

Harrington, R. M., & Brodsky, E. E. (2006). The Absence of Remotely Triggered Seismicity in Japan. *Bulletin of the Seismological Society of America*, *96*(3), 871–878. doi: 10.1785/0120050076

Harris, R. A., & Simpson, R. W. (1992). Changes in static stress on southern california faults after the 1992 landers earthquake. *Nature*, *360*(6401), 251–254. doi: 10.1038/360251a0

Hill, D. P. (2008). Dynamic Stresses, Coulomb Failure, and Remote Triggering. *Bulletin of the Seismological Society of America*, *98*(1), 66–92. doi: 10.1785/0120070049

Hill, D. P., & Prejean, S. G. (2015). 4.11 - dynamic triggering. In G. Schubert (Ed.), *Treatise on geophysics (second edition)* (Second Edition ed., p. 273-304). Oxford: Elsevier. doi: 10.1016/B978-0-444-53802-4.00078-6

Inbal, A., Ampuero, J.-P., & Avouac, J.-P. (2017). Locally and remotely triggered aseismic slip on the central San Jacinto Fault near Anza, CA, from joint inversion of seismicity and strainmeter data. *Journal of Geophysical Research: Solid Earth*, *122*(4), 3033–3061. doi: 10.1002/2016JB013499

International Seismological Centre. (2022). On-line bulletin [Computer software manual]. Thatcham, United Kingdom. (http://www.isc.ac.uk)

Johnson, P. A., & Jia, X. (2005). Nonlinear dynamics, granular media and dynamic earthquake triggering. *Nature*, *437*(7060), 871–874.

Kilb, D. (2003). A strong correlation between induced peak dynamic Coulomb stress change from the 1992 M7.3 Landers, California, earthquake and the hypocenter of the 1999 M7.1 Hector Mine, California, earthquake. *Journal of Geophysical Research: Solid Earth*, *108*(B1), ESE 3–1–ESE 3–7. doi: 10.1029/2001JB000678

Knopoff, L., Kagan, Y. Y., & Knopoff, R. (1982). b Values for foreshocks and aftershocks in real and simulated earthquake sequences. *Bulletin of the Seismological Society of America*, *72*(5), 1663–1676. doi: 10.1785/BSSA0720051663

Li, C., Peng, Z., Yao, D., Meng, X., & Zhai, Q. (2022). Temporal changes of seismicity in salton sea geothermal field due to distant earthquakes and geothermal productions. *Geophysical Journal International*, *232*(1), 287–299. doi: 10.1093/gji/ggac324

Marsan, D., & Nalbant, S. S. (2005). Methods for Measuring Seismicity Rate Changes: A Review and a Study of How the Mw7.3 Landers Earthquake Affected the Aftershock Sequence of the Mw6.1 Joshua Tree Earthquake. *Pure and Applied Geophysics*, *162*(6), 1151–1185. doi: 10.1007/s00024-004-2665-4

Marshall, S., Plesch, A., Shaw, J., & Nicholson, C. (2022). *SCEC Community Fault Model (CFM).* Zenodo. (Type: dataset) doi: 10.5281/zenodo.5899364

Matthews, M. V., & Reasenberg, P. A. (1988). Statistical methods for investigating quiescence and other temporal seismicity patterns. *Pure and Applied Geophysics*, *126*(2), 357–372. doi: 10.1007/BF00879003

Meng, X., & Peng, Z. (2014). Seismicity rate changes in the Salton Sea Geothermal Field and the San Jacinto Fault Zone after the 2010 Mw 7.2 El Mayor-Cucapah earthquake. *Geophysical Journal International*, *197*(3), 1750–1762. doi: 10.1093/gji/ggu085

Miyazawa, M., Brodsky, E. E., & Guo, H. (2021). Dynamic Earthquake Triggering in Southern California in High Resolution: Intensity, Time Decay, and Regional Variability. *AGU Advances*, *2*(2), e2020AV000309. doi: 10.1029/2020AV000309

Moutote, L., Marsan, D., Lengliné, O., & Duputel, Z. (2021). Rare Occurrences of Non-cascading Foreshock Activity in Southern California. *Geophysical Research Letters*, *48*(7), e2020GL091757. doi: 10.1029/2020GL091757

Ogata, Y. (1988). Statistical Models for Earthquake Occurrences and Residual Analysis for Point Processes. *Journal of the American Statistical Association*, *83*(401), 9–27. doi: 10.1080/01621459.1988.10478560

Okada, Y., Kasahara, K., Hori, S., Obara, K., Sekiguchi, S., Fujiwara, H., & Yamamoto, A. (2004). Recent progress of seismic observation networks in japan—hi-net, f-net, k-net and kik-net. *Earth, Planets and Space*, *56*(8), xv–xxviii. doi: 10.1186/BF03353076

Pankow, K. L., & Kilb, D. (2020). Going Beyond Rate Changes as the Sole Indicator for Dynamic Triggering of Earthquakes. *Scientific Reports*, *10*(1), 4120. doi: 10.1038/s41598-020-60988-2

Parsons, T., & Dreger, D. S. (2000). Static-stress impact of the 1992 landers earthquake sequence on nucleation and slip at the site of the 1999 m= 7.1 hector mine earthquake, southern california. *Geophysical research letters*, *27*(13), 1949–1952. doi: 10.1029/1999GL011272

Pollitz, F. F., Stein, R. S., Sevilgen, V., & Bürgmann, R. (2012). The 11 april 2012 east indian ocean earthquake triggered large aftershocks worldwide. *Nature*, *490*(7419), 250–253. doi: 10.1038/nature11504

Prejean, S. G., & Hill, D. P. (2018). The influence of tectonic environment on dynamic earthquake triggering: A review and case study on Alaskan volcanoes. *Tectonophysics*, *745*, 293–304. doi: 10.1016/j.tecto.2018.08.007

Prejean, S. G., Hill, D. P., Brodsky, E. E., Hough, S. E., Johnston, M. J. S., Malone, S. D., … Richards-Dinger, K. B. (2004). Remotely Triggered Seismicity on the United States West Coast following the Mw 7.9 Denali Fault Earthquake. *Bulletin of the Seismological Society of America*, *94*(6B), S348–S359. doi: 10.1785/0120040610

Rivera, L., & Kanamori, H. (2002). Spatial heterogeneity of tectonic stress and friction in the crust. *Geophysical Research Letters*, *29*(6), 12–1–12–4. doi: 10.1029/2001GL013803

Ross, Z. E., Idini, B., Jia, Z., Stephenson, O. L., Zhong, M., Wang, X., ... Jung, J. (2019). Hierarchical interlocked orthogonal faulting in the 2019 Ridgecrest earthquake sequence. *Science*, *366*(6463), 346–351. (Publisher: American Association for the Advancement of Science) doi: 10.1126/science.aaz0109

Ross, Z. E., Trugman, D. T., Hauksson, E., & Shearer, P. M. (2019). Searching for hidden earthquakes in Southern California. *Science*, *364*(6442), 767–771. (Publisher: American Association for the Advancement of Science Section: Report) doi: 10.1126/science.aaw6888

Shearer, P. M. (2012a). Self-similar earthquake triggering, Båth's law, and foreshock/aftershock magnitudes: Simulations, theory, and results for southern California. *Journal of Geophysical Research: Solid Earth*, *117*(B6). doi: 10.1029/2011JB008957

Shearer, P. M. (2012b). Space-time clustering of seismicity in california and the distance dependence of earthquake triggering. *Journal of Geophysical Research: Solid Earth*, *117*(B10). doi: 10.1029/2012JB009471

Shearer, P. M., Abercrombie, R. E., & Trugman, D. T. (2022). Improved stress drop estimates for m 1.5 to 4 earthquakes in southern california from 1996 to 2019. *Journal of Geophysical Research: Solid Earth*, *127*(7), e2022JB024243. doi: 10.1029/2022JB024243

Shelly, D. R., Peng, Z., Hill, D. P., & Aiken, C. (2011). Triggered creep as a possible mechanism for delayed dynamic triggering of tremor and earthquakes. *Nature Geoscience*, *4*(6), 384–388. doi: 10.1038/ngeo1141

Silverman, B. (1986). *Density estimation for statistics and data analysis* (Vol. 26). CRC Press.

Stark, M. A., & Davis, S. D. (1996). Remotely triggered microearthquakes at the Geysers Geothermal Field, California. *Geophysical Research Letters*, *23*(9), 945–948. doi: 10.1029/96GL00011

Thomson, D. (1982). Spectrum estimation and harmonic analysis. *Proceedings of the IEEE*, *70*(9), 1055–1096. doi: 10.1109/PROC.1982.12433

Trugman, D. T., & Ross, Z. E. (2019). Pervasive foreshock activity across southern california. *Geophysical Research Letters*, *46*(15), 8772–8781. doi: 10.1029/2019GL083725

Uchide, T., Horikawa, H., Nakai, M., Matsushita, R., Shigematsu, N., Ando, R., & Imanishi, K. (2016). The 2016 kumamoto–oita earthquake sequence: aftershock seismicity gap and dynamic triggering in volcanic areas. *Earth, Planets and Space*, *68*(1), 1–10. doi: 10.1186/s40623-016-0556-4

Utsu, T. (1961). A statistical study on the occurrence of aftershocks. *Geophys.Mag.*, *30*, 521–605.

Utsu, T., Ogata, Y., S, R., & Matsu'ura. (1995). The Centenary of the Omori Formula for a Decay Law of Aftershock Activity. *Journal of Physics of the Earth*, *43*(1), 1–33. doi: 10.4294/jpe1952.43.1

van der Elst, N. J., & Brodsky, E. E. (2010). Connecting near-field and far-field earthquake triggering to dynamic strain. *Journal of Geophysical Research: Solid Earth*, *115*(B7). doi: 10.1029/2009JB006681

Velasco, A. A., Hernandez, S., Parsons, T., & Pankow, K. (2008). Global ubiquity of dynamic earthquake triggering. *Nature Geoscience*, *1*(6). doi: 10.1038/ngeo204

Wiemer, S. (2000). Minimum Magnitude of Completeness in Earthquake Catalogs: Examples from Alaska, the Western United States, and Japan. *Bulletin of the Seismological Society of America*, *90*(4), 859–869. doi: 10.1785/0119990114

Wyss, M., & Marsan, D. (2011). Seismicity rate changes. *Community Online Resource for Statistical Seismicity Analysis*. doi: 10.5078/CORSSA-25837590

Yang, W., & Hauksson, E. (2013). The tectonic crustal stress field and style of faulting along the pacific north america plate boundary in southern california. *Geophysical Journal International*, *194*(1), 100–117.

Yoshida, S. (2016). Earthquakes in Oita triggered by the 2016 M7.3 Kumamoto earthquake. *Earth, Planets and Space*, *68*(1), 176. doi: 10.1186/s40623-016-0552-8

Zhuang, J., Werner, M. J., Zhou, S., Hainzl, S., & Harte, D. (2012). Basic models of seismicity: temporal models. *Community Online Resource for Statistical Seismicity Analysis*. doi: 10.5078/CORSSA-79905851

Supplemental Material for "Ubitquitous Earthquake Dynamic Triggering in Southern California"

DeSalvio, Nicolas D.[1] and Fan, Wenyuan[1]

[1]Scripps Institution of Oceanography, U.C. San Diego, La Jolla, CA, USA

Contents of this file

β_0	4.6	Z_0	4.4	β_{m-0}	0.4	Z_{m-0}	0.2
$\beta_{95\%}$	3.1	$Z_{95\%}$	3.0	$\beta_{m-95\%}$	2.5	$Z_{m-95\%}$	2.5
		$Z_{5\%}$	1.9			$Z_{m-5\%}$	-3.2
β_b	-0.6	Z_b	-0.6	β_{m-b}	-0.1	Z_{m-b}	-0.1
Trigger?	Yes		Yes		No		No

Table S1: Table of test statistic values at a grid point in Coso after the January 8, 2017 M6 Queen Charlotte earthquake (Figure 2).

Median Recurrence Times (days)	β	Z	β_m	Z_m
SSGF	40	48	80	138
CGF	13	53	46	97
SJF	51	53	54	72

Table S2: Table of median recurrence times in days under each statistic for multiple grid points within the Salton Sea Geothermal Field (SSGF), Coso Geothermal Field (CGF), and the San Jacinto Fault Zone (SJF).

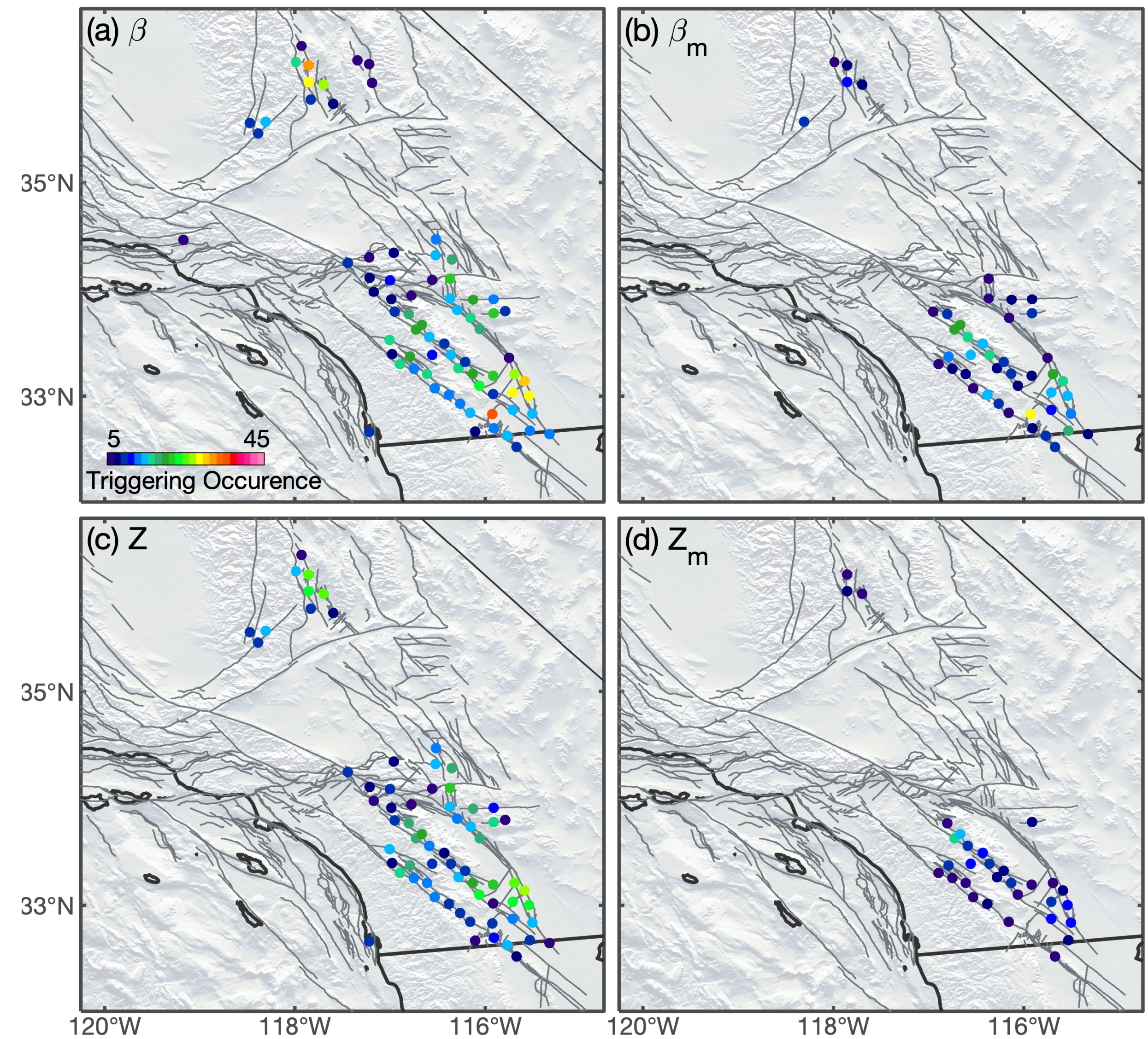

Figure S1: Triggering occurrence during the 6 hour (δ_a=6) time window using the β-statistic (a), β_m-statistic (b), Z-statistic (c), and Z_m-statistic (d).

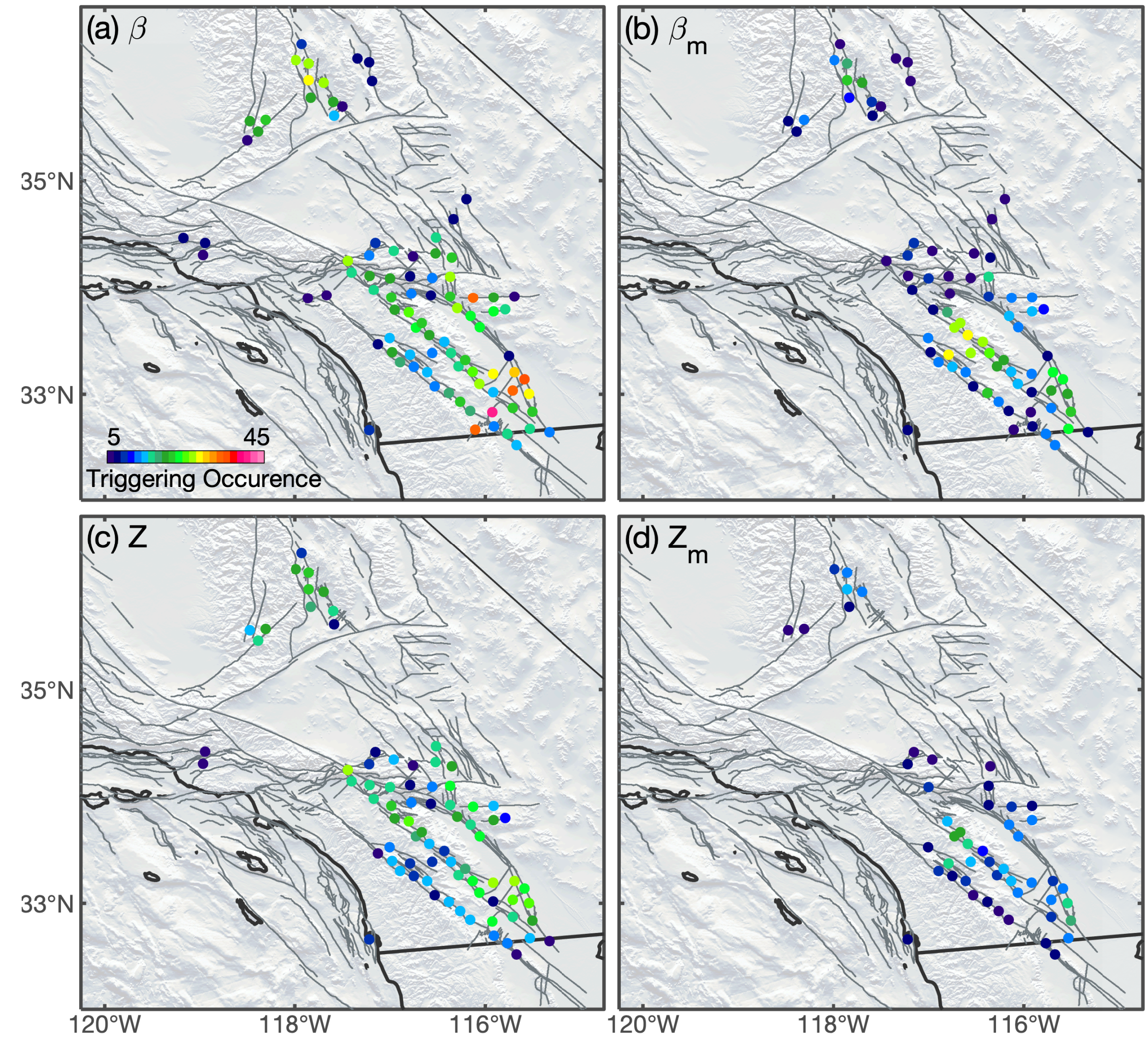

Figure S2: Triggering occurrence during the 12 hour (δ_a=12) time window using the β-statistic (a), β_m-statistic (b), Z-statistic (c), and Z_m-statistic (d).

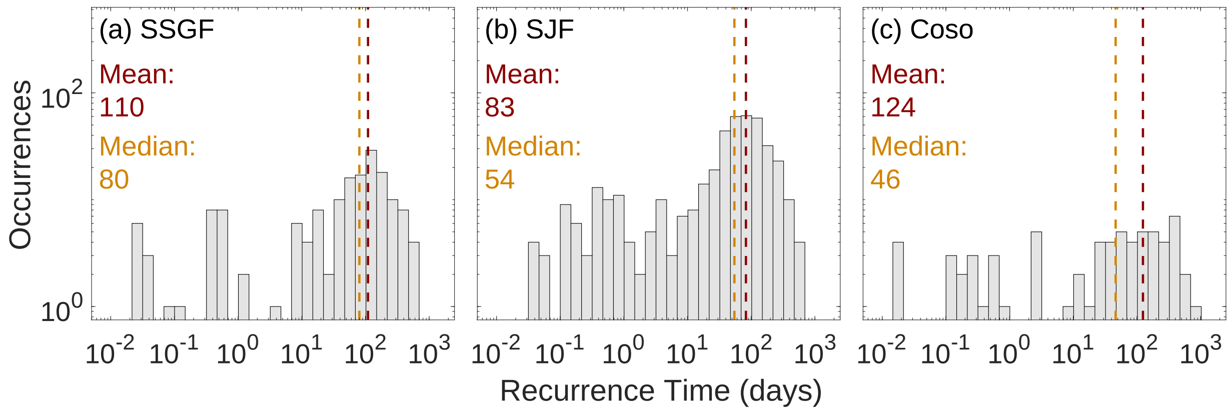

Figure S3: Distribution of triggering recurrence times at example sites that are identified using the β_m-statistic. (a–c) Recurrence times at the Salton Sea Geothermal Field (a), the San Jacinto Fault Zone (b), and the Coso Geothermal Field (c).

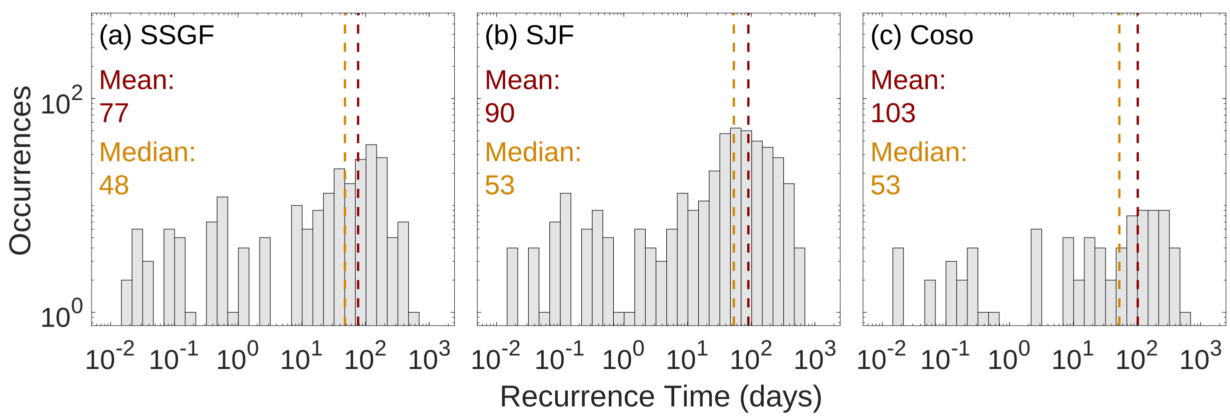

Figure S4: Distribution of triggering recurrence times at example sites that are identified using the Z-statistic. (a–c) Recurrence times at the Salton Sea Geothermal Field (a), the San Jacinto Fault Zone (b), and the Coso Geothermal Field (c).

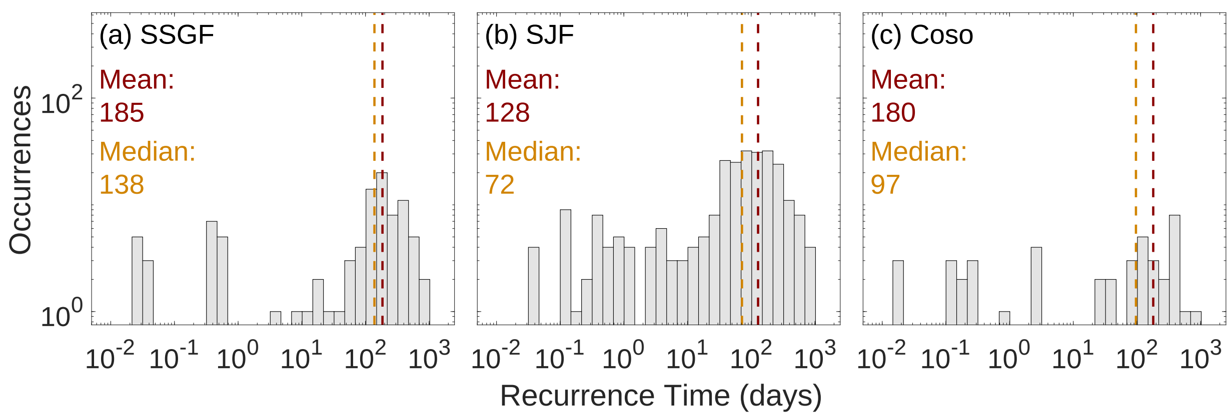

Figure S5: Distribution of triggering recurrence times at example sites that are identified using the Z_m-statistic. (a–c) Recurrence times at the Salton Sea Geothermal Field (a), the San Jacinto Fault Zone (b), and the Coso Geothermal Field (c).

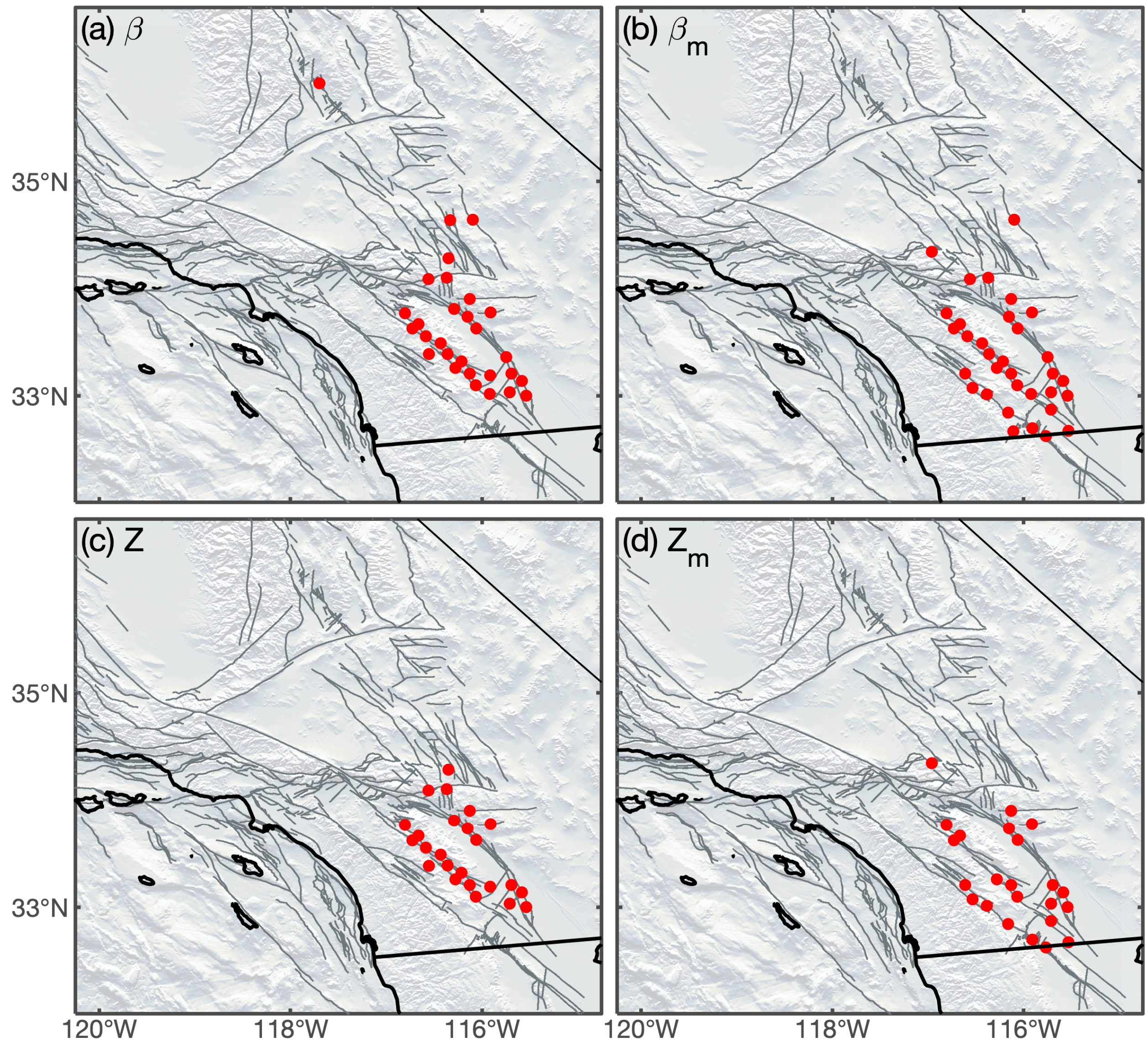

Figure S6: Triggered grid points following the 2010 El Mayor Cucapah earthquake.

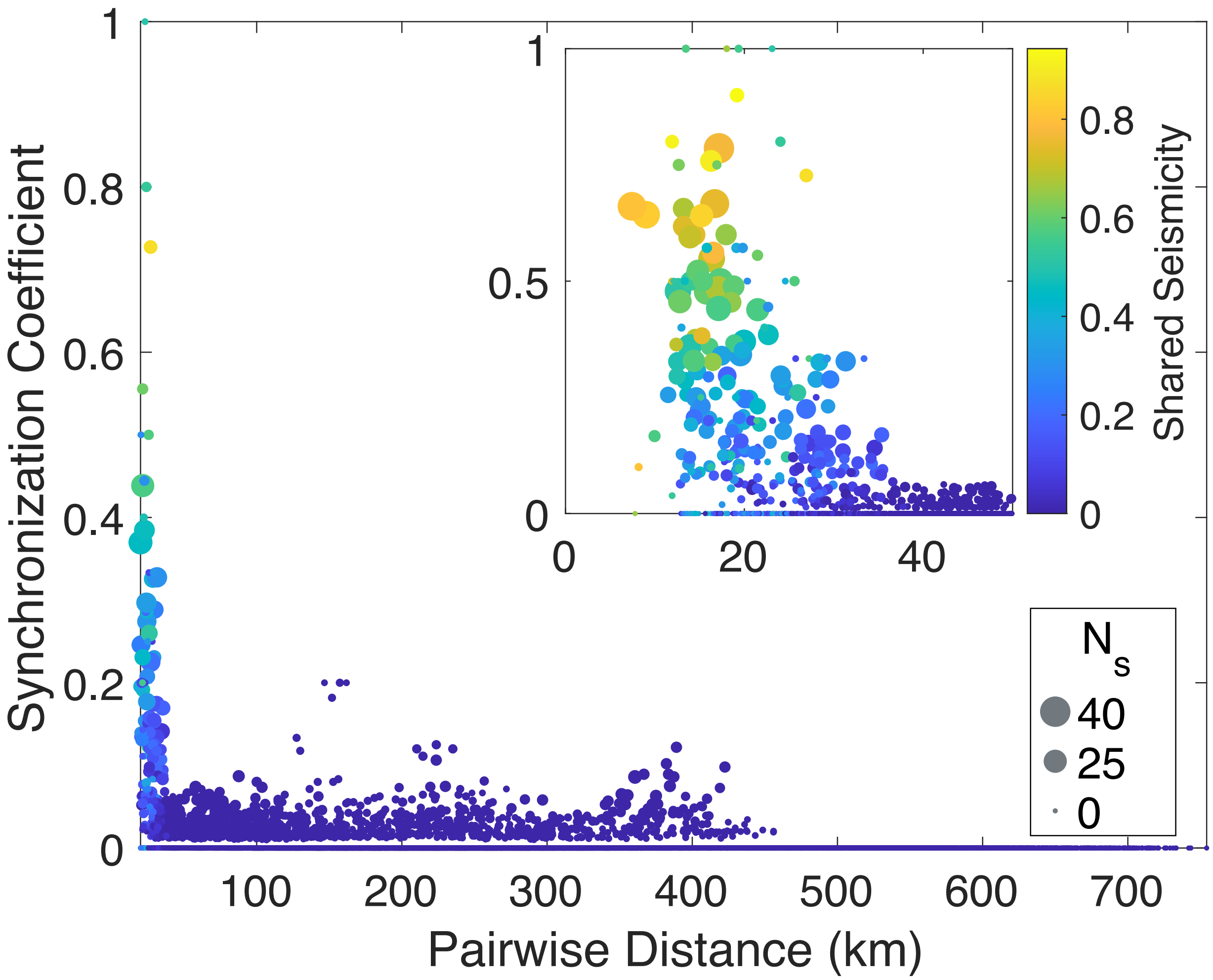

Figure S7: Synchronization coefficient versus pairwise grid distance for the Z-statistic. Inset displays a zoom-in view for grids that are less than 50 km apart. Marker color shows the proportion of local earthquakes that are shared between grid pairs during the study period. Marker size indicates the number of candidate earthquakes that cause triggering at both locations, N_s.

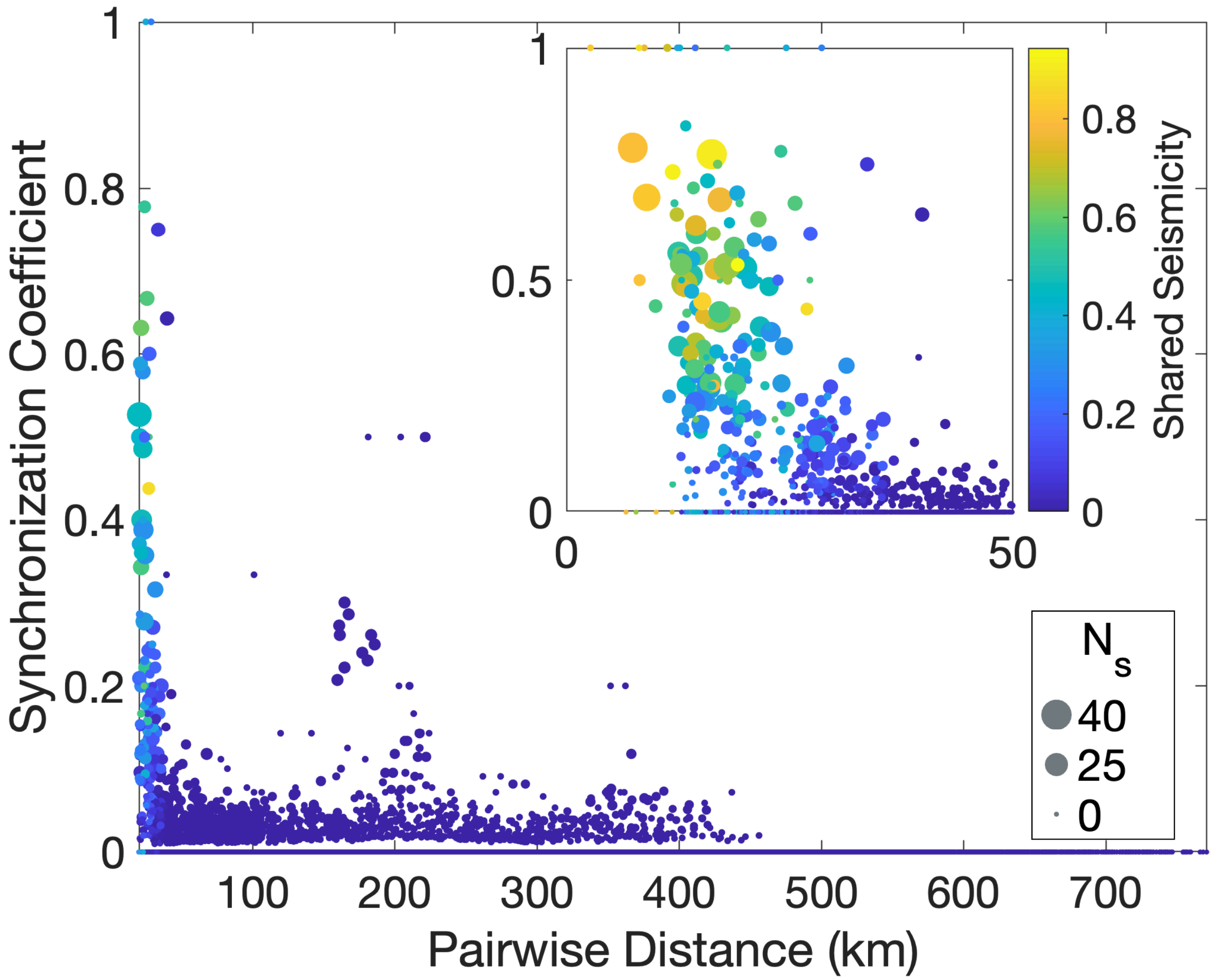

Figure S8: Synchronization coefficient versus pairwise grid distance for the β_m-statistic. Inset displays a zoom-in view for grids that are less than 50 km apart. Marker color shows the proportion of local earthquakes that are shared between grid pairs during the study period. Marker size indicates the number of candidate earthquakes that cause triggering at both locations, N_s. Points beyond 100 km that have $S > 0.2$ fall into two categories: either too few triggering occurrences to be significant, or trigger after multiple $M \geq 6$ aftershocks within an aftershock sequence of a larger earthquake.

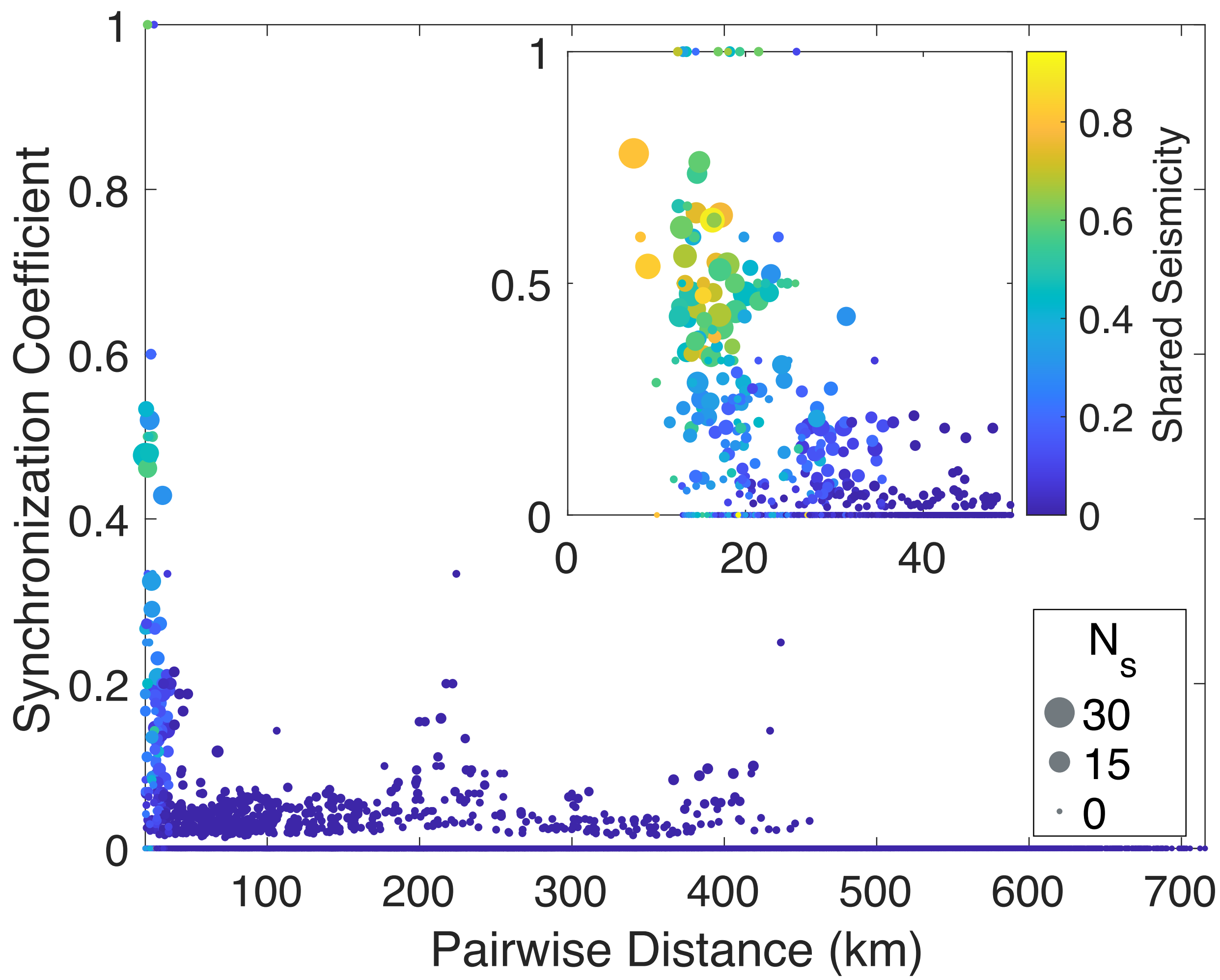

Figure S9: Synchronization coefficient versus pairwise grid distance for the Z_m-statistic. Inset displays a zoom-in view for grids that are less than 50 km apart. Marker color shows the proportion of local earthquakes that are shared between grid pairs during the study period. Marker size indicates the number of candidate earthquakes that cause triggering at both locations, N_s.

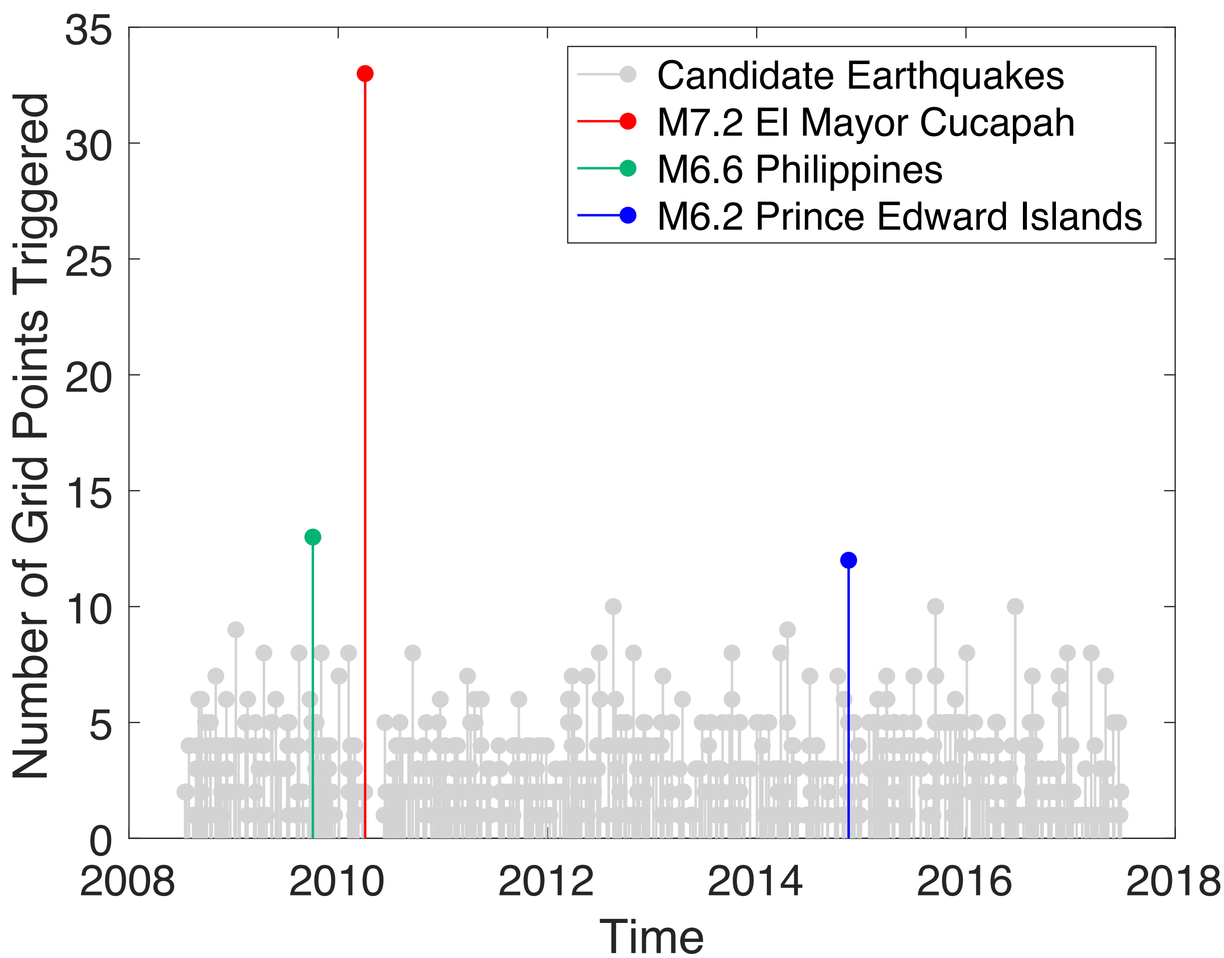

Figure S10: Time series of the number of grid points triggered after each candidate earthquake (β_m-statistic). Candidate earthquakes within 60 days following the 2010 El Mayor Cucapah earthquake are not analyzed.

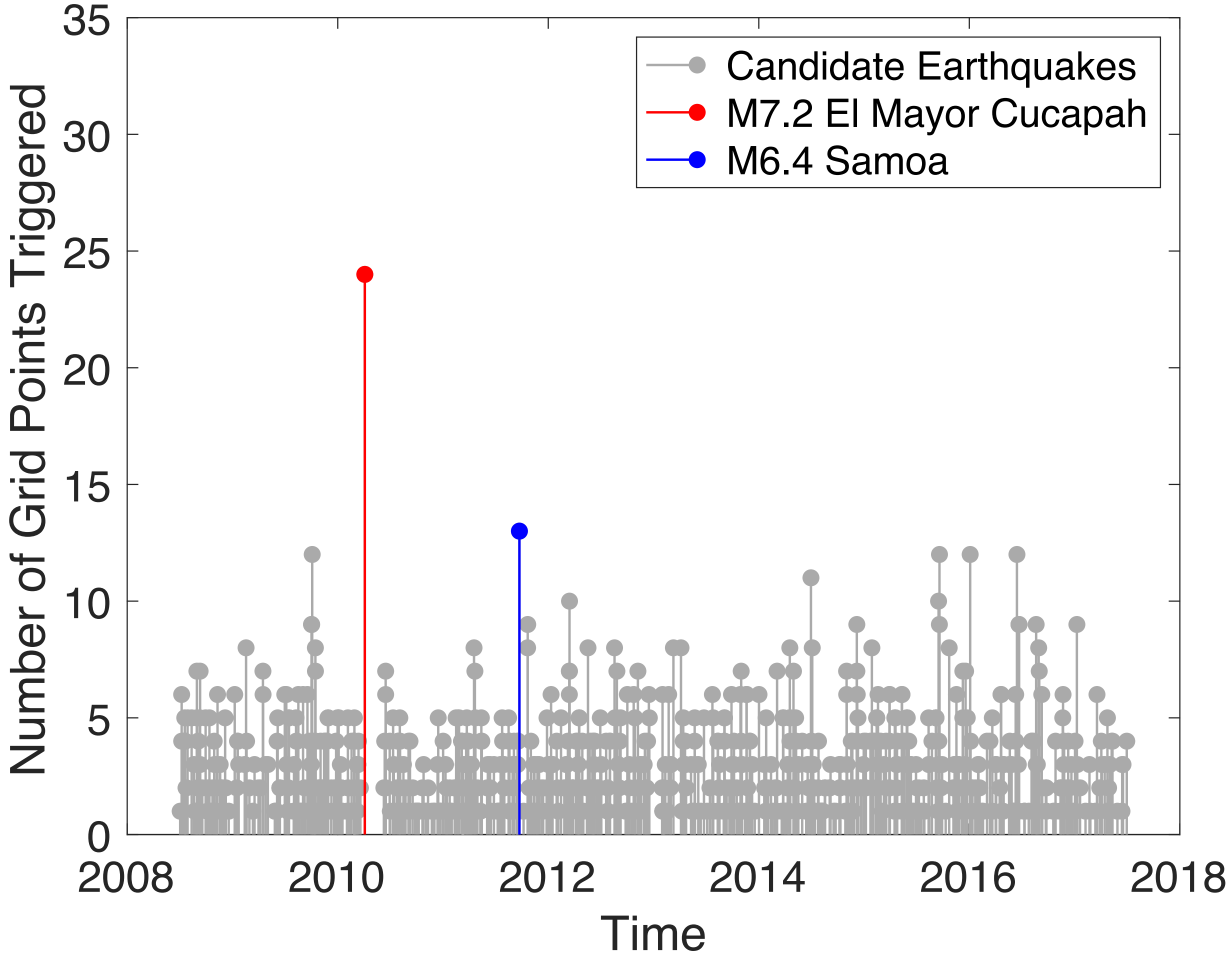

Figure S11: Time series of the number of grid points triggered after each candidate earthquake (Z-statistic). Candidate earthquakes within 60 days following the 2010 El Mayor Cucapah earthquake are not analyzed.

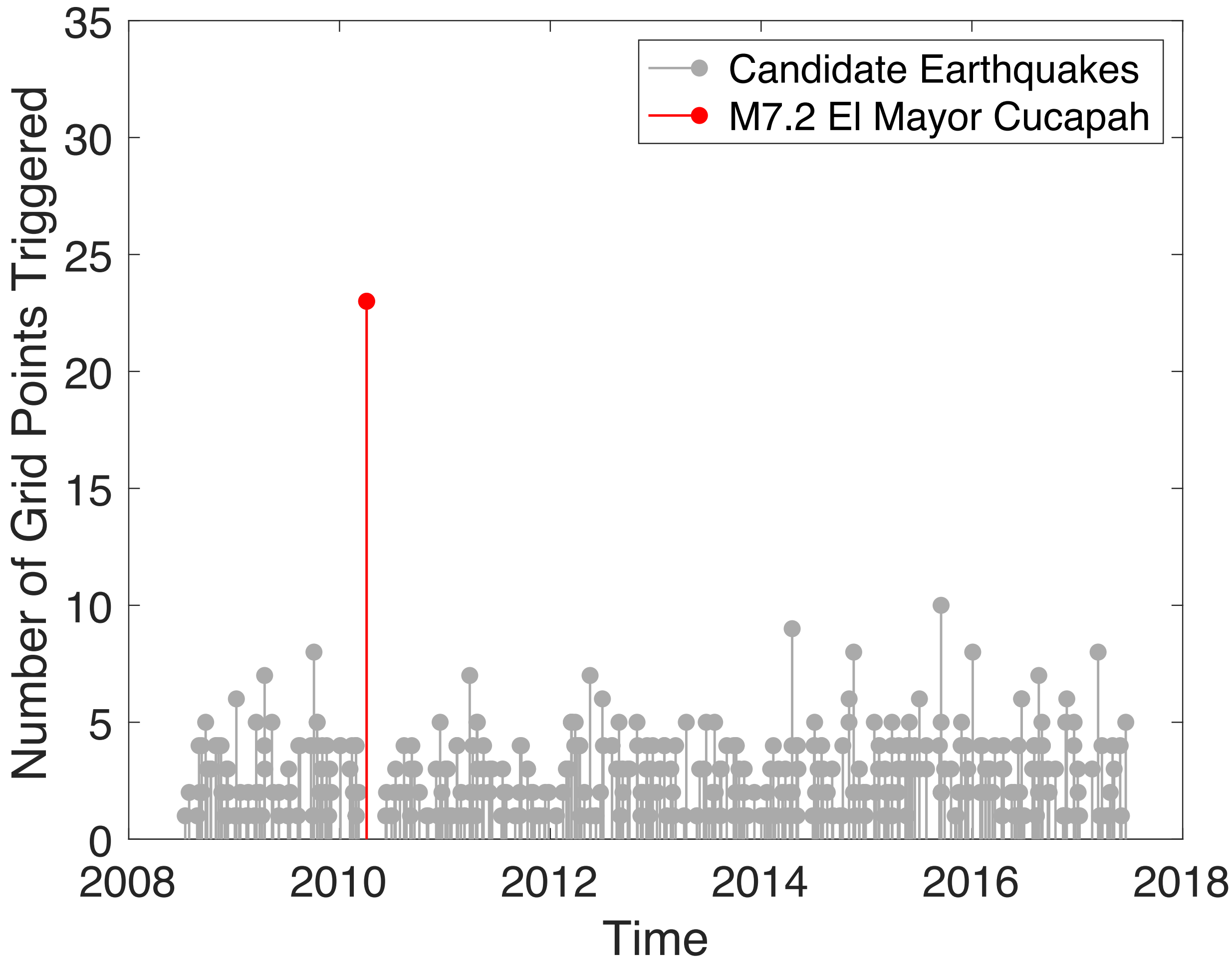

Figure S12: Time series of the number of grid points triggered after each candidate earthquake (Z_m-statistic). Candidate earthquakes within 60 days following the 2010 El Mayor Cucapah earthquake are not analyzed.

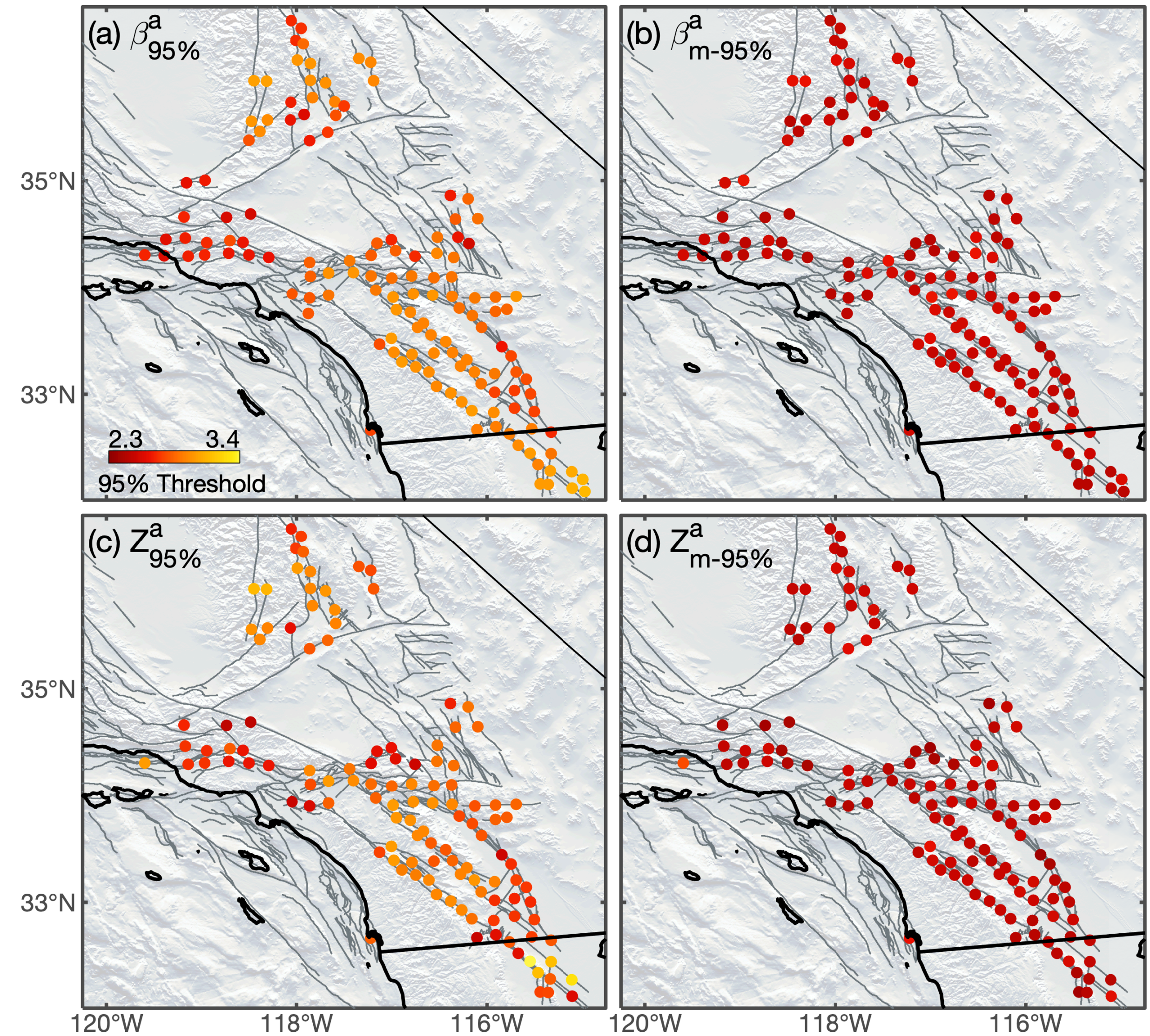

Figure S13: Spatial patterns of the median of the 95% percentile thresholds during the 6 hour time window for the β-statistic (a), β_m-statistic (b), Z-statistic (c), and Z_m-statistic (d).

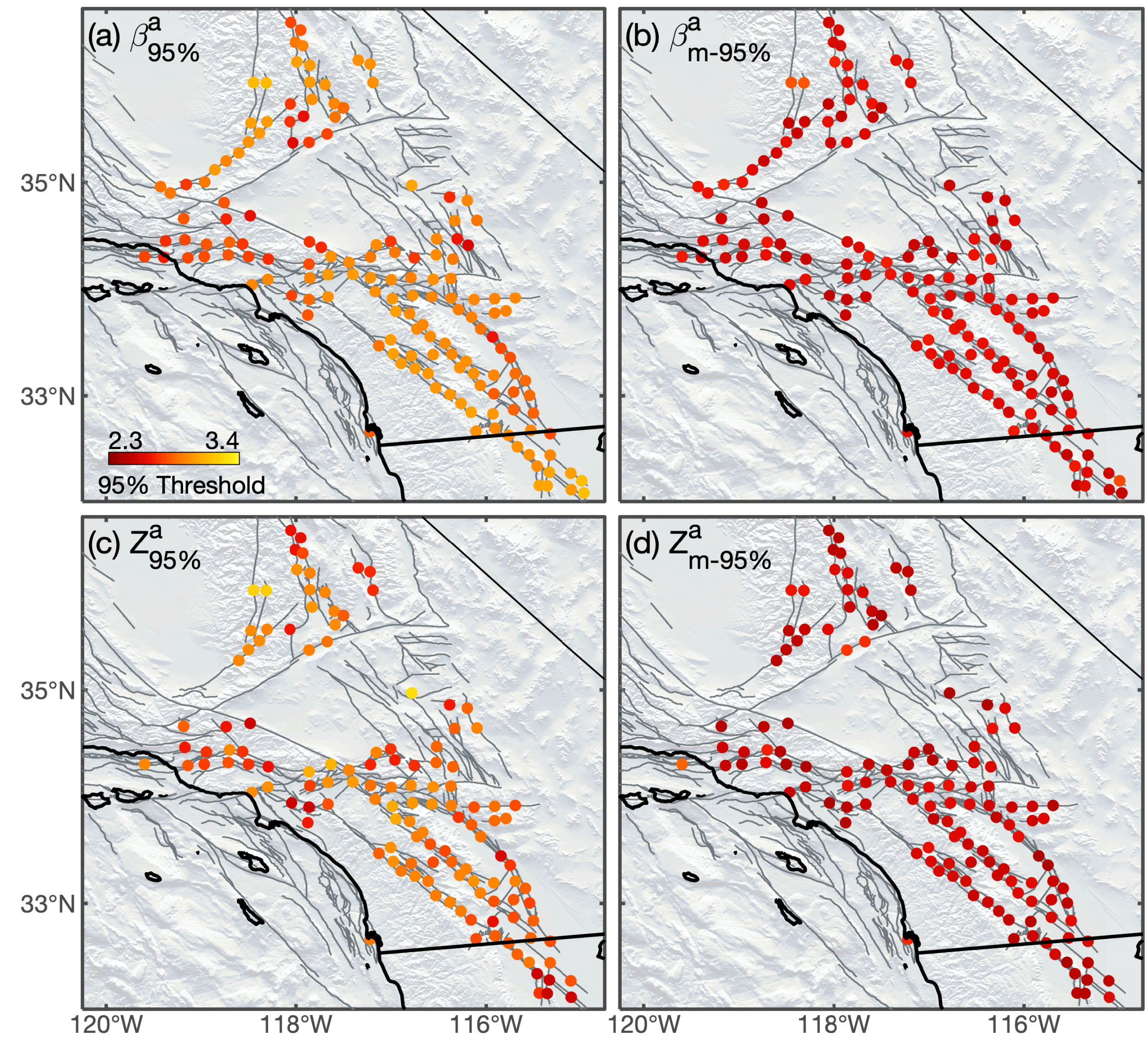

Figure S14: Spatial patterns of the median of the 95% percentile thresholds during the 12 hour time window for the β-statistic (a), β_m-statistic (b), Z-statistic (c), and Z_m-statistic (d).

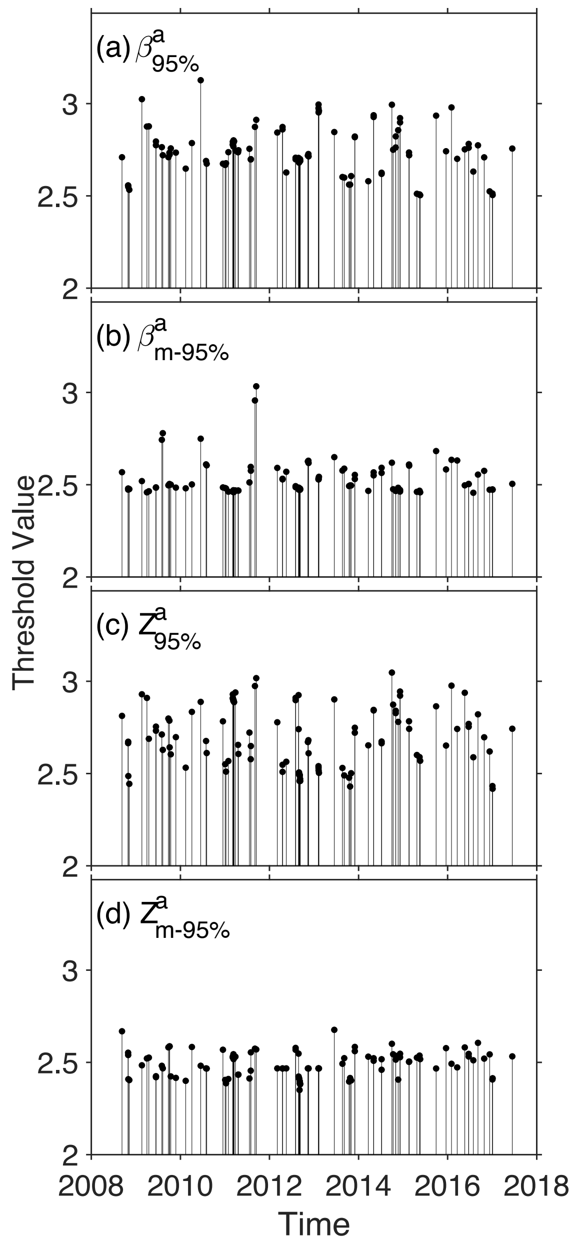

Figure S15: Temporal evolution of the 95% percentile thresholds during the 6 hour time window at a site in the Salton Sea Geothermal Field for the β-statistic (a), β_m-statistic (b), Z-statistic (c), and Z_m-statistic (d).

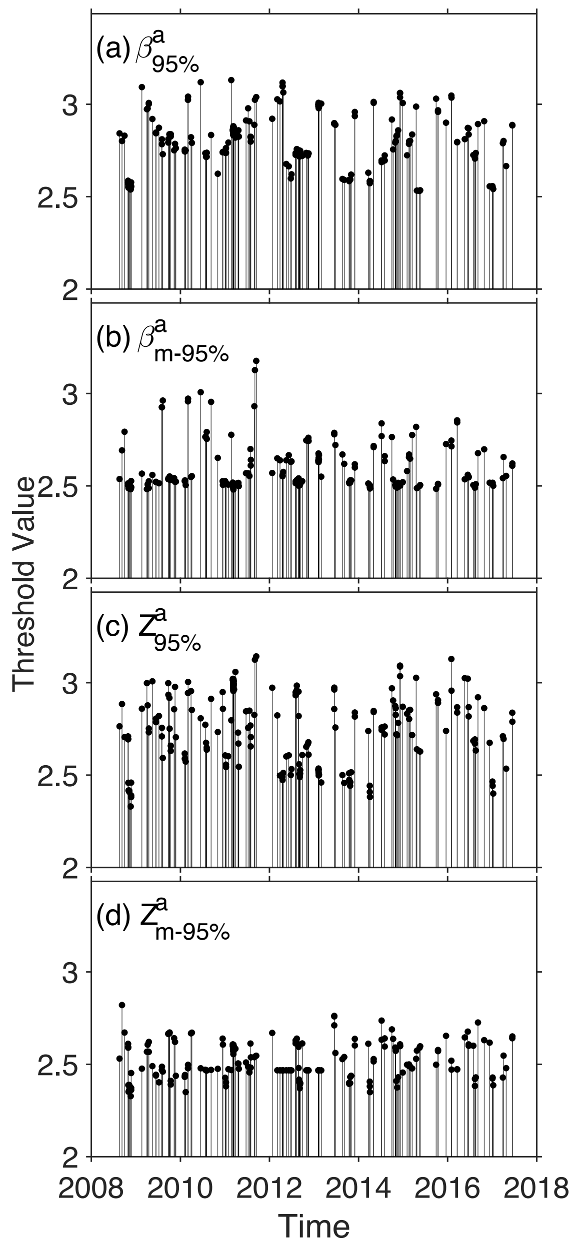

Figure S16: Temporal evolution of the 95% percentile thresholds during the 12 hour time window at a site in the Salton Sea Geothermal Field for the β-statistic (a), β_m-statistic (b), Z-statistic (c), and Z_m-statistic (d).

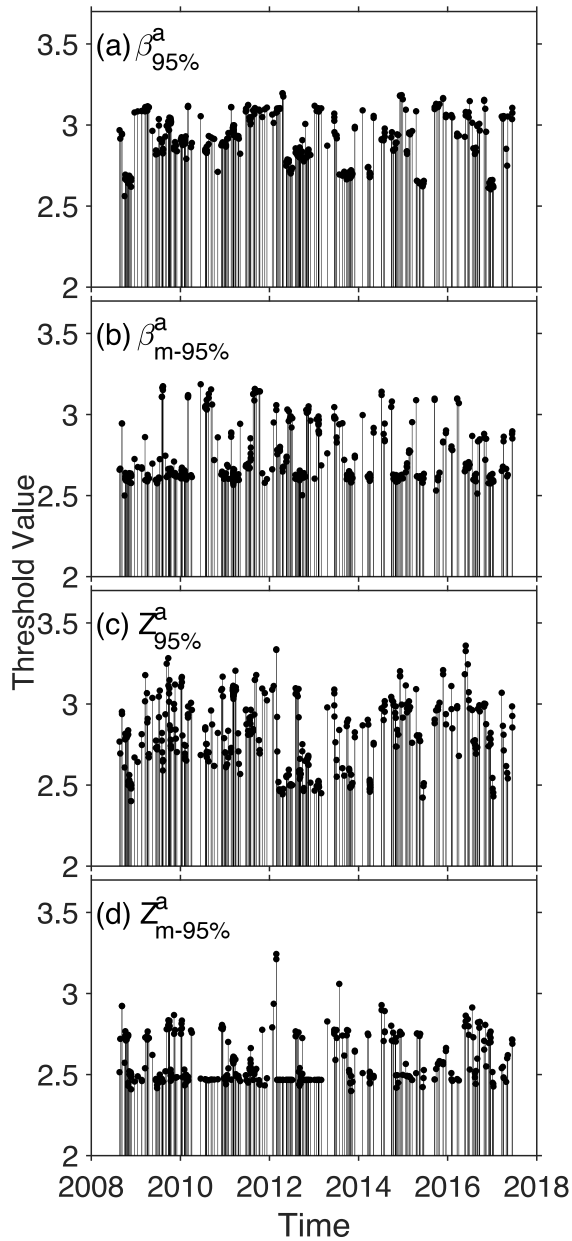

Figure S17: Temporal evolution of the 95% percentile thresholds during the 24 hour time window at a site in the Salton Sea Geothermal Field for the β-statistic (a), β_m-statistic (b), Z-statistic (c), and Z_m-statistic (d).